SYNTHESIS AND CHARACTERIZATION OF A NEW PROTON CONDUCTING MATERIAL AND ITS USE AS HYDROGEN SEPARATION MEMBRANE

By

GUOJING ZHANG

A DISSERTATION PRESENTED TO THE GRADUATE SCHOOL
OF THE UNIVERSITY OF FLORIDA IN PARTIAL FULFILLMENT
OF THE REQUIREMENTS FOR THE DEGREE OF
DOCTOR OF PHILOSOPHY

UNIVERSITY OF FLORIDA

2005

Copyright 2005

by

GUOJING ZHANG

To my grandfather.

ACKNOWLEDGMENTS

I would like to thank Dr. Eric D. Wachsman for providing me such a good opportunity to do this research work. His advice and guidance were very valuable and will always be appreciated. I would also like to thank other supervisory committee members, Dr. W. Sigmund, Dr. J. C. Nino, Dr. E. D. Whitney, Dr. K. Jones and Dr. T. Anderson.

I sincerely acknowledge Dr. Yoon, Dr. Guo, Dr. Rhodes, Dr. Song, Dr. Jaiswal and Dr. Park for their suggestions and kind help on my research. I would also like to thank W. Zhang and Dr. Kaufman for their help with TEM characterization, G. Scheiffele in ERC for his help with IR and Raman characterization, C. Cheng and Dr. R. Bowers in Chemistry Department for their help with MAS-NMR measurement, Dr. S. Sinnott and Dr. J. C. Nino for their help on the crystallographic studies. Dr. Nino's precious suggestion on my dissertation is sincerely appreciated. I also want to thank Martin, Sean, Eric and Jeremiah for their reading and correcting my dissertation.

Special appreciation also goes to the encouragement and counsel from my master advisor, Prof. Jia in ECUST, and all the instructors in P. R. China. Finally, I would like to thank my parents and my husband for their great support and unconditional love. I would also like to thank my grandparents for my six-year childhood with them. I would like to dedicate this dissertation especially to my grandpa. His uprightness and patience will be remembered and inherited by us forever.

TABLE OF CONTENTS

page

ACKNOWLEDGMENTS iv

LIST OF TABLES viii

LIST OF FIGURES x

ABSTRACT xiv

CHAPTER

1 INTRODUCTION 1

1.1 Application of Proton Conducting Material 1
1.2 Proton Conducting Materials 2
1.2.1 Proton Conductor 2
1.2.2 $BaCeO_3$ Based Proton Conductors 3
1.3 Experimental Techniques 7
1.3.1 Synthesis 7
1.3.2 Common Characterization 7
1.3.2.1 Infrared (IR) and Raman spectroscopy 8
1.3.2.2 Nuclear Magnetic Resonance spectroscopy 9
1.3.3 Electrochemical Characterization 10
1.3.3.1 Conductivity measurement 10
1.3.3.2 Transference number measurement 11
1.3.3.3 Hydrogen permeation 13

2 REVIEW OF PROTONIC CONDUCTORS 20

2.1 Introduction 20
2.2 Proton Conduction in Phosphates 20
2.2.1 Proton Conduction in Doped $LaPO_4$ 21
2.2.2 Proton Conduction in Other Phosphates 23
2.3 Proton Incorporation Mechanism in Phosphates 25
2.3.1 Norby's Hypothesis 25
2.3.2 Amezawa's Hypothesis 27
2.3.2 Haile's and Mizuno's Hypothesis 32
2.4 Transference Number in Phosphates 33
2.5 Hydrogen Permeation in Phosphates 33

2.6 Summary 34

3 PHASE IDENTIFICATION 38

3.1 Introduction 38
3.2. Experiment 38
3.2.1 Electroless Deposition 38
3.2.2 Solid State Reaction 39
3.2.3 Characterization 39
3.3 Results and Discussion 40
3.3.1 XRD Results 40
3.3.2 IR Results 44
3.3.3 Conductivity Measurement 46
3.4 Conclusion 47

4 SYNTHESIS AND CHARACTERIZATION OF $Ba_3Ce(PO_4)_3$ 60

4.1 Introduction 60
4.2 Experiment 61
4.2.1 Synthesis 61
4.2.2 Characterization 61
4.3 Results and Discussion 63
4.3.1 Synthesis 63
4.3.2 Particle Size Characterization 64
4.3.3 Crystal Structure Characterization 64
4.3.4 Defect Structure Characterization 66
4.3.4.1 Raman characterization 66
4.3.4.2 NMR characterization 69
4.3.4.3 Defect structure 70
4.3.5 Chemical and Thermal Stability 83
4.3.6 Thermal Expansion 83
4.4 Conclusion 83

5 CONDUCTIVITY MEASUREMENT OF $Ba_3Ce(PO_4)_3$ 99

5.1 Introduction 99
5.2 Experiment 99
5.3 Results and Discussion 100
5.3.1 Sintering and Density Issue 100
5.3.2 Conductivity 101
5.3.2.1 Conductivity in different atmospheres 101
5.3.2.2 Conductivity as a function of oxygen partial pressure 107
5.3.2.3 Conductivity as a function of water vapor partial pressure 117
5.3.2.4 Conductivity as a function of hydrogen partial pressure 118
5.3.2.5 Conductivity under CO/CO_2 mixture gas 119
5.4 Conclusion 120

6 TRANSFERENCE NUMBER MEASUREMENT 136

6.1 Introduction 136
6.2 Experiment 138
6.3 Results and Discussion 138
6.4 Conclusion 142

7 HYDROGEN PERMEATION MEASUREMENT 147

7.1 Introduction 147
7.2 Experiment 148
7.3 Results and Discussion 149
7.3.1 Hydrogen Permeability of $Ba_3Ce(PO_4)_3$ 149
7.3.2 Hydrogen Permeability of Composite $Ba_3Ce(PO_4)_3$ with CeO_2 149
7.3.3 Hydrogen Permeability of Composite 35vol%Pd-65vol% $Ba_3Ce(PO_4)_3$ 150
7.4 Conclusion 151

8 CONCLUSION 159

LIST OF REFERENCES 161

BIOGRAPHICAL SKETCH 166

LIST OF TABLES

Table		page
1-1	Infrared and Raman stretching frequency ranges for phosphate anions.	18
1-2	Infrared and Raman functional group frequencies.	18
1-3	Reported Raman shifts of Sr doped $LaPO_4$.	19
1-4	Chemical shift of ^1H NMR and ^{31}P NMR in Sr doped $LaPO_4$.	19
3-1	Band assignment of $SrCe_{1-x}Y_xO_{3-\delta}$, $SrZr_{1-x}Y_xO_{3-\delta}$, and BCG5Pd.	58
3-2	Band assignment for $Cs_2(HSO_4)(H_2PO_4)$.	58
3-3	Band assignment for BCG4.31Pd and sintered mixture of BCGO+$NH_4H_2PO_4$.	59
4-1	Measured spacing d compared with those obtained from TEM result and literature value.	96
4-2	Wavenumbers (cm^{-1}) of the absorption bands in infrared spectra of $Ba_3Ce(PO_4)_3$	96
4-3	Raman shift of $Ba_3Ce(PO_4)_3$ at dry atmosphere compared with Sr doped $LaPO_4$.	96
4-4	Raman shift of $Ba_3Ce(PO_4)_3$ at wet atmosphere compared with Sr doped $LaPO_4$	97
4-5	Chemical shift of ^1H NMR of $Ba_3Ce(PO_4)_3$ after different atmosphere treatments compared with Sr doped $LaPO_4$	97
4-6	Defect concentration dependence of p_{H_2}, p_{O_2} and p_{H_2O}.	98
5-1	Electrical conductivity data of $Ba_3Ce(PO_4)_3$ under different atmospheres.	134
5-2	Conductivity dependence of oxygen partial pressure.	134
5-3	Conductivity dependency of water partial pressure.	135
5-4	Conductivity dependence of hydrogen partial pressure.	135

6-1 Corrected hydrogen concentration in cell 1-cell4. 146

6-2 Proton transference number of $Ba_3Ce(PO_4)_3$ at different temperatures in cell 1. ..146

LIST OF FIGURES

Figure page

1-1 Total conductivity of BCGO and Pd-BCGO composite. 14

1-2 Conductivity of various systems in wet 10vol% hydrogen. 15

1-3 Hydrogen flux of BCGO with time at 650 ºC. 15

1-4 Hydrogen flux through BCG1Pd with time at 650 °C. 16

1-5 Hydrogen flux through BCG5Pd with time at 650 °C. 16

1-6 Hydrogen flux as a function of temperature through different system. 17

1-7 Conductivity in some proton conductors as a function of temperature. 17

2-1 The crystal structure of $LaPO_4$ with monazite structure. 36

2-2 Polyhedral diagrams of the monazite structure. 36

2-3 Phosphate, diphosphate and hydrogen phosphate structure and proton transfer illustration using "MS modeling" software and photoshop. 37

3-1 XRD patterns of composite BCG5Pd and BCG35Pd. 48

3-2 XRD results of deposited composites at different pH conditions. 48

3-3 XRD results of composite BCG4.31Pd with different sintering temperature compared with JCPDS 43-0643, 25-0028, 43-1002, 22-0074 and 32-0199. 49

3-4 Phase diagram of system YPO_4-$Ca_3(PO_4)_2$. 50

3-5 XRD results of sintered mixtures of BCGO and $NH_4H_2PO_4$ with different $NH_4H_2PO_4$ concentration. 51

3-6 XRD results of mixtures of BCGO and $NH_4H_2PO_4$ with or without argon treatment. 52

3-7 IR spectra of composite BCG5Pd, $SrCe_{1-x}Y_xO_{3-\delta}$ and $SrZr_{1-x}Y_xO_{3-\delta}$ 53

3-8 IR spectra of composite BCG5Pd and $Cs_2(HSO_4)(H_2PO_4)$ 55

3-9 IR spectra of the sintered mixture of BCGO and $NH_4H_2PO_4$ compared with those of composite BCG5Pd and BCG4.31Pd. 55

3-10 Impedance plot of the sintered mixture of BCGO and $NH_4H_2PO_4$ at 800 °C in wet 10% hydrogen atmosphere: 56

3-11 Arrhenius plot of the mixture of BCGO and $NH_4H_2PO_4$ in wet 10% hydrogen.....57

4-1 XRD patterns of calcined precipitate with different calcination temperatures.. 85

4-2 Compare XRD results from JCPDS, experiment and calculation by CaRIne Crystallography V3.1 software. 86

4-3 IR of precipitates after calcining at different temperatures for 4 h. 86

4-4 IR spectra of $Ba_3Ce(PO_4)_3$ and composite BCG5Pd....87

4-5 Bright field image and selected area diffraction pattern of $Ba_3Ce(PO_4)_3$ particle....87

4-6 Crystal structure of $Ba_3Ce(PO_4)_3$ using "MS modeling" software.. 88

4-7 Crystal structure of $Ba_3Ce(PO_4)_3$ using "CaRIne Crystallography V3.1" software.. 89

4-8 Directional view of $Ba_3Ce(PO_4)_3$ 90

4-9 Raman spectra of $Ba_3Ce(PO_4)_3$ after dry air, N_2 and H_2 treatment....91

4-10 Raman spectra of $Ba_3Ce(PO_4)_3$ after wet and dry nitrogen treatment.. 93

4-11 Raman spectra of $Ba_3Ce(PO_4)_3$ after wet hydrogen treatment....93

4-12 High- resolution ^1H NMR spectra of $Ba_3Ce(PO_4)_3$ after different gas treatment at 550ºC for 24 h. 94

4-13 High-temperature XRD pattern of $Ba_3Ce(PO_4)_3$ 94

4-14 XRD of $Ba_3Ce(PO_4)_3$ after different atmosphere treatments at 600 °C for 10 h. ..95

4-15 Thermal expansion behavior of $Ba_3Ce(PO_4)_3$ in hydrogen and air atmosphere. ...95

5-1 Relative density with different sintering temperatures for 8h....121

5-2 XRD of $Ba_3Ce(PO_4)_3$ with different sintering temperatures and dwell times. 121

5-3 SEM images of fracture cross sections of $Ba_3Ce(PO_4)_3$ pellets with a dwell time of 8 h and different sintering temperatures.. 122

5-4 Porous Pt electrode on the surface of a $Ba_3Ce(PO_4)_3$ pellet. 123

5-5 Impedance plot of $Ba_3Ce(PO_4)_3$ in different atmospheres.. 125

5-6 Arrhenius Plot of $Ba_3Ce(PO_4)_3$ under different atmospheres. 126

5-7 Conductivity comparison of $Ba_3Ce(PO_4)_3$ with reported data from literature.....126

5-8 Conductivity of $Ba_3Ce(PO_4)_3$ as a function of oxygen partial pressure in the whole oxygen partial pressure region.....127

5-9 Conductivity of $Ba_3Ce(PO_4)_3$ as a function of oxygen partial pressure in the case 1 of low oxygen partial pressure region. 128

5-10 Conductivity of $Ba_3Ce(PO_4)_3$ as a function of oxygen partial pressure in the case 2 of low oxygen partial pressure region. 128

5-11 Conductivity of $Ba_3Ce(PO_4)_3$ as a function of oxygen partial pressure in the case 4 of low oxygen partial pressure region. 129

5-12 Conductivity of $Ba_3Ce(PO_4)_3$ as a function of oxygen partial pressure in the case 3 of low-intermediate oxygen partial pressure region. 129

5-13 Conductivity of $Ba_3Ce(PO_4)_3$ as a function of oxygen partial pressure in the case 4 of low-intermediate oxygen partial pressure region. 130

5-14 Conductivity of $Ba_3Ce(PO_4)_3$ as a function of oxygen partial pressure in the intermediate oxygen partial pressure region. 130

5-15 Conductivity of $Ba_3Ce(PO_4)_3$ as a function of oxygen partial pressure in the high oxygen partial pressure region. 131

5-16 Conductivity of $Ba_3Ce(PO_4)_3$ as a function of water partial pressure in hydrogen.....131

5-17 Conductivity of $Ba_3Ce(PO_4)_3$ as a function of water partial pressure in nitrogen.....132

5-18 Conductivity of $Ba_3Ce(PO_4)_3$ as function of hydrogen concentration with p_{H_2O}=0.0312atm. 132

5-19 Conductivity of $Ba_3Ce(PO_4)_3$ under the CO/CO_2 gas mixture compared with that under purified argon gas. 133

6-1 Schematic illustration of the experimental setup for transference number measurement. 143

6-2 Open circuit voltage of $Ba_3Ce(PO_4)_3$ as a function of Log($P_{H_2}^{II}/P_{H_2}^{I}$) in the wet and dry concentration cells at 600 and 550°C. 143

6-3 Hydrogen concentration calibration of the mass spectrometer. 144

6-4 Open circuit voltage of $Ba_3Ce(PO_4)_3$ as a function of Log($P_{H_2}^{II}/P_{H_2}^{I}$) with or without MS correction in dry concentration cells at 600°C. 144

6-5 Proton transference number as a function of temperature in the dry hydrogen atmosphere. 145

7-1 Hydrogen permeability measurement system. 153

7-2 Gas partial pressure on sweep side while testing $Ba_3Ce(PO_4)_3$. 154

7-3 XRD patterns of composite CeO_2 - $Ba_3Ce(PO_4)_3$ before and after sintering. 154

7-4 Cross-section image of composite CeO_2 - $Ba_3Ce(PO_4)_3$. 155

7-5 Gas partial pressure on sweeping side while testing composite CeO_2 - $Ba_3Ce(PO_4)_3$. 155

7-6 XRD pattern of composite 35 vol% Pd–65 vol% $Ba_3Ce(PO_4)_3$ after separate treatment in air and argon 156

7-7 Surface image of composite 65 vol% $Ba_3Ce(PO_4)_3$ -35 vol% Pd. 156

7-8 EDS results of $Ba_3Ce(PO_4)_3$ grain and Pd grain in the composite 65 vol% $Ba_3Ce(PO_4)_3$ -35 vol% Pd. 157

7-9 Cross-section image of composite 35 vol% Pd-65 vol% $Ba_3Ce(PO_4)_3$. 157

7-10 Gas partial pressure on sweeping side with composite 35 vol% Pd-65 vol% $Ba_3Ce(PO_4)_3$. 158

Abstract of Dissertation Presented to the Graduate School
of the University of Florida in Partial Fulfillment of the
Requirements for the Degree of Doctor of Philosophy

SYNTHESIS AND CHARACTERIZATION OF A NEW PROTON CONDUCTING MATERIAL AND ITS USE AS HYDROGEN SEPARATION MEMBRANE

By
Guojing Zhang

December 2005

Chair: Eric D. Wachsman
Major Department: Materials Science and Engineering

$BaCe_{0.85}Gd_{0.15}O_{3-x}$ (BCGO) has high proton conductivity but does not exhibit any of the necessary electronic conductivity required for use as a hydrogen separation membrane. To address this problem, a two phase composite Pd-BCGO was synthesized in our lab to form a mixed ionic electronic conductor (MIEC). Composites of 35vol%Pd-65vol%BCGO (BCG35Pd) and 5vol%Pd-95vol%BCGO (BCG5Pd) were synthesized by solid-state reaction and electroless deposition, respectively.

At temperatures lower than 550 °C, the hydrogen flux of BCG5Pd was higher than that of BCG35Pd. The hydrogen flux of BCG5Pd also increased with time at 650 °C and continued to increase for 20 hours until hydrogen was shut off. This was an unusual behavior compared with BCG35Pd. The second phase Pd did not exhibit such a trend under isothermal conditions, indicating the existence of a tertiary phase.

Analysis was performed using X-ray diffraction (XRD) and infrared (IR) spectroscopy. The results showed that the acidic electroless bath decomposed part of

BCGO and that a phosphorous impurity was absorbed. BCGO and the phosphorus impurity reacted at high sintering temperature to form a BaO-rich compound $Ba_3Ce(PO_4)_3$ and leave excess CeO_2. The compound $Ba_3Ce(PO_4)_3$ was most likely the tertiary phase.

Single-phase $Ba_3Ce(PO_4)_3$ was synthesized successfully at 1100°C by the coprecipitation method. The conductivities of $Ba_3Ce(PO_4)_3$ at 600°C in dry and wet 4vol% hydrogen were 4.04×10^{-5} and 1.46×10^{-4}S/cm, respectively, less than those of BCGO. The proton transference number was around 0.8 at 600°C in hydrogen concentration cells. Therefore, the electronic transference number was about 0.2. $Ba_3Ce(PO_4)_3$ is a mixed conductor with dominant proton conduction. However, neither its proton nor electron conductivity is high enough for hydrogen separation. Composites of CeO_2-$Ba_3Ce(PO_4)_3$ were also prepared. However, the electronic conductivity provided by the hopping between Ce^{3+} and Ce^{4+} was also not high enough to allow hydrogen separation in the composite CeO_2-$Ba_3Ce(PO_4)_3$.

The results of Raman spectroscopy and magic-angle spinning nuclear magnetic resonance (MAS-NMR) showed the local structures of $Ba_3Ce(PO_4)_3$ under different atmospheres. Free hydrogen can be oxidized forming protons and incorporated into the lattice. In the presence of water vapor, bound hydrogen is produced and oxidized forming protons. The formed protons attach onto the O atoms of PO_4 group and are incorporated into the lattice. The defect structure of $Ba_3Ce(PO_4)_3$ was proposed. The conductivities of $Ba_3Ce(PO_4)_3$ as a function of oxygen partial pressure or water partial pressure supported the proposed defect structure.

CHAPTER 1
INTRODUCTION

1.1 Application of Proton Conducting Material

Due to dwindling natural energy resources and increased concern over the environment, more attention is being paid to clean and efficient fuels such as hydrogen. For example, the efficiency of an internal combustion engine is 20%, but the efficiency of a fuel cell is above 33% when running on pure hydrogen. Fuel cells produce no pollution and the only byproduct is water [1]. It is expected that hydrogen consumption will increase dramatically in the future with the wider application of fuel cells.

Inexpensive and abundant sources of hydrogen such as coal gasification, natural gas reforming, and off gas streams from various process industries usually contain hydrogen mixed with other gases. The largest quantities of hydrogen are produced from syn gas. Hydrogen separation membranes are thin materials through which pure hydrogen is selectively permeated from a hydrocarbon based gas mixture. They are important to enable a more widespread and economic use of hydrogen.

There are many kinds of hydrogen separation membranes. One type is a composite consisting of a porous ceramic support and a Pd metal film. Hydrogen is permeated exclusively by the metal film and the ceramic provides the mechanical strength but the Pd cost is prohibitively high [2-5]. A second type is the crystalline, inorganic molecular sieve membrane for hydrogen separation. Crystalline frameworks have tunnel pores that are capable of size exclusion separation [6-9]. The other kinds are perovskites or related type materials which are mixed conductors. In recent years, some materials with different

structures have also been developed; however, the hydrogen flux is low compared with the oxygen membrane and more research is needed before commercialization is practical.

1.2 Proton Conducting Materials

1.2.1 Proton Conductor

The proton has no electron shell. It resides within an associated anion's electron shell. The small size of protons makes it difficult to jump from one site to another unassisted. Protons usually do not occupy lattice positions in oxides but attach to oxide ions, forming $OH_{\ddot{O}}$ group. Proton conduction in perovskites was first discovered in $SrCeO_3$ [10]. Since then, a series of doped perovskite oxides ABO_3 (A =Ba, Sr, B =Ce, Zr) have been studied [11-26]. Trivalent dopants at B site are charge compensated by the oxygen vacancies $V_{\ddot{O}}$. Protons replace oxygen vacancies in the presence of water vapor. They also can be incorporated into lattice in the hydrogen-rich atmosphere.

The proton transport usually has two mechanisms [27-29]: the transport of protons between relatively stationary host anions, known as the Grotthuss or free-proton mechanism, and the transport with other species, termed the vehicle mechanism.

Proton conducting materials can be used as an electrolyte in a cell, whose driving force is an external voltage. When a gas mixture containing hydrogen is applied at the anode, hydrogen will be oxidized forming protons. These protons will enter the membrane and travel to the cathode. At the cathode they will be reduced back to hydrogen molecules. This process results in separation of hydrogen from other species present at the anodic side [30-31].

Ideal hydrogen separation membrane materials should be mixed ionic-electronic conductors (MIEC), which not only have high proton conductivity but also have high

electronic conductivity and no oxygen ionic conductivity. In addition, the proton and electronic conductivities should be nearly equal and sufficiently high ($> 5\times10^{-2}$ Scm^{-1}). Materials must also exhibit high catalytic activity for the dissociation and recombination of hydrogen at gas/solid interfaces [32]. In that case, the hydrogen separation process will have high hydrogen permeation and will not need any external electrical source.

1.2.2 $BaCeO_3$ Based Proton Conductors

Barium cerates doped with lower valent cations on the Ce site are high temperature proton conductors, which can be used as the electrolytes in a fuel cell or hydrogen separation membrane. $BaCe_{0.85}Gd_{0.15}O_3$ (BCGO) exhibits the highest proton conductivity in the $BaCeO_3$ family.

Doping of Gd^{3+} on the Ce site of $BaCeO_3$ can be written as

$$Gd_2O_3 \xrightarrow{BaCeO_3} 2Gd'_{Ce} + 3O_o^x + 3V_o^{\cdot\cdot} + 2V_{Ba}'' . \qquad (1\text{-}1)$$

Kroger-Vink notation [33] is used for point defects in the above formula.

The proton incorporation in a hydrogen atmosphere follows the reaction:

$$\frac{1}{2}H_2 + O_o^x = OH_o + e' . \qquad \text{K1} \qquad (1\text{-}2)$$

The proton incorporation in wet atmosphere follows the reaction:

$$H_2O + V_O^{\cdot\cdot} + O_o^x = 2OH_o . \qquad \text{K2} \qquad (1\text{-}3)$$

Reaction (1-2) indicates that annealing in hydrogen atmosphere incorporates protons and an equal number of electrons. Reaction (1-3) suggests that incorporation of protons by annealing in water vapor will change the ionic conductivity by reducing the number of oxygen vacancies and creating $OH_o^{\cdot}$ groups.

The reaction may be split into the formation of ion vacancies and the formation of protons [34]:

$$O_O^x + 2h^{\cdot} = V_{\ddot{O}} + \frac{1}{2}O_2 \qquad \text{K3} \qquad (1\text{-}4)$$

$$H_2O + 2h^{\cdot} + 2O_O^x = 2OH_{\ddot{O}}^{\cdot} + \frac{1}{2}O_2 . \qquad \text{K4} \qquad (1\text{-}5)$$

The internal electron-hole pair formation follows the reaction:

$$null = e^{'} + h^{\cdot} . \qquad \text{K5} \qquad (1\text{-}6)$$

The electroneutrality condition for Gd doped barium cerate is

$$[h^{\cdot}] + 2[V_{\ddot{O}}^{\cdot\cdot}] + [OH_{\ddot{O}}^{\cdot}] = [Gd_{Ce}^{'}] + [e^{'}] . \qquad (1\text{-}7)$$

For the low water partial pressure condition, three different Brouwer-type charge neutrality conditions are ($e^{'}$, $V_{\ddot{O}}^{\cdot\cdot}$), ($Gd_{Ce}^{'}$, $V_{\ddot{O}}^{\cdot\cdot}$) and ($Gd_{Ce}^{'}$, $h^{\cdot}$) for low, intermediate and high oxygen partial pressure regions, respectively [35]. For the high water partial pressure condition, three different Brouwer-type charge neutrality conditions are ($e^{'}$, $OH_{\ddot{O}}^{\cdot}$), ($Gd_{Ce}^{'}$, $OH_{\ddot{O}}^{\cdot}$) and ($Gd_{Ce}^{'}$, $h^{\cdot}$) for low, intermediate and high oxygen partial pressure regions, respectively [35].

When the concentration of electronic charge carriers is neglected, the solution for the concentration of proton defects is

$$[OH_{\ddot{O}}^{\cdot}](P_{H_2O}) = \frac{1}{4}K_2 P_{H_2O}\left(\sqrt{1 + \frac{8[Gd_{Ce}^{'}]}{K_2 P_{H_2O}}} - 1\right) \text{ [34].} \qquad (1\text{-}8)$$

For the low P_{H_2O} condition, $[OH_{\ddot{O}}^{\cdot}]$ corresponds to Sievert's law:

$$[OH_{\ddot{O}}^{\cdot}](P_{H_2O}) = \sqrt{\frac{1}{2}K_2[Gd_{Ce}^{'}]P_{H_2O}} \text{ . [34]} \qquad (1\text{-}9)$$

The proton conductivity of $BaCe_{0.85}Gd_{0.15}O_3$ is theoretically proportional to $P_{H_2O}^{1/2}$ and it is a good proton conductor at high temperature. However, the electronic

conductivity of $BaCe_{0.85}Gd_{0.15}O_3$ is not high enough for hydrogen separation. Krishnamurthy [36] addressed this problem by using a two-phase composite membrane, which consisted of $BaCe_{0.85}Gd_{0.15}O_3$ ceramic material and a metallic component, Pd. In this composite BCGxPd (x: the volume percent of Pd in the composite), Pd provided an internal conduction path for electronic transport and the ceramic matrix facilitated proton transport.

Figure 1-1 shows the total conductivity of BCGO and Pd–BCGO composites. Composites BCG35Pd and BCG15Pd were synthesized by solid state reaction. BCG1Pd composite was synthesized by wet impregnation process. BCG5Pd composite was synthesized by electroless deposition process. In the composites BCG1Pd and BCG5Pd, Pd was coated on the surface of BCGO powders to obtain a continuous path of Pd in grain boundaries of sintered BCGO-Pd composites. In the composite BCG35Pd, the volume fraction of the component Pd was 0.35 and there existed a continuous network of Pd in the BCGO. Under this condition, Pd was said to have established a percolation path in the matrix BCGO [37]. The conductivity of BCG35Pd increased with decreasing temperature indicative of metallic conduction. This also indicated that an electronic path was established in the BCG35Pd composite. The bulk conductivity of BCG1Pd or BCG5Pd is lower than that of BCGO in wet 10vol% hydrogen, which is shown in figure 1-2 (a). The grain boundary conductivity decreases with increasing Pd concentration in the composite, which is shown in figure 1-2 (b). This may be caused by a grain boundary phase [36].

Figure 1-3, 1-4 and 1-5 show the hydrogen flux through BCGO, BCG1Pd, and BCG5Pd, respectively, as a function of time at 650 °C. Figure 1-6 shows the hydrogen

flux as a function of temperature through different systems. The low hydrogen flux of BCGO was expected due to its lack of electronic conductivity. The hydrogen flux of BCG1Pd shown was significantly higher in contrast to the lower conductivity of BCG1Pd. This was because the electronic conductivity was the limiting factor in hydrogen permeation when Pd content was low [36].

Hydrogen flux of BCG5Pd increased with time at 650 °C in Figure 1-5. The hydrogen flux kept this increasing trend for 20 hours until the feed gas was shut off. Hydrogen flux of BCG5Pd demonstrated better hydrogen permeability than that of BCG35Pd when temperature was lower than 550 °C as shown in Figure 1-6. It was unusual compared with other materials, whose hydrogen flux became stable within several hours. The second phase Pd did not exhibit such a trend under isothermal condition. The BCG5Pd was unique in its synthesis and some impurity could be introduced into the composite causing formation of a tertiary phase at high sintering temperatures. It was the tertiary phase that contributed to such an unusual trend. This tertiary phase was expected to be a good mixed ionic electronic conductor or at least a good proton conductor.

To identify this tertiary phase from composite BCG5Pd and synthesize it is the main objective of this research work. Conductivity and hydrogen permeability of this tertiary phase material around 600 °C needed to be checked to assure whether or not it is a good proton conductor as expected. As shown in figure 1-7 [38], there is a gap for proton conductor in the 300~600 °C range. This intermediate temperature range is very important for fuel cell and hydrogen separation. If this tertiary phase material is a good

proton conductor, it will be an important development in fuel cells and hydrogen separation research.

BCG5Pd powders synthesized by Krishnamurthy were characterized by X-ray diffraction and infrared spectroscopy. Characterization results in chapter 3 suggest that the tertiary phase is most likely the barium cerium phosphate. Doped phosphates are reported as proton conductors; however, their conductivities are not as high as those of perovskites. Therefore, barium cerium phosphate, as the tertiary phase, is most likely a proton conductor, but its conductivity behavior is unknown. To explore this hypothesis, barium cerium phosphate was synthesized and characterized in chapter 4. Corresponding defect structures were proposed based on the characterization results. Its total conductivity and ionic transference number were measured and discussed in chapter 5 and 6, respectively. Its possible use as hydrogen separation membrane was attempted in chapter 7. Finally, conclusions about this new proton conducting material were drawn in chapter 8.

1.3 Experimental Techniques

1.3.1 Synthesis

Coprecipitation refers to a process in which components precipitate simultaneously by the formation of mixed crystals, or by adsorption, or mechanical entrapment. It generally produces an intimate mixture of precipitates. The mixture is calcined at an elevated temperature to produce the desired chemical composition and crystalline phase.

1.3.2 Common Characterization

Powder X-ray diffraction (XRD) is an essential technique for phase identification and crystal structure refinement. A scanning electron microscope (SEM) in conjunction with energy dispersive spectroscope (EDS) is used to examine microstructure and

chemical features. A transmission electron microscope (TEM) is used to characterize the microstructure at higher magnification.

In addition, vibrational and nuclear magnetic resonance (NMR) spectroscopes are very important methods, especially in the study of solid phosphate. These methods characterize the local environments around phosphates.

1.3.2.1 Infrared (IR) and Raman spectroscopy

Each atom has three degrees of freedom due to its motions along the Cartesian coordination axes. Therefore, a molecule with N atoms has 3N degrees of freedom, which describe the translation, rotation and vibration of molecules. Translation refers to the motion of the entire molecule through the space and it has 3 degrees of freedom. Rotation refers to the rotation of the entire molecule and it has 3 degrees of freedom for nonlinear molecules and 2 degrees of freedom for linear molecules. Vibration refers to the continuous vibrations of all atoms in the molecules respective to each other. It has 3N-6 degrees of freedom for nonlinear molecules and 3N-5 degrees of freedom for linear molecules.

Molecule vibrational spectroscopy is relatively complicated. Quantum mechanics only allows certain vibrational frequencies, which are known as the normal molecule vibrational modes. There are several types of motions and some examples are

- Stretching motion between two bonded atoms
- Bending motion between three atoms connected by two bonds.

Infrared spectroscopy characterizes molecule vibrations by measuring the light absorption, whose frequency matches the vibrational excitation energy of a molecule from low energy states to higher energy states. For a vibration to be IR active, the

molecule dipole moment must change. The Raman effect is due to the interaction of a molecule with the electromagnetic field of the incident radiant. For a vibration to be Raman active, the molecule polarizability must change [39].

Infrared spectroscopy and Raman spectroscopy are used to study the local symmetry of the phosphate groups. Characteristic group frequencies of orthophosphates and diphosphates are mentioned in many references [40-42]. Both IR and Raman spectra of orthophosphates have no band at 700-900cm^{-1}. The IR spectrum of a tetrahedral symmetric orthophosphate anion is characterized by a strong stretching mode at around 1000 cm^{-1} and a strong bending mode at 500-600 cm^{-1}. Diphosphates are distinguished from orthophosphates by the P-O-P bridge vibrations. For diphosphates, the asymmetric P-O-P stretching mode at 900-950cm^{-1} is strong in the IR spectrum and the symmetric P-O-P stretching mode around 750cm^{-1} is strong in the Raman spectrum. However, vibrations are no longer characteristic of the anion alone if the M-O (P) bonds in the lattice are strong.

Table 1-1 lists the infrared and Raman stretching frequency ranges for phosphate anions in the solid state [40]. Table 1-2 also lists the infrared and Raman characteristic group frequencies of acid phosphates [41]. Table 1-3 lists the Fourier transform Raman shifts and assignments of Sr-doped $LaPO_4$, which reveals that HPO_4^{2-} and $P_2O_7^{4-}$ exist in Sr-doped $LaPO_4$ under wet and dry conditions, respectively, in addition to PO_4^{3-} [42].

1.3.2.2 Nuclear Magnetic Resonance spectroscopy

When an atom is placed in a magnetic field, its electrons will circulate about the direction of the applied magnetic field. This circulation causes a small opposite magnetic field at the nucleus. The effective magnetic field at the nucleus is therefore generally less

than the applied field. This phenomenon is called nuclear magnetic resonance (NMR). NMR spectroscopy is the use of the NMR phenomenon to study physical, chemical and biological properties of materials [40].

The electron density around each nucleus varies according to the types of nuclei and bonds in the molecule. The opposing field and the effective field at each nucleus will vary. This is called the chemical shift phenomenon and related with local environments. The chemical shift of a nucleus is the difference between the resonance frequency of the nucleus and reference. The chemical shift is given the symbol δ, which can be expressed as

$$\delta = (\upsilon - \upsilon_{ref}) \times 10^6 / \upsilon_{ref} \quad (1\text{-}10)$$

where υ and υ_{ref} are resonance frequencies of the nucleus and reference, respectively.

MAS-NMR spectroscopy was applied to investigate the defect structures in Sr doped $LaPO_4$ [42]. It was carried out with the Bruker MSL-300 spectrometer with an operating frequency of 300.13 MHz for ^1H and 121.50 MHz for ^{31}P. The spinning speed was 10 kHz. The chemical shifts for ^1H and ^{31}P were given with respective to tetramethylsilane (TMS) and 85% phosphoric acid, respectively. Table 1-4 shows the chemical shift of ^1H and ^{31}P in Sr doped $LaPO_4$ [42].

1.3.3 Electrochemical Characterization

1.3.3.1 Conductivity measurement

When a constant electric field is applied to material, a steady-state current may result. The ratio of this current to the applied electric field is proportional to a material property, which is known as conductivity. Conductivity is defined as the conductance of a cube of material of unit cross section. In ceramics, ionic conduction is caused by

migration of ions in an electric field and electronic conduction is caused by the migration of mobile electronic carriers. Both ionic and electronic conductivity contribute to the total conductivity. The total conductivity σ_{total} is given by

$$\sigma_{total} = \sum_i c_i |z_i| e \mu_i \tag{1-11}$$

where μ_i is the electric mobility, c_i is the number of mobile carriers per unit volume, z_i is the net charge of the moving ion.

Conductivity can be measured by several techniques such as four-point method, AC impedance measurement and I-V relations. Small amplitude AC impedance measurement can be used to determine the bulk, grain boundary and the electrode characteristics. Their responses can be described as a capacitor connected with a resistor in parallel. Parameters such as oxygen partial pressure, sample length and grain size can be varied to identify the bulk, grain boundary and the electrode effect. Raising the temperature will enhance the contribution of the process with the higher activation energy. Variation in oxygen partial pressure influences the electrode parameter and can affect the bulk conductivity, depending on defect equilibrium. Increasing the sample length increases the bulk impedance. Increasing the grain size reduces the impedance associated with the total grain boundary.

1.3.3.2 Transference number measurement

The transference number t_i characterizes the contribution of each mobile carrier to the current in a material. The knowledge of t_i for all components i is very important for understanding the electrolytic process. It is defined as

$$t_i = \frac{\sigma_i}{\sigma_{total}} = \frac{\sigma_i}{\sum_i \sigma_i}. \tag{1-12}$$

In proton conducting ceramics, total conductivity includes ionic conductivity (σ_{ion}) and electronic conductivity (σ_{elec}). Ionic conductivity includes contributions from oxygen vacancies $V_{\ddot{O}}$ and protons OH_O. Electronic conductivity includes contributions from electrons $e^{'}$ and electron holes $h^{\cdot}$. Therefore, the contribution of ionic conductivity and electronic conductivity can be expressed as

$$\sigma_{total} = \sigma_{ion} + \sigma_{elec} = \sigma_{ion} + \sigma_{e^{'}} + \sigma_{h} = \sigma_{OH_O} + \sigma_{V_O} + \sigma_{e^{'}} + \sigma_{h} \tag{1-13}$$

$$t_{OH_o} = \frac{\sigma_{OH_O}}{\sigma_{total}} \tag{1-14}$$

$$t_{ion} = \frac{\sigma_{ion}}{\sigma_{totol}} \tag{1-15}$$

$$t_{ion} + t_{elec} = 1 \tag{1-16}$$

where t_{ion} is the ionic transference number, t_{elec} is the electronic transference number, t_{OH_O} is the proton transference number and t_{V_O} is the oxygen ionic transference number.

There are many methods to determine the transference number, such as measurement of permeation, Hebb-Wagner polarization and electromotive force (EMF) measurement. In EMF measurement, the material is used as an electrolyte in a galvanic cell. If it is a pure ionic conductor, EMF of the cell is given by the equation $\Delta G = -nFE$, where ΔG is the Gibbs free energy of the cell reaction, F is the Faraday constant and n is the number of Faraday equivalents which flow through the cell. If this material also has electronic conductivity, the experimental value of the EMF is smaller than the theoretical one. Therefore, ionic transference number $t_{ion} = \frac{E_{measurement}}{E_{theoretical}}$ is obtained.

1.3.3.3 Hydrogen permeation

Hydrogen permeation can be defined as a process by which pure hydrogen is selectively passed through a separation membrane from a gas mixture. The hydrogen permeation process is a kinetic process, which is controlled by the bulk transport and surface exchange. The exchange of hydrogen between the surface and the gas phases involves adsorption, dissociation, charge transfer, surface diffusion of intermediate species, and, finally, incorporation in the surface layer. During bulk transport, the hydrogen is transported through the membrane in the form of protons, rather than molecules, under the driving force of a gradient in hydrogen chemical potential. Protons are charge compensated by a simultaneous flux of electrons.

Generally, the hydrogen permeation flux J_{OH_O} across an oxide membrane can be calculated using the Wagner equation, which assumes the bulk diffusion to be the rate-limiting step [35].

$$J_{OH_O} = -\frac{1}{L}\left[\frac{RT}{4F^2}\int_{P'_{O_2}}^{P''_{O_2}}\sigma_{total}t_{OH_O}t_{V_O}\,d\ln P_{O_2} + \frac{RT}{2F^2}\int_{P'_{H_2}}^{P''_{H_2}}\sigma_{total}t_{OH_O}(t_{V_O}+t_{e'})\,d\ln P_{H_2}\right] \quad (1\text{-}17)$$

where L is the thickness of the membrane, R is the universal gas constant; F is the Faraday constant and $d\ln P$ is the chemical potential gradient across the membrane.

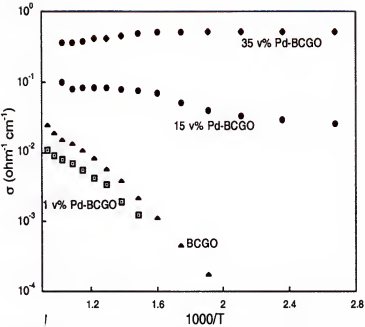

Figure 1-1. Total conductivity of BCGO and Pd-BCGO composite (from ref [36]).

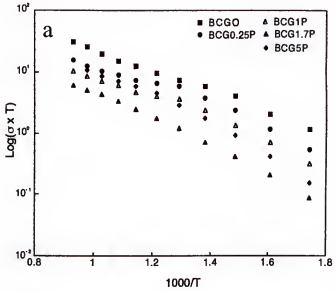

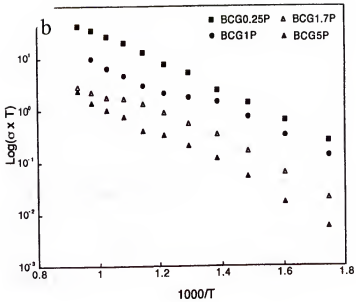

Figure 1-2. Conductivity of various systems in wet 10vol% hydrogen. (a) Bulk conductivity and (b) grain boundary (from ref [36]).

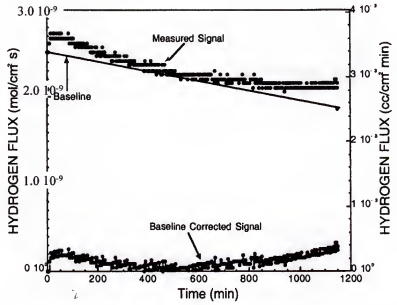

Figure 1-3. Hydrogen flux of BCGO with time at 650 °C (from ref [36]).

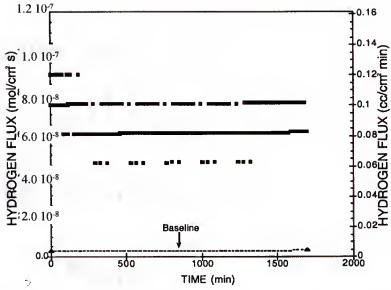

Figure 1-4. Hydrogen flux through BCG1Pd with time at 650 °C (from ref [36]).

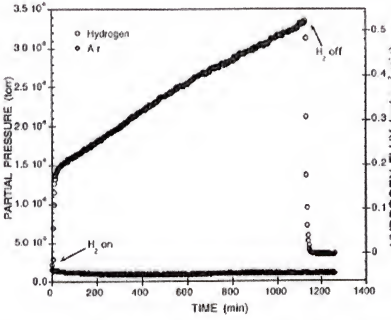

Figure 1-5. Hydrogen flux through BCG5Pd with time at 650 °C (from ref [36]).

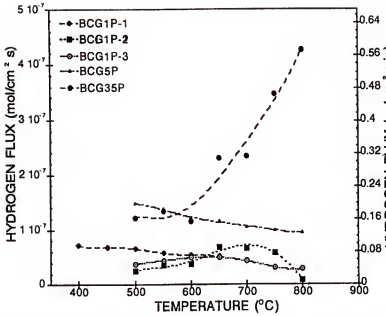

Figure 1-6. Hydrogen flux as a function of temperature through different system (from ref [36]).

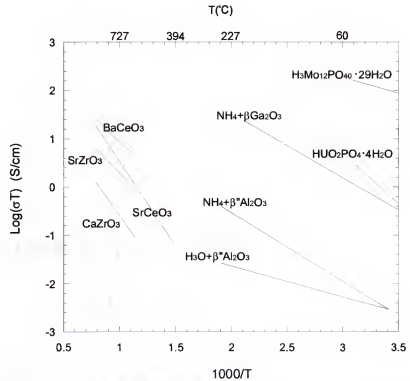

Figure 1-7. Conductivity in some proton conductors as a function of temperature (from ref [38]).

Table 1-1. Infrared and Raman stretching frequency ranges for phosphate anions.

Anion	Infrared (cm^{-1})	Raman (cm^{-1})
PO_4^{3-}	1000-1070, strong, asymmetric, PO_4	930-970, strong, symmetric, PO_4
$P_2O_7^{4-}$	720-750, weak, symmetric, POP 900-950, strong, asymmetric, POP 1070-1120, strong, asymmetric, PO_3	720-750, strong, symmetric, POP 1010-1020, strong, symmetric, PO_3

Data from ref [40].

Table 1-2. Infrared and Raman functional group frequencies.

Functional Group	Region cm^{-1}	Intensity IR	Raman
PO_4^{3-}	475		medium
	1180-1000	strong	strong
	1000-900		strong
	580-540	very week	weak-medium
	415-380		weak-medium
$P_2O_7^{4-}$	1220-1060	strong	medium-strong
	1060-960	weak-medium	strong
	980-850	medium	weak
	770-700	medium-weak	weak-medium
	600-500	medium-strong	weak-medium
	530-400		weak-medium
	355-315		weak
HPO_4^{2-}	2900-2750	medium	medium-weak
	2500-2150	weak	strong
	1900-1600	weak	
	1410-1200	weak	
	1220-1100		medium-strong
	1150-1000	strong	strong
	1110-925	medium-weak	medium
	920-825	medium-weak	weak
	580-450	weak	
	430-390	weak	
$H_2PO_4^-$	2700	weak	medium-weak
	2400-2200	weak	strong
	1700	weak	
	1250	strong-medium	
	1200-950	strong	medium-strong
	950-850	strong	strong
	580-540	weak	medium
	450-350		medium-strong

Data from ref [41].

Table 1-3. Reported Raman shifts of Sr doped $LaPO_4$.

Functional Group	Raman (cm^{-1})	
HPO_4^{2-}	1135 and 672	P-O-H in plane and out–of–plane deformation mode
$P_2O_7^{4-}$	1036, 764 and 728	
PO_4^{3-}	1073, 1065, 1055 and 1025	asymmetric stretching mode
	991 and 967	symmetric stretching mode
	619, 589,571,559 and 537	O-P-O F2-bending mode
	466,416 and 395	O-P-O E-bending mode

Data from ref [42].

Table 1-4. Chemical shift of ^1H NMR and ^{31}P NMR in Sr doped $LaPO_4$.

High resolution ^1H MAS-NMR	
Water molecules	5.4 and 1.2 ppm
Proton in the crystals	12.4 ppm, relaxation time is shorter, intensity increases with doping concentration
High resolution ^{31}P MAS-NMR	
Orthophosphate ions PO_4^{3-}	-4.4 ppm
Protons near phosphorus	-30.6 ppm, relaxation time is shorter, intensity increases with doping concentration
Pyrophosphate $P_2O_7^{4-}$	-7.2 and –8.4 ppm

Data from ref [42].

CHAPTER 2
REVIEW OF PROTONIC CONDUCTORS

2.1 Introduction

As pointed out in the first chapter, if the tertiary phase in composite BCG5Pd is a good proton conductor between 300 and 600 °C, it would be an important development in fuel cells and hydrogen separation. BCG5Pd was synthesized by a unique process, electroless deposition. In this process, BCGO particles were suspended in an electroless solution containing palladium chloride and ammonium hydroxide. Hypophosphite was used as the reducing agent to deposit Pd on the surface of BCGO particles from an electroless bath. The coated particles were separated from solution by filtration and washed several times to remove salts. However, some impurity was still absorbed during the process. Based on information about the synthesis process of BCG5Pd, the tertiary phase is more likely to be a phosphate. Phosphates with or without structure protons have been studied recently as proton conductors at intermediate temperatures. In this chapter, the research status of proton conduction, defect structure, transference number and hydrogen permeation of phosphates is reviewed.

2.2 Proton Conduction in Phosphates

Most recent research about proton conduction in phosphates focused on doped lanthanum phosphate, $LaPO_4$. According to JCPDS 32-0493, $LaPO_4$ crystallizes in space group $P2_1/n$ (14) with lattice parameter a=6.8366 Å, b=7.0769 Å, c=6.5095 Å and β= 103.23°. It has a low symmetry monoclinic monazite structure. Figure 2-1 approximately illustrates the relative position of elements and the bond lengths in the structure [43]. The

monazite structure is composed of PO_4 tetrahedra and LaO_9 edge sharing polyhedra, which is clearly shown in figure 2-2 [44]. In the reported lanthanum phosphate studies, La sites were usually substituted by alkaline earth metals or by a composition of rare earth elements. The substitution leads to the formation of oxygen vacancies for charge balance. The protons are introduced into the lattice through the equilibrium between oxygen vacancies and water vapor. The conductivities of doped $LaPO_4$ were usually measured in air or oxygen. Their conductivities were higher under the wet atmosphere than under the dry atmosphere, indicating dominant proton conduction in the presence of water vapor. Doped $LnPO_4$ (Ln= Pr, Nd and Sm) and YPO_4 were also investigated [45-51]. No literature reported proton conductivity data measured in a hydrogen atmosphere. Compared with perovskite type oxides, conductivities of doped phosphates were lower when temperature was higher than 300 ºC. The following are some details of recent research.

2.2.1 Proton Conduction in Doped $LaPO_4$

Norby studied proton conduction in Ca and Sr substituted $LaPO_4$ in air, wet air and air with D_2O [26-27]. The magnitude of the isotope effect, although smaller than the ratio of 1.37 expected for classical free proton jump migration, was high enough to identify a major contribution from proton conductivity. The proton conductivity went through a maximum as a function of temperature. This maximum occurred at approximately 950 and 850 ºC, for Ca and Sr substituted sample in wet air, respectively. At 800 ºC, the proton conductivity was about 6×10^{-5} and 3×10^{-4} S cm^{-1} for Ca and Sr substituted $LaPO_4$ in wet air, respectively. The activation energy for proton mobility was approximately 0.8 eV.

Gallini took impedance spectra on the 2.5 mol% and 5 mol% Sr doped $LaPO_4$ in wet and dry oxygen [45]. The conductivity of 5 mol% doped $LaPO_4$ was around 2×10^{-5} S/cm at 600 °C in the wet oxygen, higher than that of 5 mol% doped $LaPO_4$. The bulk resistance dominated above 400 °C and grain boundary resistance dominated below it. Water vapor was incorporated to hydrolyze the $P_2O_7^{4-}$ group into two HPO_4^{2-} groups. The entropy and enthalpy changes of the incorporation were –90 J/mol·K and –83 KJ/mol, respectively.

Amezawa investigated electrical conduction in $LaPO_4$ doped with 1 mol% of alkaline earth metal M (M= Mg, Ca, Sr and Ba) at 500-925 °C [46-47]. Conductivities of 1 mol% Sr, Ca , and Ba doped $LaPO_4$ in wet oxygen at 500 °C are 5×10^{-6}, 4×10^{-6} and 2×10^{-6} S/cm, respectively. The conductivity of Mg doped $LaPO_4$ in wet oxygen was lower, only 2×10^{-6} S/cm at 600 °C. Ca, Sr, and Ba doped $LaPO_4$ conducted protons dominantly under the wet atmosphere but Mg doped $LaPO_4$ did not. The activation energy for proton conduction in the Ca, Sr, Ba doped $LaPO_4$ at 500-600°C are 0.95, 0.98 and 0.79 eV, respectively. Their conductivity differences originated from the solubility differences of the alkaline earth metals in the $LaPO_4$. The solubility limits of Ca, Sr and Ba in $LaPO_4$ are 4.2%, 1.9% and 0.4%, respectively.

Amezawa also investigated the conductivities of Sr doped $LaPO_4$ with different sintering temperatures and different dopant concentrations (Sr = 0-7 mol%) [42]. Sr doped $LaPO_4$ sintered at 1350 °C had a second phase, $Sr_2P_2O_7$, and lower conductivity than that sintered at 1200 °C. The conductivity of $(x/2)/Sr_2P_2O_7$-$(1-x)LaPO_4$ (x= 0-0.6) showed a maximum when x= 0.02-0.03, which nearly equaled the solubility limit of Sr in the $LaPO_4$ [48]. $Sr_2P_2O_7$ appeared as a second phase with sintering temperature 1200 °C

when x>0.02. The proton activation energy of $(x/2)/Sr_2P_2O_7$-$(1-x)LaPO_4$ (x= 0.02) was 0.86 eV at 500-600 ºC.

Kitamura investigated the electrical conduction in 1 mol% Sr doped $(La_{1-x}Sm_x)PO_4$ (x= 0.3, 0.5 and 0.7) [49].The conductivities of 1 mol% Sr doped $(La_{1-x}Sm_x)PO_4$ (x=0.3, 0.5, 0.7) are at the same magnitude –5 at 600 ºC in wet oxygen atmosphere and did not increase much with the increased Sm content. The activation energies are 0.975, 0.91, 0.92, 0.94 and 0.96 eV for x=0, 0.3, 0.5, 0.7 and 1, respectively.

2.2.2 Proton Conduction in Other Phosphates

Ca doped YPO_4 has a tetragonal xenotime-type structure. Amezawa investigated its electrical conductivity under 0.4-8 kPa of water partial pressure and 0.01-100 kPa of oxygen partial pressure [50]. The conductivity of the 3 mol% Ca doped YPO_4 was 4×10^{-6} S/cm at 500ºC in wet conditions. The proton activation energy was estimated as 0.84 eV at 500-700 ºC.

$LnPO_4$ (Ln=La, Pr, Nd and Sm) has a monazite structure. Kitamura measured the electrical conductivity of $LnPO_4$ and 1 mol% Sr doped $LnPO_4$ [51]. The conductivities of 1 mol% Sr doped $LnPO_4$ under wet oxygen atmosphere were $10^{-5.5}$ S/cm at 500 ºC and were about 10 times higher than those of undoped $LnPO_4$. The conductivities of undoped $LnPO_4$ were almost independent of humidity. The conductivities of 1 mol% Sr doped $LnPO_4$ were drastically increased under wet atmosphere compared with those under dry atmosphere. Conductivities of 1 mol% Sr doped $LnPO_4$ (Ln= La, Pr, Nd and Sm) were almost independent of rare earth elements. The activation energies at 500-600 ºC were estimated to be 0.98, 0.91, 0.92 and 0.96 eV for Ln=La, Pr, Nd and Sm, respectively.

Baranov reported conductivity of single crystal $Pb_3(PO_4)_2$ increased 20-40 times the original value after annealing in wet nitrogen [52]. Transmission IR spectra of $Pb_3(PO_4)_2$ after annealing in wet nitrogen or air showed a broad band at 3250 and a doublet at 2750-2800 cm^{-1}, which were characteristic of the stretching vibration of two different types of hydrogen bonding.

Haile reported conductivity of a new compound $\beta - Cs_3(HSO_4)_2(H_X(P,S)O_4)$ in ambient air and dry argon from room temperature to the thermal decomposition temperature 190 °C [53-54]. The compound went through a superprotonic transition at 125 °C. Its conductivity jumped from 2×10^{-5} to 6×10^{-3} S/cm. The activation energy was 0.70 eV at low temperature and 0.37 eV at high temperature. Its low temperature conductivity was about one magnitude greater than that of $\alpha - Cs_3(HSO_4)_2(H_2PO_4)$ [55] and about two orders of magnitude greater than that of $CsHSO_4$ [56]. She also studied $Cs_5(HSO_4)_3(H_2PO_4)_2$ [57] and $Cs_2(HSO_4)(H_2PO_4)$ [58]. The conductivity of $Cs_2(HSO_4)(H_2PO_4)$ in the high temperature phase at 110 °C was 3×10^{-3} S/cm and the activation energy for proton transport was 0.37 eV.

Otomo carried out conductivity measurements of polycrystalline CsH_2PO_4 and CsH_2PO_4/silica composite from 150 to 250 °C under dry and wet argon atmosphere [59]. The melting point of CsH_2PO_4 was 345 °C. A sudden ionic conductivity-jump took place at around 230 °C. D-H isotopic exchange suggested that CsH_2PO_4 was a proton conductor. The conductivity maintained the constant value 1×10^{-2} S/cm during 20 h in wet atmosphere but it decreased from 1×10^{-4} S/cm with time in dry atmosphere at 250 °C. In CsH_2PO_4/silica composite systems, the conductivity was influenced by hydrophilicity

and the specific surface area of silica. The hydrophilic silica accelerated the conductivity at the temperature approximately below the phase transition.

Alberti also mentioned other phosphates exhibited proton conducting behavior only when hydrated. The proton conductivity of $HUO_2PO_4 \cdot 4H_2O$ at room temperature was 5×10^{-3} S/cm and activation energy was 0.35 eV [60-61]. The proton conductivity of $\alpha - Zr(HPO_4)_2 \cdot nH_2O$ was 1×10^{-4} S/cm and its activation energy was 0.3 eV at room temperature [62]. Its conductivity increased to 1.5×10^{-4} S/cm with 97% relative humidity at 100 ºC [63]. The proton conductivity of $\gamma - Zr(PO_4)(H_2PO_4)\cdot 2H_2O$ was 3×10^{-4} S/cm and its activation energy was 0.24 eV at room temperature [64]. Its conductivity maintained 3×10^{-4} S/cm with 95% relative humidity at 100 ºC [65]. The proton conductivity of polybenzimidazole·xH_3PO_4 was 4×10^{-2} S/cm with 11% relative humidity at 190 ºC [66].

2.3 Proton Incorporation Mechanism in Phosphates

The proton incorporation mechanism in phosphates is still not clearly understood. Norby, Amezawa and Haile proposed the following defect structures based on their experimental results.

2.3.1 Norby's Hypothesis

Due to the complexity of the proton incorporation, Norby proposed two mechanisms. He initially assumed that dopant Ca or Sr dissolved on the La site in $LaPO_4$ and the native compensating defect was an oxygen vacancy [26-27].

The electroneutrality could be written as

$$2[V_{\ddot{O}}] + [H_i] = [M'_{La}] = \text{constant (M= Ca, Sr).} \quad (2\text{-}1)$$

The external equilibrium between oxygen vacancies and protons can be written as

$$V_{\ddot{O}} + H_2O(g) = 2H_i + O_O^{\times} \tag{2-2}$$

$$K_a = [H_i]^2[V_{\ddot{O}}]^{-1} p_{H_2O}^{-1}. \tag{2-3}$$

Oxygen vacancies were considered to be dominant at high temperature and the electroneutrality in (2-1) was simplified as

$$2[V_{\ddot{O}}] = [M_{La}^{'}] = \text{constant (M= Ca, Sr).} \tag{2-1a}$$

Equation (2-3) can then be written as

$$[H_i] = K_a^{1/2}[M_{La}^{'}]^{1/2} p_{H_2O}^{1/2}. \tag{2-3a}$$

Proton concentration $[H_i]$ should be proportional to $p_{H_2O}^{1/2}$ based on equation (2-3a). Experimental results showed that the conductivities of Ca or Sr doped $LaPO_4$ were approximately $p_{H_2O}^{1/3}$ dependent at 800 ºC at the high water partial pressure.

Because the experimental conductivity dependence of water partial pressure is lower than the theoretical dependence deduced from his first hypothesis, Norby came up with an alternative defect model comprised of protons and oxygen interstitials, which are formed through the reaction:

$$H_2O(g) = 2H_i + O_i^{''} \tag{2-4}$$

$$K_b = [H_i]^2[O_i^{''}] p_{H_2O}^{-1}. \tag{2-5}$$

The proton concentration is twice that of the oxygen interstitial concentration based on equation (2-4). Equation (2-5) can then be written as

$$[H_i] = (2K_b)^{1/3} p_{H_2O}^{1/3}. \tag{2-5a}$$

Proton concentration should be proportional to $p_{H_2O}^{1/3}$ based on this model. It matched the conductivity behavior better than the first model. However, Norby thought

this model required higher defect concentration than those from Ca or Sr substitution but he did not explain it in detail [27].

Actually, both of the two models have limitations. He did not point out the existing form of protons in the phosphate and proposed the defect structures only with conductivity information. Corresponding structural characterizations should be done to assure his defect model. He considered that oxygen vacancies dominate at high temperature in his first hypothesis. However, it is not absolutely true in the presence of water vapor. The proton conduction sometimes still dominates. There is also a possibility of p-type electronic conduction dominance. His second hypothesis matched his experimental results better but it did not indicate the doping effect on the possible proton concentration in the lattice. If we consider that the second defect structure is right, then the electroneutrality could be

$$p+[H_i^{\cdot}]=2[O_i^{''}]+[M_{La}^{'}]+n\,. \tag{2-6}$$

However, he considered that the proton concentration was twice that of the oxygen interstitial concentration based on equation (2-4). Generally, the oxygen interstitials are not easily incorporated into the lattice due to their large size. Therefore, the amount of protons produced would not be as much as the model suggested.

2.3.2 Amezawa's Hypothesis

Later, Amezawa came up with a better hypothesis than Norby. He sintered a pellet of Sr doped $LaPO_4$ (Sr= 0-7 mol%), ground it into powder and heat treated it at 900 ºC for 10 h in an unspecified atmosphere under two different conditions. One condition is 1 kPa of water vapor and the other is vacuum [42]. He used FT-Raman and MAS-NMR spectroscopy to examine local structures in Sr doped $LaPO_4$. Those results revealed that

hydrogen phosphate ions HPO_4^{2-} and pyrophosphate ions $P_2O_7^{4-}$ existed in Sr doped $LaPO_4$ under these two conditions, respectively, in addition to orthophosphate ions PO_4^{3-}. No pyrophosphate ion $P_2O_7^{4-}$ was detected in the water vapor treated sample by Raman or NMR spectroscopy. The chemical shift assigned to hydrogen phosphate ions HPO_4^{2-} also appeared in the 5 mol% and 7 mol% Sr doped $LaPO_4$ after heat treatment under vacuum. However, their intensities decreased compared with sample after heat treatment under water vapor. He explained the results as decreasing concentration of protons during heat treatment under vacuum, but did not mention the origin of proton in the sample.

He proposed a defect structure model for Sr doped $LaPO_4$ based on the characterization results. According to the model, La substitution with Sr leads to formation of $P_2O_7^{4-}$ as intrinsic positive defects. Protons are introduced into the phosphate forming hydrogen phosphate groups through the equilibrium between $P_2O_7^{4-}$ and water vapor. Figure 2-3 is drawn to approximately illustrate the chemical structure of phosphate, pyrophosphate and hypophosphate. The proton transfer between phosphates is also shown. Mobile protons can transfer to the nearest neighboring tetrahedron or to the next oxygen in the same tetrahedron. The reorientation of the PO_4 tetrahedron facilitates the proton transfer.

The specific relationship between defect species from Amezawa 's paper are reproduced in equations (2-7) to (2-11) below:

$$\frac{1}{2}Sr_2P_2O_7 \rightarrow Sr'_{La} + \frac{1}{2}(P_2O_7)^{\cdot\cdot}_{2PO_4} \tag{2-7}$$

$$\frac{1}{2}(P_2O_7)^{\cdot\cdot}_{2PO_4} + \frac{1}{2}H_2O(g) \rightarrow (HPO_4)^{\cdot}_{PO_4} \tag{2-8}$$

$$K_1 = [(HPO_4)^{\cdot}_{PO_4}][(P_2O_7)^{\cdot\cdot}_{2PO_4}]^{-1/2}P^{-1/2}_{H_2O} \tag{2-9}$$

$$\frac{1}{2}(P_2O_7)^{\cdot}_{2PO_4} + \frac{1}{4}O_2(g) \rightarrow (PO_4)^{x}_{PO_4} + h^{\cdot} \tag{2-10}$$

$$K_2 = p[(P_2O_7)^{\cdot}_{2PO_4}]^{-1/2} p_{O_2}^{-1/4} \tag{2-11}$$

where

$(PO_4)^{x}_{PO_4}$: phosphate on phosphate site

$(P_2O_7)^{\cdot}_{2PO_4}$: oxygen vacancy in double phosphate site

$(HPO_4)_{PO_4}$: interstitial proton in phosphate.

An issue with these formulas is that half oxygen atoms have no physical meaning. Therefore, the formulas were multiplied by a factor of 2 and rewritten as follows:

$$Sr_2P_2O_7 \rightarrow 2Sr'_{La} + (P_2O_7)^{\cdot}_{2PO_4} \tag{2-7a}$$

$$(P_2O_7)^{\cdot}_{2PO_4} + H_2O(g) \rightarrow 2(HPO_4)_{PO_4} \tag{2-8a}$$

$$(P_2O_7)^{\cdot}_{2PO_4} + \frac{1}{2}O_2(g) \rightarrow 2(PO_4)^{x}_{PO_4} + 2h^{\cdot}. \tag{2-10a}$$

The electroneutrality conduction can be written as

$$[(HPO_4)_{PO_4}] + 2[(P_2O_7)^{\cdot}_{2PO_4}] + p = [Sr'_{La}] + n.$$

If $P_2O_7^{4-}$ and HPO_4^{2-} are the dominant positive defects and electronic defects are only present in minor concentration, the electroneutrality conduction can be approximated by

$$[(HPO_4)_{PO_4}] + 2[(P_2O_7)^{\cdot}_{2PO_4}] = [Sr'_{La}] = \text{constant}. \tag{2-12}$$

He mentioned two cases. In the first case, $P_2O_7^{4-}$ is the dominant defect and charge neutrality can be written as

$$2[(P_2O_7)^{\cdot}_{2PO_4}] = [Sr'_{La}]. \tag{2-13}$$

Based on formulas (2-9) and (2-13), the proton concentration can be described as

$$[(HPO_4)_{PO_4}] = K_1([Sr'_{La}]/2)^{1/2} p_{H_2O}^{1/2}. \quad (2\text{-}14)$$

Based on formulas (2-11) and (2-13), the electron hole concentration can be described as

$$p = K_2([Sr'_{La}]/2)^{1/2} p_{O_2}^{1/4}. \quad (2\text{-}15)$$

In this case, proton concentration is supposed to be proportional to $p_{H_2O}^{1/2}$ and p-type electronic concentration is supposed to follow $p_{O_2}^{1/4}$.

In the second case, hydrogen phosphate groups are the dominant defects and charge neutrality can be written as

$$[(HPO_4)_{PO_4}] = [Sr'_{La}]. \quad (2\text{-}16)$$

Based on formulas (2-9) and (2-16), the oxygen vacancy concentration can be described as

$$[(P_2O_7)^{2-}_{2PO_4}] = K_1^{-2}[Sr'_{La}]^2 p_{H_2O}^{-1}. \quad (2\text{-}17)$$

Based on formulas (2-11) and (2-17), the electron hole concentration can be described as

$$p = K_1^{-1}K_2[Sr'_{La}]p_{H_2O}^{-1/2} p_{O_2}^{1/4}. \quad (2\text{-}18)$$

In this case, p-type electronic concentration is supposed to follow $p_{O_2}^{1/4}$. Proton concentration is supposed to be independent of water pressure and oxygen partial pressure.

However, for Sr doped $LaPO_4$, oxygen partial pressure and water partial pressure dependence of conductivity is much smaller than expected. He considered it was caused by the change from hydrogen phosphate dominance to oxygen vacancy (pyrophosphate) dominance.

Amezawa's hypothesis not only pointed out the existing form of hydrogen in phosphates but also pointed out the relationship between defect species based on characterization results. He predicted the oxygen partial pressure and water partial pressure dependence of conductivity using his proposed defect structure. Amezawa's hypothesis, however, addressed only the intermediate and high oxygen partial pressure region, ignoring the low oxygen partial pressure region. He considered oxygen vacancies or protons instead of electron holes dominating in the high oxygen partial pressure region. His NMR and Raman characterization results did not indicate the existence of pyrophosphate $P_2O_7^{4-}$ in the wet atmosphere treated sample. Therefore, the first case did not exist. If we consider the undetected pyrophosphates were due to the limitation of the characterization technology, then the results also could not exclude the possibility of electron holes as the dominant species. The contribution from electron holes at high temperature should not be omitted. In this case, we can consider the electroneutrality condition as

$$p = [Sr'_{La}]. \tag{2-19}$$

The proton and oxygen vacancy concentration could be written as

$$[(HPO_4)_{PO_4}] = K_1 K_2^{-1} [Sr'_{La}] p_{O_2}^{-1/2} p_{H_2O}^{1/2} \tag{2-20}$$

$$[(P_2O_7)_{2PO_4}] = K_2^{-2} [Sr'_{La}]^2 p_{O_2}^{-1/2}. \tag{2-21}$$

This model also can explain the conductivity behavior of Sr doped $LaPO_4$. The electron hole concentration will not increase much with oxygen partial pressure based on Eqs. (2-19), which might explain the conductivity dependence better.

He predicted the conductivity dependence of oxygen partial pressure or water partial pressure based on his proposed model. Actually, the conductivity is not only

related with charge carrier's concentration but also related with carrier's mobility. The proposed model only predicted the concentration dependence of oxygen partial pressure or water partial pressure.

2.3.2 Haile's and Mizuno's Hypothesis

Haile [58] revealed the high temperature phase of $Cs_2(HSO_4)(H_2PO_4)$ is cubic with a CsCl structure by using high temperature X-ray powder diffraction and infrared spectroscopy. Cs atoms are at the corners of a simple cubic unit cell and the XO_4 group (X=P or S) is at the center. As a result, oxygen atoms must be distributed over many sites and oxygen site occupancy is less than one. Accordingly, the PO_4 group must exhibit multiple orientations. The possible rapid PO_4 group reorientation can facilitate proton transfer. Mizuno studied proton dynamics in phase II of $CsHSO_4$ by ^1H NMR between 210 and 470 K [67] and proton diffusion in the superprotonic phase of $CsHSO_4$ (phase I) by ^1H NMR relaxation [68]. The NMR results demonstrate that proton transfer between two neighbouring SO_4 tetrahedra takes place much easier than the reorientation of the SO_4 tetrahedra. Thus, the reorientation limits the rate of the proton transport in phase II and I. The electronic structure and proton transfer mechanism of $CsHSO_4$ phase I were studied by the first-principles methods [69]. The calculated result showed that the band gap is 6.03 eV, indicating that it is electronically insulating. The reorientation of the sulfate tetrahedron can take place very frequently. Sometimes the proton transfers to the nearest neighboring tetrahedron and from there it continues to transfer either to the next oxygen ion or to the next hydrogen bond. Sometimes the proton rotates to a local minimum and from there it continues to transfer to the next nearest neighboring tetrahedron.

2.4 Transference Number in Phosphates

The transference number t_i characterizes the contribution of each charge carrier to the current in a material. There are few instances in the literatures where the proton transference number in phosphates is reported.

Gallini showed for the first time with the EMF measurements of water vapor concentration cells that 2.5 mol% and 5 mol% Sr doped $LaPO_4$ were predominantly proton conductors below 700 °C in wet oxygen [45]. The cell was exposed to wet oxygen while the water vapor partial pressure was different on both sides. The obtained proton transport number was approximately 0.62 at 600 °C. The cell was then exposed to an oxygen partial pressure gradient with dry gas on one side and wet gas on another side. The water partial pressures on both sides were monitored. The obtained total ionic transport number is 0.59 at 600 °C. It was not significantly different from the proton transference number of 0.62. Based on this, Sr doped $LaPO_4$ was considered by Gallini to be a proton conductor.

Amezawa studied proton and native conduction in 5 mol% Sr doped $LaPO_4$ by thermoelectric power measurements [46]. The proton transport number of 5 mol% Sr doped $LaPO_4$ was calculated to be unity in wet air at 600 °C when water pressure was larger than 1 kPa and at 700 °C when water pressure was larger than 3 kPa. He used the same electroneutrality conditions as in the defect structure studies [42], therefore, the obtained proton transference number may be slightly high.

2.5 Hydrogen Permeation in Phosphates

When a material is used as hydrogen separation membrane, it will be exposed to atmospheres in the low oxygen partial pressure region. Its hydrogen permeability is

closely related with its total conductivity and transference number in that oxygen partial pressure region. The material will have a high hydrogen permeation flux if its proton conductivity and electronic conductivities are sufficiently high and nearly equal. Unfortunately, no one mentioned the conductivity behavior and transference number results of phosphates in the low oxygen partial pressure region, especially in hydrogen atmosphere. Thus far, no literature has reported hydrogen permeability of phosphates.

The reported conductivity data and transference number results of phosphates all focused on the wet air or wet oxygen atmosphere. However, the conductivity and transference number changed with oxygen partial pressures. Therefore, the hydrogen permeation in phosphates could not be predicted without information about their total conductivity and proton transference number in hydrogen atmosphere.

2.6 Summary

Conductivity and transference number measurement of doped phosphates indicated that they are proton conductors in wet oxygen or air atmosphere. The conductivities of reported phosphates were still lower than that of perovskite oxide system above 300 °C. No proton conductivity data of phosphates in hydrogen atmosphere was reported. There was also no reported hydrogen permeability of phosphate so far. The best proposed defect structure of phosphate still has limitations and only covered the intermediate and high oxygen partial pressure region. As proton conductors, conductivity behaviors of phosphates and corresponding defect structures should be studied in hydrogen atmosphere.

Based on reviewed literatures, we expected the desired new phosphate was a proton conductor. Its conductivity as functions of temperature, oxygen partial pressure or water partial pressure will be studied and compared with literature. Its corresponding defect

structure will be proposed based on characterization results. More attention will be paid to conductivity behavior and defect structure in the low oxygen partial pressure region, especially hydrogen atmosphere. Proton transference number and hydrogen permeation of the desired phosphate will be measured after finding an appropriate sealant at intermediate temperature range.

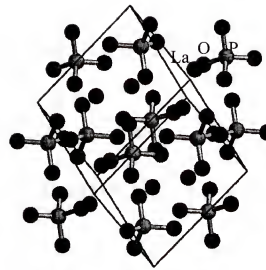

Figure 2-1. The crystal structure of $LaPO_4$ with monazite structure (from ref [43]).

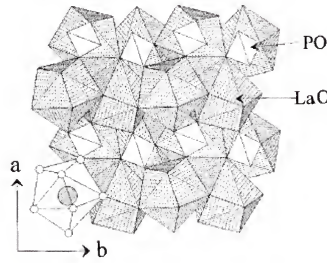

Figure 2-2. Polyhedral diagrams of the monazite structure (from ref [44]).

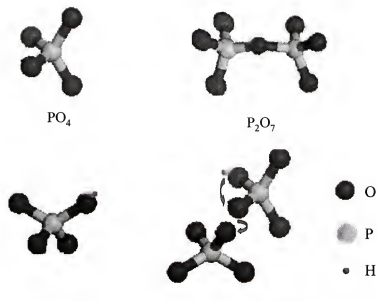

Figure 2-3. Phosphate, diphosphate and hydrogen phosphate structure and proton transfer illustration using "MS modeling" software and photoshop.

CHAPTER 3
PHASE IDENTIFICATION

3.1 Introduction

As stated in the first chapter, the hydrogen flux of composite BCG5Pd was higher than that of BCG35Pd when the temperature was lower than 550ºC. Additionally, this hydrogen flux did not achieve an equilibrium value even after 20 hours at 650 ºC. The second phase Pd did not exhibit such a trend under isothermal conditions. Krishnamurthy in our lab [36] synthesized the composite BCG5Pd powder by electroless deposition, which is a unique process and may introduce some impurity. The impurity may react with composite BCG5Pd to form a tertiary phase at high sintering temperature. The produced tertiary phase may contribute to such an unusual trend. If we could identify this tertiary phase, synthesize it and prove it as a good proton conductor, it will be an important development in fuel cell and hydrogen research field. Therefore, composite BCG5Pd was characterized by X-ray diffraction and infrared spectroscopy. The electroless deposition process of composite BCG5Pd was also repeated and absorbed impurity was measured by an inductively coupled plasma atomic emission spectrometer (ICP-AES). The pH effects on the stability of BCGO in the electroless bath as well as the impurities absorbed were studied.

3.2. Experiment

3.2.1 Electroless Deposition

BCGO powder was synthesized by solid-state reaction and sieved to less than 45 μm. For the electroless deposition at pH= 3, the procedure was performed the same as

Krishnamurthy [36]. For the electroless deposition at pH= 10 [70], 12g BCGO powder was suspended in the electroless solution bath consisting of palladium chloride (1.8 g), ammonium hydroxide (24 mL), ammonium chloride (3.6 g), formaldehyde (37 wt%, 16 mL) and buffer (pH= 10, 80 mL). Sodium hypophosphite (8 g) was added to the bath under rapid stirring. In both pH conditions, the color of the electroless baths changed to black immediately when sodium hypophosphate was added. Color of the bath became shallow green and black particles precipitated to the bottom, which suggested that the bath was exhausted. Powders were then filtered through 3.0 um filter paper and washed with deionized water several times. Then they were dried and calcined at 900, 1100 and 1475 °C in air for 10 h and finally treated at 900 °C in argon for 5 h.

3.2.2 Solid State Reaction

A mixture of BCGO and $NH_4H_2PO_4$ was milled, dried and calcined at 1475 °C for 10 h and argon treated at 900 °C for 5 h. For conductivity measurement, sintered powders were uniaxially pressed at 35 MPa, cold isostatic pressed at 200 MPa, sintered at 1450 °C in air for 10 h and treated at 900 °C in argon for 10 h.

3.2.3 Characterization

The actual concentration of coated Pd and P impurity absorbed under different pH conditions were measured by ICP-AES (Perkin-Elmer Plasma 3200) with a detection limit range of less than 1 part per million. 1 g of electroless deposited powder was dried, accurately weighted, and then transferred into a 500 ml volumetric flask. 10 ml 37% HCl was added to totally dissolve the mixture and then diluted with distilled deionized water.

XRD (PHILIPS-APD-3720) was used to analyze the phase distribution in the powders. IR (INTCOLET Magna 760 Bench spectrometer) was used to investigate the

existence form of the tertiary phase. The measured wave number range was 400-4000 cm^{-1}. The reference was KBr powder.

The conductivity measurement followed Krishnamurthy's procedure [36]. Gold paste was brushed on top of the sintered pellet of the mixture of BCGO and $NH_4H_2PO_4$, dried at 125 °C for 30 min. The sample was then fired at 850 °C for 1 h. The gold pastes acted as electrodes for the sample. Thin gold wires were attached to the gold electrodes to make contact with leads of the analyzer. The conductivity was measured by a Solatron 1260. The atmosphere was wet 10vol% hydrogen, using temperature range of 400-800 °C.

3.3 Results and Discussion

3.3.1 XRD Results

Figure 3-1 shows XRD result of composite BCG5Pd synthesized by Krishnamurthy. It is compared with that of composite BCG35Pd synthesized by solid-state reaction. Peak position of Pd and BCGO is marked. For composite BCG5Pd before sintering, in addition to Pd and BCGO, other peaks also appeared. However, their intensities were so low that they can be considered as machine noise. The intensity of impurity peaks increased after sintering. Impurity peaks at 2θ=33.2° and 56.3° belonged to CeO_2 (200) and (311). The first peak's intensity was 30% relative to the second peak. This could be used as a sure indication that CeO_2 was present in the material under examination [71]. However, determining the presence of other possible products was complicated by the fact that many peaks of possible products overlap each other and their intensities were all low.

In Krishnamurthy's process [36], BCGO powders were suspended in an electroless solution bath (pH=3) consisting of $PdCl_2$ and ammonium hydroxide. Sodium hypophosphite was added to reduce Pd from the solution under rapid stirring. Powders were then filtered and washed. Some ions were not easily washed off and absorbed as impurities on the surface of the composite. However, XRD is not very sensitive to the surface composition change compared with the grain interior even if the surface is well crystallized [72]. Absorbed impurities began to react with the interior of BCGO during sintering and their XRD peak intensity increased. CeO_2 was easily determined in the sintered composite BCG5Pd.

As we know, the basicity of BCGO is advantageous for the formation of proton charge carriers, but makes it unstable in acidic solution, which is used in Krishnamurthy's process [36]. The pH condition also affects the amount of impurities absorbed. Therefore, electroless deposition process of BCG5Pd was repeated at different pH conditions.

ICP-AES analysis results showed that the composite was composed of 6.87 wt% Pd and 2.89 wt% P with deposition at pH= 10 and it was composed of 7.38 wt% Pd (4.31vol%) and 2.32 wt% P with deposition at pH= 3. Pd concentration was less than the theoretical value 9.07 wt%. It indicated that Pd did not deposit completely onto the BCGO particle surface while reduced from the $PdCl_2$ solution. Electroless bath with pH= 3 had a better deposition effect of Pd on BCGO and less phosphorus adsorption. Both of these two electroless bathes decomposed part of BCGO to form CeO_2. This decomposition is more severe in the electroless bath with pH= 3, which is shown in

figure 3-2. From the stability issue of BCGO, it is better to use a basic electroless bath for composite synthesis.

Phosphorus impurity was both absorbed onto BCGO under two pH conditions. It reacted with BCGO to form some tertiary phase at higher sintering temperature. Two samples showed little difference in the absorbed phosphate concentration and the intensity of CeO_2 was a little higher in the composite with 4.31vol%Pd. CeO_2 was an additional unwanted impurity in the composite and made the tertiary phase characterization more difficult. However, the pH condition of the electroless bath is similar between BCG4.31Pd and BCG5Pd. We chose the composite with 4.31vol% Pd (BCG4.31Pd) to do further tertiary phase characterizations because of it's same process with Krishnamurthy's.

Figure 3-3 shows the XRD results of BCG4.31Pd with different sintering temperatures. The main peak of BCGO decreased and some peaks even disappeared after sintering at 900 °C. The intensity of CeO_2 peaks increased with sintering temperature. This suggests that decomposition of BCGO became worse due to the reaction with phosphorus impurity at high temperature. In addition to CeO_2, there are other impurity peaks and their intensities increase with increasing sintering temperature. $Ba_3Ce(PO_4)_3$, $Ba_3(PO_4)_2$ and $CePO_4$ are all possible impurities. As pointed out in chapter 1, the desired tertiary phase might be a good proton conductor. The reported conductivities of $Ba_3(PO_4)_2$ and $CePO_4$ were low [25] and therefore may be just unwanted impurities. $Ba_3Ce(PO_4)_3$ might be the desired tertiary phase. The existence of $Ba_3Ce(PO_4)_3$ could be produced by the solid state reaction of $Ba_3(PO_4)_2$ and $CePO_4$ at high sintering temperature, however, the phase diagram of system $CePO_4$-$Ba_3(PO_4)_2$ was not found.

Figure 3-4 shows the phase diagram of system YPO_4-$Ca_3(PO4)_2$ [73]. Ca_3YPO_4 is produced when the temperature is higher than 1215 °C. $Ba_3Ce(PO_4)_3$, $Ba_3(PO_4)_2$ and $CePO_4$ may co-exist in a similar phase diagram.

Caballero [72] reported that residual phosphorous located at the surface of the particles reacted with $BaTiO_3$ during sintering to form BaO-rich compounds and leave a certain TiO_2 excess. CeO_2 excess and BaO-rich compound $Ba_3Ce(PO_4)_3$ may also be produced by the reaction of BCGO with other phosphorous containing compounds. Therefore, phosphorous was introduced by solid-state reaction of BCGO with $NH_4H_2PO_4$ as the starting material, which avoided the sodium impurity introduced by hypophosphite. Different ratios of BCGO to $NH_4H_2PO_4$ were used to investigate the phosphorous concentration effect on the composition of the product.

In Krishnamurthy's experiment, BCG5Pd was sintered at 1475 °C in air and 900° C in argon after electroless deposition. Argon treatment was used to prevent the formation of PdO [36]. It is unknown whether or not argon atmosphere has an effect on the composition of the tertiary phase. Therefore, the exact sintering atmosphere was followed in solid-state reaction of BCGO with $NH_4H_2PO_4$.

Figure 3-5 shows XRD results of sintered mixture of BCGO and $NH_4H_2PO_4$ with a sintering temperature of 1475 °C and dwell time 10 h. The molar ratios of BCGO and $NH_4H_2PO_4$ are 1:0.1, 1:0.3 and 1:1, respectively. Figure 3-6 shows XRD results of sintered mixture of BCGO and $NH_4H_2PO_4$ with molar ratio of 1:0.1 and 1:1 with or without argon treatment. Compared with XRD result of BCGO, they all contained impurity peaks. There are few differences between XRD results of sintered mixture with or without argon treatment, suggesting the little effect of atmosphere on the product

composition. Products were identified as $Ba_3(PO_4)_2$, $CePO_4$, CeO_2, $Ba_3Ce(PO_4)_3$. The relative intensity of CeO_2 and $Ba_3Ce(PO_4)_3$ increased with initial concentration of $NH_4H_2PO_4$.

All the produced mixtures contained one common composition $Ba_3Ce(PO_4)_3$, which is the most likely the desired tertiary phase. Its crystal structure is cubic with a lattice constant of a= 10.5112 Å according to JCPDS 43-0643.

3.3.2 IR Results

Figure 3-7 (a) shows the infrared spectroscopy of sintered composite BCG5Pd. Figure 3-7 (b) shows the infrared spectroscopy of $SrCe_{1-x}Y_xO_{3-\delta}$ and $SrZr_{1-x}Y_xO_{3-\delta}$ [19]. Table 3-1 lists their band assignment. Perovskites $SrCe_{1-x}Y_xO_{3-\delta}$ and $SrZr_{1-x}Y_xO_{3-\delta}$ have broad OH stretching bands at 3200 cm^{-1}. OH stretching band of composite BCG5Pd is obscured by a strong and broad band at 3430 cm^{-1}, which is attributed to the stretching vibrations of water. The band at 1631 cm^{-1} of composite BCG5Pd is due to the bending vibrations of water molecules. The band at 1035 cm^{-1} of composite BCG5Pd is attributed to the tertiary phase.

$Ba_3Ce(PO_4)_3$, the possible tertiary phase, is an orthophosphate with tetrahedral symmetry (T_d). Tetrahedral symmetric orthophosphate anion has four types of vibrations: symmetric stretching (υ_s), symmetric bending (δ_s), antisymmetric stretching (υ_{as}) and antisymmetric bending (δ_{as}). They are illustrated in figure 3-8. Symmetric stretching and symmetric bending are IR inactive. IR spectrum of a tetrahedral symmetric orthophosphate has a strong stretching mode at around 1000 and a strong bending mode at 500-600 cm^{-1}. However, the vibrations of molecules fixed in the lattice are not only

affected by their symmetry but also by the lattice symmetry, which may shift the band position. The band at 1035 cm^{-1} of composite BCG5Pd is attributed to asymmetric stretching of PO_2 group. Asymmetric bending of PO_2 group is observed at 456 cm^{-1}.

Figure 3-8 (a) and (b) compares IR of composite BCG5Pd with the high temperature IR of $Cs_2(HSO_4)(H_2PO_4)$, which was reported to have a cubic structure at high temperature [58]. Figure 3-8 (c) illustrates the difference between the orthophosphates, diphosphates and hydrogen phosphates. Diphosphates are characterized by the POP bridge vibrations with a strong asymmetric stretching mode around 900-950 cm^{-1} in IR spectrum. There is no POP vibration observed in the composite BCG5Pd, suggesting no diphosphate in the tertiary phase. Hydrogen phosphates are characterized by the POH vibrations. Table 3-2 lists the wave number of OH vibrations of $Cs_2(HSO_4)(H_2PO_4)$ at 199°C, which are at 1715, 2350 and 2945 cm^{-1}. These OH vibrations are not observed in the composite BCG5Pd, suggesting no H_2PO_4 group in the tertiary phase.

Figure 3-9 shows the IR spectra of the sintered mixture of BCGO and $NH_4H_2PO_4$ with ratio 1:1 compared with those of composite BCG4.31Pd and BCG5Pd. Table 3-3 lists their band assignments. The stretching vibration mode is degenerated in the composite BCG5Pd but split in the composite BCG4.31Pd. The stretching vibration modes of BCG4.31Pd are observed at 1060 and 1000 cm^{-1} while that of the sintered mixture is observed at 1032 cm^{-1}. The bending vibration mode is degenerated in the composite BCG5Pd but split in the sintered mixture. The bending vibration modes of the sintered mixture are observed at 546 and 407 cm^{-1} while that of composite BCG4.31Pd is observed at 559 cm^{-1}. However, POP bridge vibrations are observed at 935 cm^{-1} in

composite BCG4.31Pd and at 897 cm^{-1} in the sintered mixture. This shows that small amount of diphosphates were produced in the composite BCG4.31Pd and sintered mixture.

3.3.3 Conductivity Measurement

Conductivity of the sintered mixture of BCGO and $NH_4H_2PO_4$ was measured to investigate the effect of the desired phase $Ba_3Ce(PO_4)_3$ on the total conductivity. Figure 3-10 shows the impedance plot of the sintered mixture of BCGO and $NH_4H_2PO_4$ at 800 °C in wet 10vol% hydrogen atmosphere.

In a typical impedance plot of a ceramic system, the semicircles belong to the electrode, grain boundary, and bulk, from low frequency to high frequency. The corresponding equivalent circuit is composed of resistors and capacitors in an ideal system. In the system of the sintered mixture of BCGO and $NH_4H_2PO_4$, there are many produced impurities. It is difficult to use a simple electrical circuit to simulate the involved physical transport. However, information about the bulk conductivity is clearly demonstrated by semicircle I. The bulk electrical resistance values were obtained from the low frequency interception of the semicircle I on the real axis of the impedance plot in figure 3-10 (a). Semicircle II is more complex, including electrode effect and other contribution. The information about the tertiary phase resistance was found to be impossible to obtain from this impedance plot.

Figure 3-11 is the Arrhenius plot of the sintered mixture of BCGO and $NH_4H_2PO_4$. The diameter of the sample was 25.92 mm and thickness was 3.344 mm. The relative density was 87%. The temperature range was 400-800 °C. The bulk conductivity was on the order of 10^{-6} S/cm at 500-800 °C, which is less than that of BCGO with the order of

10^{-2} S/cm (shown in figure 1-1). The sintered mixture did not have as good a conductivity as expected. This may be caused by the additional unwanted impurity phases such as CeO_2, $Ba_3(PO_4)_2$ and $CePO_4$. The conductivity of our desired phase $Ba_3Ce(PO_4)_3$ was not clearly demonstrated in this measurement. Single phase $Ba_3Ce(PO_4)_3$ should be synthesized and electrochemically characterized.

3.4 Conclusion

In electroless deposition, exposure to an acidic bath decomposed part of BCGO to form CeO_2 and phosphorus impurity was absorbed and covered the surface of BCGO particles. They reacted at high sintering temperature to form a BaO-rich compound $Ba_3Ce(PO_4)_3$ and leave a certain CeO_2 excess. $Ba_3Ce(PO_4)_3$ was most likely the desired tertiary phase in the composite BCG5Pd.

Solid-state reaction between BCGO and $NH_4H_2PO_4$ produced $Ba_3Ce(PO_4)_3$ and CeO_2, which increased with increasing amount of $NH_4H_2PO_4$. The conductivity of the desired phase $Ba_3Ce(PO_4)_3$ was not clearly demonstrated in the conductivity results of the sintered mixture. Single phase $Ba_3Ce(PO_4)_3$ will be synthesized and electrochemically characterized in the following chapter.

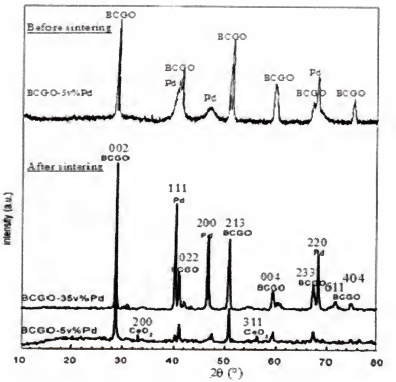

Figure 3-1. XRD patterns of composite BCG5Pd and BCG35Pd.

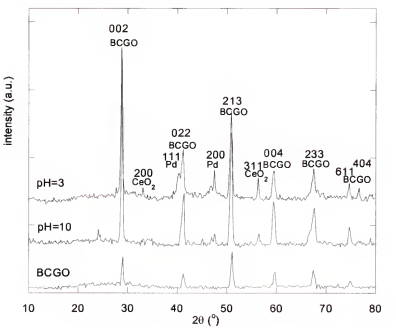

Figure 3-2. XRD results of deposited composites at different pH conditions.

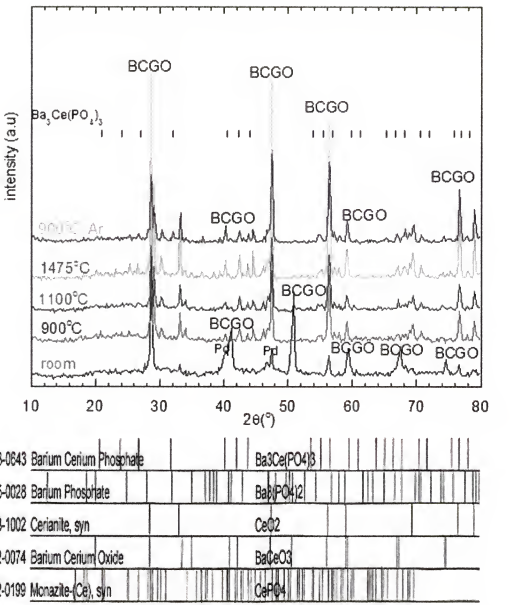

Figure 3-3. XRD results of composite BCG4.31Pd with different sintering temperature compared with JCPDS 43-0643, 25-0028, 43-1002, 22-0074 and 32-0199.

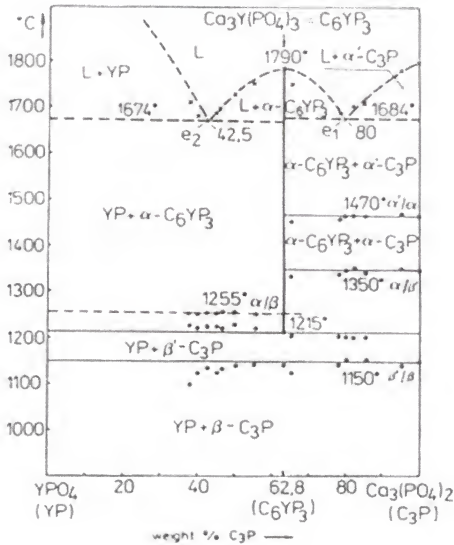

Figure 3-4. Phase diagram of system YPO_4-$Ca_3(PO_4)_2$ (from ref [73]).

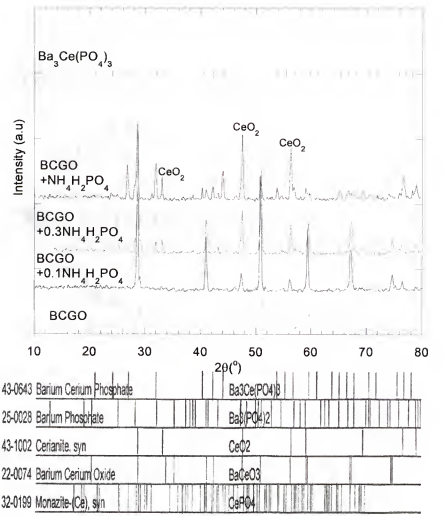

Figure 3-5. XRD results of sintered mixtures of BCGO and $NH_4H_2PO_4$ with different $NH_4H_2PO_4$ concentration.

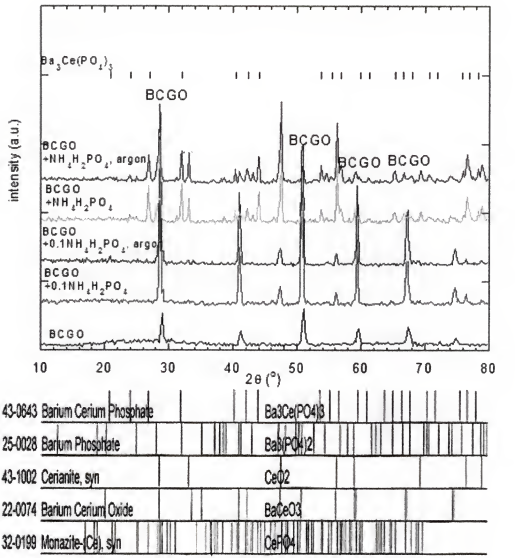

Figure 3-6. XRD results of mixtures of BCGO and $NH_4H_2PO_4$ with or without argon treatment.

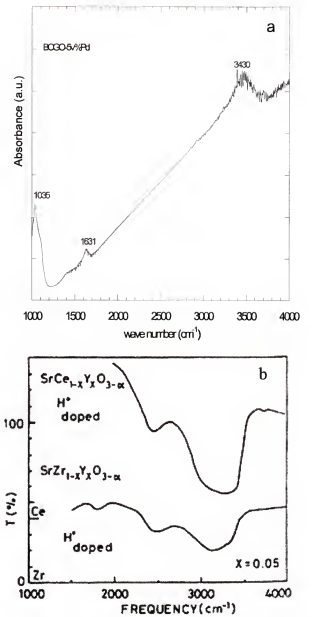

Figure 3-7. IR spectra of composite BCG5Pd, $SrCe_{1-x}Y_xO_{3-\delta}$ and $SrZr_{1-x}Y_xO_{3-\delta}$. (a) BCG5Pd and (b) $SrCe_{1-x}Y_xO_{3-\delta}$ and $SrZr_{1-x}Y_xO_{3-\delta}$ (from ref [19]).

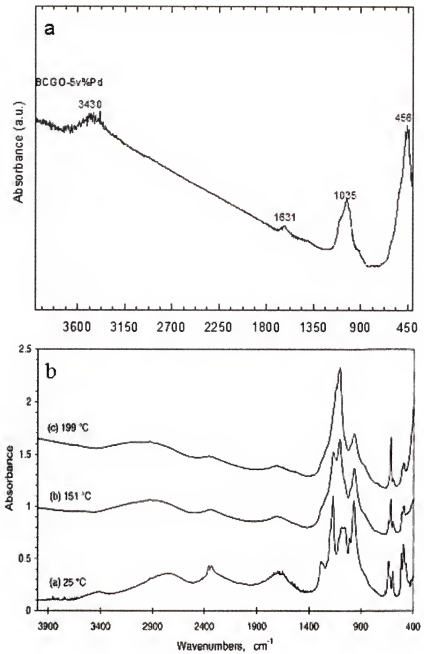
a
BCGO-5v%Pd
3430
1631
1035
456
Absorbance (a.u.)
3600
3150
2700
2250
1800
1350
900
450
b
(c) 199 °C
(b) 151 °C
(a) 25 °C
Absorbance
2.5
2
1.5
1
0.5
0
3900
3400
2900
2400
1900
1400
900
400
Wavenumbers, cm-1

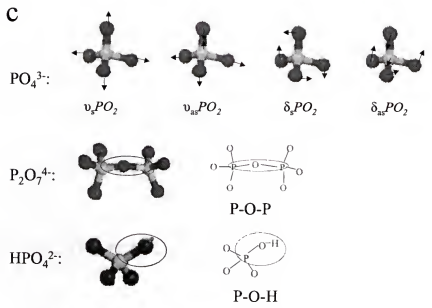

Figure 3-8. IR spectra of composite BCG5Pd and $Cs_2(HSO_4)(H_2PO_4)$. (a) IR spectra of BCG5Pd, (b) IR spectra of $Cs_2(HSO_4)(H_2PO_4)$ with a cubic structure at 199 °C [58], and (c) vibration illustration of orthophosphate, diphosphate and hydrogen phosphate.

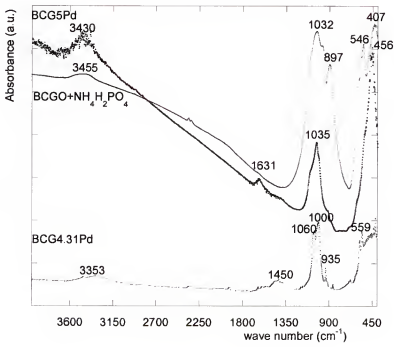

Figure 3-9. IR spectra of the sintered mixture of BCGO and $NH_4H_2PO_4$ compared with those of composite BCG5Pd and BCG4.31Pd.

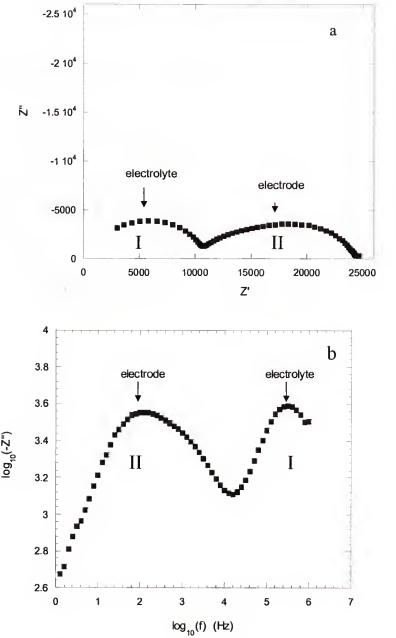

Figure 3-10. Impedance plot of the sintered mixture of BCGO and $NH_4H_2PO_4$ at 800 °C in wet 10% hydrogen atmosphere: (a) imaginary vs. real impedance (b) imaginary impedance vs. frequency.

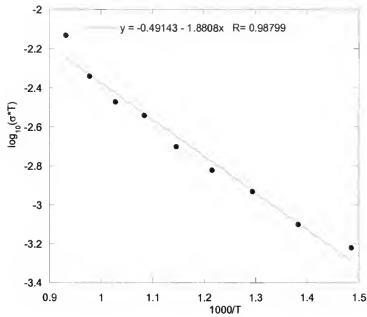

Figure 3-11. Arrhenius plot of the mixture of BCGO and $NH_4H_2PO_4$ in wet 10% hydrogen.

Table 3-1 Band assignment of $SrCe_{1-x}Y_xO_{3-\delta}$, $SrZr_{1-x}Y_xO_{3-\delta}$, and BCG5Pd.

	Wave number (cm^{-1})	assignment
$SrCe_{1-x}Y_xO_{3-\delta}$ $SrZr_{1-x}Y_xO_{3-\delta}$ [19]	3200	υOH
BCG5Pd	3430	υH_2O
	1631	δH_2O
	1035	$\upsilon_{as} PO_2$
	456	δPO_2

υ = stretching, δ = bending.

Table 3-2 Band assignment for $Cs_2(HSO_4)(H_2PO_4)$.

Wave number (cm^{-1})		Qualitative assignment	Parent mode in T_d symmetry
High T	Room T		
495 513	474 496 517	Bending modes	υ_2 (E) OXO-asymmetric bend (IR inactive)
599 620	601 623 641 670		υ_4 (F_2) OXO-symmetric bend
968	971		υ_1 (A_1) XO-symmetric strech (IR inactive)
	1012	X-OH stretch	
1109 1124 1147	1065 1091 1173 1286	X-O strech	υ_3 (F_2) XO-asymmetric stretch
		X-O-H in plane bending mode	
1715	1700	υ OH(C)	
2350	2340	υ OH(B)	
2945	2760	υ OH(A)	

Data from ref [58].

Table 3-3 Band assignment for BCG4.31Pd and sintered mixture of BCGO+$NH_4H_2PO_4$.

	Wave number (cm^{-1})	assignment
BCG4.31Pd	3353	υH_2O
	1060 1000	$\upsilon_{as} PO_2$
	935	υPOP
	559	δPO_2
Sintered mixture of BCGO+$NH_4H_2PO_4$	3455	υH_2O
	1032	$\upsilon_{as} PO_2$
	897	υPOP
	546 407	δPO_2

CHAPTER 4
SYNTHESIS AND CHARACTERIZATION OF $Ba_3Ce(PO_4)_3$

4.1 Introduction

As mentioned in previous chapters, $Ba_3Ce(PO_4)_3$ was most likely the tertiary phase we obtained. The main objective of this chapter is to describe the synthesis and characterization of single-phase $Ba_3Ce(PO_4)_3$. According to JCPDS 43-0643, $Ba_3Ce(PO_4)_3$ belongs to cubic system with space group $I\bar{4}3d$ (220) and lattice parameter a=10.5112 Å. It can be obtained by annealing a stoichiometric mixture of $BaCeO_3$, CeO_2 and $NH_4H_2PO_4$ at 1000 °C for one day and at 1350 °C for 10 days in an open Pt crucible and then quenching in air; however, this process is not efficient. Since the solubility products of $Ba_3(PO_4)_2$ and $CePO_4$ are similar (3.2×10^{-23} and 1×10^{-23}, respectively [74]), the co-precipitation method was attempted. XRD and IR spectroscopy were used to characterize the precipitates with different calcination temperatures. XRD patterns were compared with that of JCPDS 43-0643 to assure a single-phase material was obtained. Software "MS modeling" and "CaRIne Crystallography V3.1" were used to illustrate the crystal structure of $Ba_3Ce(PO_4)_3$. Raman and nuclear magnetic resonance (NMR) spectroscopy were used to investigate the local structures of $Ba_3Ce(PO_4)_3$ under different atmospheres.

As mentioned in chapter 2, defect structures of doped phosphates were proposed to explain their conductivity behavior. They have limitations and only apply in the

intermediate and high oxygen partial pressure regions. Nobody has studied the defect structure in the low oxygen partial pressure region, especially in hydrogen atmosphere. However, that pressure region is very important for proton conductors. In this chapter, the defect structure of $Ba_3Ce(PO_4)_3$ is proposed based on the characterization results. The concentration dependence of charge carriers on the oxygen, hydrogen or water partial pressure was predicted according to the defect structure.

The chemical stability of a hydrogen separation membrane material should be good in the atmosphere of its intended application. Therefore, chemical stability of $Ba_3Ce(PO_4)_3$ in dry helium was tested by high temperature XRD (HT-XRD). XRD patterns of $Ba_3Ce(PO_4)_3$ after separate treatments in hydrogen and air were compared. Finally, thermal expansion behaviors of $Ba_3Ce(PO_4)_3$ in air and hydrogen atmospheres were investigated with a dilatometer.

4.2 Experiment

4.2.1 Synthesis

A solution of $Ba(NO_3)_2$ and $Ce(NO_3)_3{\cdot}6H_2O$ was mixed with an appropriate 3:1 molar ratio. The mixture was stirred and $(NH_4)_2HPO_4$ was added drop by drop into the mixture until it was excess. The pH was controlled to be certain Ba^{2+} and Ce^{3+} were precipitated in the form of $Ba_3(PO_4)_2$ and $CePO_4$. The dried precipitates were calcined at different temperatures with a 3 °C/min heating rate and 4 h dwell time.

4.2.2 Characterization

The precipitates with different calcination temperatures were characterized by XRD on a PHILIPS-APD-3720 using CuKα radiation and by IR on a INTCOLET Magna 760 Bench spectrometer. XRD patterns were compared with that of JCPDS 43-0643. The

synthesized particles of $Ba_3Ce(PO_4)_3$ were suspended in acetone and a drop of the ultrasonicated suspension was transferred to a carbon coated copper microgrid for TEM characterization. Bright field images and selected area diffraction patterns of particles were taken on a JEOL200CX. EMS online software [75] was used to index diffraction patterns.

$Ba_3Ce(PO_4)_3$ powder was pressed into pellets, cold isostatic pressed at 200 MPa and sintered at 1200 °C for 8 h. Pellets were ground into powder and separately treated in different atmospheres (wet and dry air, nitrogen and hydrogen) at 550 °C for 24 h. Raman spectra of treated samples were measured using a Nicolet MAGNA760 spectrometer equipped with a multi-channel CCD detector.

For NMR experiments, typical experimental parameters were as follows: a proton pulse duration of 10.0 μs; a recycle delay of 100 s and a spectral width of 60 Hz. Approximately 40-60 mg of sample were used and 1024 transients were required. All ^1H magic angle spinning NMR spectra in this work were acquired on a Bruker Avance Spectrospin 400 MHz spectrometer operating at a frequency of 400.13 MHz using a triple resonance probe with a 4.0 mm rotor. Spectra were acquired at a spinning rate of 7 kHz to ensure all rotational sidebands would fall outside of the spectral region of interest. All ^1H NMR spectra were referenced to tetramethylsilane (TMS). High-resolution ^{31}P NMR was not applied due to the low concentration of phosphorus (10^{-19} /g) in the $Ba_3Ce(PO_4)_3$.

High temperature XRD was performed on the $Ba_3Ce(PO_4)_3$ powders in the dry helium. $Ba_3Ce(PO_4)_3$ powders were separately treated in hydrogen, argon and air atmosphere at 600 °C for 10 h to study its stability by XRD.

A $Ba_3Ce(PO_4)_3$ pellet was sintered at 1200 °C for 8 h, polished to a 15 mm length and put into a Theta dilatometer to investigate its thermal expansion behavior. The heating and cooling rates were set at 2 °C/min. The gas flow rate was adjusted to maintain 20 kPa over-pressure in the chamber.

4.3 Results and Discussion

4.3.1 Synthesis

Figure 4-1 shows XRD patterns of precipitates with different calcination temperatures. All the heating rates and dwell times were 3 °C/min and 4 h, respectively. The precipitate at room temperature is a mixture of $Ba_3(PO_4)_2$ and $CePO_4$. Peaks at 2θ = 28°, 38.5 and 43° belong to both $Ba_3(PO_4)_2$ and $CePO_4$. The intensity of these peaks decreases with increasing calcination temperature and peaks disappear with an 1100 °C calcination temperature. A new peak appears at 2θ = 27° with a calcination temperature of 800 °C and it becomes strongest with calcinations temperature 1100 °C. The XRD pattern of the 1100 °C calcined sample successfully matches JCPDS 43-0643 (shown in table 4-1) except a d spacing of 1.9128 Å. However, d spacing of 1.9128 can be still be indexed as (521), as shown in figure 4-1. No second phase is detected. The difference between the experimentally obtained d spacings and those in JCPDS 43-0643 is small. This difference may be caused by a different synthesis method.

Figure 4-2 shows the calculated XRD profile of $Ba_3Ce(PO_4)_3$ using the crystallographic data, lattice parameter and CaRIne Crystallography V3.1 software. The calculated XRD files predict all of the d spacings in our experimental XRD result. It includes reflection (521) at 2θ= 47.5°, which is not in the JCPDS 43-0643 but appears in

our experimental XRD data. It suggests single-phase $Ba_3Ce(PO_4)_3$ is produced during calcination at 1100 °C.

Infrared spectra of precipitates with different calcination temperatures are shown in Figure 4-3. Table 4-2 gives assignments of bands with different calcination temperatures. The bands at 1050 and 566 cm^{-1} of $Ba_3Ce(PO_4)_3$ belong to a stretching mode and bending mode of PO_4^{3-}, respectively. The band at 2000 cm^{-1} may originate from the vibration mode of bonds M-O(P) (M= Ba, Ce). The band of stretching vibration at 1100 ºC is broad, which can be narrowed by measuring IR at lower temperature. It may obscure the possible splitting. The bending vibration modes of PO_4^{3-} become degenerated with increasing calcination temperatures. Compared with BCG5Pd in figure 4-4, the stretching and bending vibration modes of synthesized $Ba_3Ce(PO_4)_3$ move to slightly higher wave number. However, it still suggests that a similar chemical environment of the tertiary phase and our synthesized $Ba_3Ce(PO_4)_3$.

4.3.2 Particle Size Characterization

Figure 4-5 (a) is a bright field image of $Ba_3Ce(PO_4)_3$ particles, which revealed a homogeneous and well-crystallized $Ba_3Ce(PO_4)_3$ with a grain size around several hundred nanometers. Figure 4-5 (b) is a selected area diffraction pattern of $Ba_3Ce(PO_4)_3$ with incidence $[\bar{1}3\bar{9}]$. TEM image simulation software was used to obtain corresponding d-spacings, which are listed in table 4-1. They match those obtained by XRD.

4.3.3 Crystal Structure Characterization

According to JCPDS 43-0643, $Ba_3Ce(PO_4)_3$ belongs to cubic system with space group $I\bar{4}3d$ (220) with lattice parameter a=10.5112 Å. According to Wyckoff positions

of group 220, the P atoms are fixed at 12a sites, the Ba and Ce atoms are randomly distributed on the 16c sites, and the O atoms are at 48e sites. Without neutron diffraction experiments, the crystal structures of $Ba_3Ce(PO_4)_3$ can only be approximately illustrated based on the available information of the $Ba_3La(PO_4)_3$ [76], which has a similar crystal structure with $Ba_3Ce(PO_4)_3$. The coordinates of atoms in $Ba_3Ce(PO_4)_3$ are based on those of $Ba_3La(PO_4)_3$. Software "MS modeling" and "CaRIne Crystallography V3.1" are used to illustrate the crystal structure of $Ba_3Ce(PO_4)_3$. The results are shown in figure 4-6 and 4-7, respectively.

The O atoms have two sets of different crystallographic positions in the eulytite-type $Ba_3Ce(PO_4)_3$. However, software "MS modeling" could not plot the two positions at the same time. Only the first set of oxygen sites is considered when using the 'MS modeling". The coordinates of P, O and metals M (M= Ba, Ce) in $Ba_3Ce(PO_4)_3$ are (0.375, 0, 0.25), (0.466317, 0.361411, 0.707516), and (0.06025, 0.06025, 0.06025), respectively, based on that of $Ba_3La(PO_4)_3$ [76]. The bond lengths and angles are measured from the illustrated structure. The measured bond lengths of M-O and P-O in $Ba_3Ce(PO_4)_3$ are 2.818 and 1.427 Å, respectively. The angle of O-P-O is 104.88°. The [111] directional view clearly shows the metal atoms are in the three-fold axis.

Figure 4-7 (a) shows the crystal structure of $Ba_3Ce(PO_4)_3$ using "CaRIne Crystallography V3.1" software. Ba atom is represented by blue sphere. Ce atom is represented by blue sphere with red in the center. The positions of Ba and Ce are random but their molar ratio of 3 is fixed. The two different crystallographic positions for the O-atoms, O1 and O2, are represented by dark and shallow green spheres. Figure 4-7 (b)

gives [001] directional views of $Ba_3La(PO_4)_3$, clearly showing the two sets of oxygen sites [76]. The two possible positions of oxygen atoms cause rotational disorder. The rotational disorder usually changes the coordination of the metal atoms from 6 to 9. $Ba_3Ce(PO_4)_3$ belongs to the same eulytite structure and a rotational disorder of the phosphate group is also expected as $Ba_3La(PO_4)_3$. Neutron diffraction data are needed for further discussion.

Figure 4-8 (a) and (b) gives [010] and [111] directional views of $Ba_3Ce(PO_4)_3$, respectively, with all the oxygen atoms in the same crystallographic position O2. There is a three-fold channel, which may be good for the proton transfer.

As mentioned in the beginning, these illustrated crystal structures of $Ba_3Ce(PO_4)_3$ are based on the available information of the $Ba_3La(PO_4)_3$. Therefore, all the obtained information is just approximation for the real structure. Neutron diffraction experiments would be desirable and extremely useful in a better understanding of the crystal structure.

4.3.4 Defect Structure Characterization

4.3.4.1 Raman characterization

Raman spectroscopy was used to study the proton incorporation and oxygen vacancy formation in $Ba_3Ce(PO_4)_3$ under dry or wet atmospheres.

Raman Characterization of Dry Atmosphere Treated Samples

Figure 4-9 shows the Raman spectra of $Ba_3Ce(PO_4)_3$ after separate treatments with dry air, nitrogen and hydrogen. Raman shifts of $Ba_3Ce(PO_4)_3$ are listed in table 4-3 and compared with Sr doped $LaPO_4$ after dry atmosphere treatments [42].

PO_4^{3-} is the main existing form in $Ba_3Ce(PO_4)_3$ under dry conditions. It has four vibration bands: an asymmetric PO_2 stretching mode at 1057 and 1020 cm^{-1}, a symmetric stretching mode at 944 cm^{-1}, the O-P-O F_2-bending mode at 571 cm^{-1} and the O-P-O E-bending mode at 463 and 439 cm^{-1}. The PO_4^{3-} Raman shift in $Ba_3Ce(PO_4)_3$ is slightly different from that in Sr doped $LaPO_4$, which is due to different cations in the lattice [40].

Raman shifts at 1057 and 1020 cm^{-1} in the dry hydrogen treated $Ba_3Ce(PO_4)_3$ can also be assigned to $P_2O_7^{4-}$ according to reference [41]. Their relative intensities are highest in dry hydrogen treated sample and lowest in dry air treated one, which is shown in figure 4-9 (b). It may suggest that the oxygen vacancy concentration increases with reduced oxygen partial pressure under the dry condition.

For the dry hydrogen treated $Ba_3Ce(PO_4)_3$, proton incorporation is expected. However, Raman did not detect any HPO_4^{2-} shift, which is reported to be strong at the 2500-2150 and 1150-1000 cm^{-1} regions [41].

Raman Characterization of Wet Atmosphere Treated Samples

Raman was also used to investigate the proton incorporation in the presence of water vapor. Vibration bands in the regions of 1240-1460 and 2330-2900cm^{-1} are reported as the existence of POH bonds in reference [77]. Vibration bands at 2176-2787 and 1278-1332cm^{-1} are reported in reference [78] as the stretching and bending modes of POH in acid pyrophosphate $KMg_{0.5}H_2P_2O_7 \cdot H_2O$, respectively.

Figure 4-10 (a, b) is Raman spectra of $Ba_3Ce(PO_4)_3$ after separate treatments in wet and dry nitrogen. Table 4-4 lists Raman shifts of $Ba_3Ce(PO_4)_3$ compared with Sr doped $LaPO_4$ treated in the wet atmosphere [42]. Some liquid water was added into

powder $Ba_3Ce(PO_4)_3$ to show the stretching mode of absorbed water, which appeared at 3333 cm^{-1}. This stretching mode of water molecule did not appear in the wet nitrogen treated $Ba_3Ce(PO_4)_3$, suggesting that no water molecules are inserted in the lattice. The bands at 2881 and 2848 cm^{-1} are assigned to the stretching modes of POH in the HPO_4 group. The bands at 1439, 1295 and 1131 cm^{-1} are assigned to the bending modes of POH. They suggest that protons exist in the form of $(HPO_4)_{PO_4}$ in the wet nitrogen treated $Ba_3Ce(PO_4)_3$.

Raman results also provide some information about oxygen vacancy concentration in the presence of water vapor. Figure 4-10 (c) demonstrates that the relative intensities of $P_2O_7^{4-}$ vibration modes at 1057 and 1020 cm^{-1} decreased in wet nitrogen. This indicates that water partial pressure suppresses the oxygen vacancy formation.

Figure 4-11 is the Raman spectra of $Ba_3Ce(PO_4)_3$ with wet hydrogen treatment. The broad band at 1350 cm^{-1} is assigned to the bending mode of POH bonds according to references [78, 79]. Its relative intensity decreases after drying at 100 °C for 1 h, suggesting the proton concentration decreases with drying process. It is very difficult to compare the relative intensity of vibration bands at 1057 and 1020 cm^{-1} due to the overlap effect with band at 1350 cm^{-1}. Therefore, it is unclear about the water vapor effect on the oxygen vacancy concentration in hydrogen treated $Ba_3Ce(PO_4)_3$.

Raman Characterization Summary

Raman results explain the proton incorporation in the presence of water vapor. Without free hydrogen gas, in the presence of water vapor, bound hydrogen is produced

and oxidized forming protons. The formed protons attach onto the O atoms of PO_4 group and are incorporated into the lattice.

The band wave numbers of incorporated protons under wet atmospheres can be summarized as follows: 2881, 2848, 1439,1295,1135 cm^{-1} in wet nitrogen, 1350 cm^{-1} in wet hydrogen. The wave number reflects the bond strength. Thus, the bond strength of POH decreased with decreasing oxygen partial pressure under wet condition.

Oxygen vacancy concentration increases with reduced oxygen partial pressure under the dry condition. Water vapor suppresses the oxygen vacancy formation in nitrogen. The water vapor effect on the oxygen vacancy concentration in hydrogen is not clearly demonstrated by Raman results.

Unfortunately, Raman results did not demonstrate the existence of protons in the dry hydrogen treated $Ba_3Ce(PO_4)_3$.

4.3.4.2 NMR characterization

According to reference [42], in Sr doped $LaPO_4$, chemical shifts at 5.4 and 1.2 ppm in high-resolution ^1H NMR were considered due to adsorbed water molecules. The chemical shift at 12.4 ppm was considered due to dissolved protons and it had a slower relaxation time than that at 5.4 and 1.2 ppm, reflecting that the dipole interaction between protons was much weaker than that between protons in adsorbed water molecules.

Figure 4-12 is ^1H NMR results of $Ba_3Ce(PO_4)_3$ after different atmosphere treatments. Corresponding chemical shifts of ^1H NMR are listed in table 4-5 and compared with Sr doped $LaPO_4$. Dry air treated $Ba_3Ce(PO_4)_3$ has a chemical shift at 5 ppm, which is assigned to the attached water molecules from the environment. In addition to 5 ppm, the chemical shift at 15 ppm appears in the dry hydrogen treated

$Ba_3Ce(PO_4)_3$. The relative intensity of the chemical shift at 15 ppm is much larger than at 5 ppm. This clearly demonstrates proton insertion under the dry hydrogen condition despite the fact that it is not observed in the Raman spectra. The inserted protons can be expressed in the form of $(HPO_4)_{PO4}$ [42]. The difference between the chemical shift at 15 ppm in $Ba_3Ce(PO_4)_3$ and 12.4 ppm in Sr doped $LaPO_4$ is caused by the different chemical environment.

The ^1H NMR chemical shift at 15 ppm in wet nitrogen treated $Ba_3Ce(PO_4)_3$, shown in figure 4-12, suggests again the proton insertion in the presence of water vapor.

Raman spectra did not indicate whether or not oxygen vacancy existed in the lattice under the wet hydrogen atmosphere. ^{31}P NMR can illustrate it more clearly. The chemical shift of orthophosphate is –4.4, pyrophosphate is -7.2 and –8.4, and hydrogen phosphate is -30.6 ppm according to reference [42]. It would have been very helpful if the ^{31}P NMR was applied. However, it was not applied due to the low concentration of phosphorus (10^{-19} /g) in the $Ba_3Ce(PO_4)_3$.

4.3.4.3 Defect structure

Based on the local structure characterization results, a defect structure model of $Ba_3Ce(PO_4)_3$ was proposed in low ($p_{O_2} < 10^{-15} atm$), low-intermediate ($10^{-15} < p_{O_2} < 10^{-7} atm$), intermediate ($10^{-7} < p_{O_2} < 10^{-1} atm$) and high ($p_{O_2} > 10^{-1} atm$) oxygen partial pressure regions. Defect concentration dependencies of P_{O_2}, P_{H_2} and P_{H_2O} were derived and listed in table 4-6.

Low Oxygen Partial Pressure Region

Oxygen vacancy exists in the phosphate lattice at the low oxygen partial pressure region and plays a similar role as that in perovskites. However, it exists as a different

form in phosphates. Oxygen vacancy in phosphates can be considered as two PO_4 sites sharing two P and seven O atoms. It also can be considered as two PO_4 sites losing one O atom. Oxygen vacancy is expressed as $(P_2O_7)^{\cdot\cdot}_{2PO_4}$ in this work, the same way Amezawa did in his paper [42].

The following defect equilibrium always exists at the low oxygen partial pressure region:

$$2(PO_4)^{x}_{PO_4} \rightarrow (P_2O_7)^{\cdot\cdot}_{2PO_4} + 2e^{'} + \frac{1}{2}O_2 . \qquad \text{K1} \qquad (4\text{-}1)$$

$$K_1 = [(P_2O_7)^{\cdot\cdot}_{2PO_4}]n^2 p_{O_2}^{\frac{1}{2}} .$$

The internal electron-hole pair formation follows the reaction:

$$null = e^{'} + h^{\cdot} . \qquad \text{K2} \qquad (4\text{-}2)$$

At the low oxygen partial pressure region, hole concentration is negligible and its contribution to electroneutrality can be omitted.

Four cases were discussed in the low oxygen partial pressure region. Case 1 is the low water partial pressure condition without free hydrogen, case 2 is the low water partial pressure condition with free hydrogen, case 3 is the high water partial pressure condition without free hydrogen, and case 4 is the high water partial pressure condition with free hydrogen.

Case 1: low water partial pressure without free hydrogen.

Under low water partial pressure condition without free hydrogen, there is no proton source for $Ba_3Ce(PO_4)_3$. Oxygen vacancies are the only significant positive defects to charge balance electrons. The electroneutrality condition is simplified as

$$2[(P_2O_7)^{\cdot\cdot}_{2PO_4}] = n .$$

Therefore,

$$K_1=[n/2]n^2 p_{O_2}^{\frac{1}{2}}.$$

Electron concentration and oxygen vacancy concentration are proportional to $p_{o_2}^{-\frac{1}{6}}$.

There is no water partial pressure dependence due to the low water partial pressure condition. Without a proton source, there is also no hydrogen partial pressure dependence.

Case 2: low water partial pressure with free hydrogen.

Free hydrogen is the only proton source in case 2. Free hydrogen can be oxidized forming protons, which are attached onto the O atoms in the PO_4 tetrahedron and incorporated into the lattice. The corresponding defect equilibrium is written as

$$(PO_4)_{PO_4}^x + \frac{1}{2}H_2 \rightarrow (HPO_4)_{PO_4} + e' \qquad \text{K3} \qquad (4\text{-}3)$$

$$K_3 = n[(HPO_4)_{PO_4}]p_{H_2}^{-\frac{1}{2}}.$$

A small amount of water vapor possibly exists due to the existence of hydrogen and oxygen formed in formula (4-1):

$$H_2 + \frac{1}{2}O_2 \rightarrow H_2O \qquad \text{K4} \qquad (4\text{-}4)$$

$$K_4 = p_{H_2O} p_{H_2}^{-1} p_{O_2}^{-\frac{1}{2}}.$$

Dry hydrogen belongs to low water partial pressure condition with free hydrogen. For dry hydrogen treated $Ba_3Ce(PO_4)_3$, a chemical shift at 15 ppm in ^{1}H NMR spectroscopy result (shown in figure 4-12) clearly demonstrates proton incorporation. Figure 4-9 (b) demonstrates that the oxygen vacancy concentration increases with

reduced oxygen partial pressure under dry condition. Therefore, oxygen vacancies and incorporated protons are the positive defects in the lattice. The electroneutrality condition is written as

$$[(HPO_4)_{PO_4}^{\cdot}] + 2[(P_2O_7)_{PO_4}^{\cdot}] = n .$$

If oxygen vacancy concentration dominates,

$$2[(P_2O_7)_{PO_4}^{\cdot}] = n$$

$$2K_1 p_{O_2}^{-\frac{1}{2}} = 2K_1 K_4 p_{H_2O}^{-1} p_{H_2} = n^3 .$$

Therefore, electron and oxygen concentration are proportional to $p_{O_2}^{-\frac{1}{6}}$ and $p_{H_2}^{\frac{1}{3}} p_{H_2O}^{-\frac{1}{3}}$.

They are proportional to $p_{H_2}^{\frac{1}{3}}$ if water partial pressure is held constant in experiments.

If proton concentration dominates,

$$[(HPO_4)_{PO_4}^{\cdot}] = n$$

$$K_3 K_4^{-\frac{1}{2}} p_{H_2O}^{\frac{1}{2}} p_{O_2}^{-\frac{1}{4}} = K_3 p_{H_2}^{\frac{1}{2}} = n^2$$

Therefore, electron and proton concentration are proportional to $p_{O_2}^{-\frac{1}{8}} p_{H_2O}^{\frac{1}{4}}$ and $p_{H_2}^{\frac{1}{4}}$.

They are proportional to $p_{O_2}^{-\frac{1}{8}}$ if water partial pressure is held constant in experiments.

Case 3: high water partial pressure without free hydrogen.

Without free hydrogen, water vapor is the only proton source. Water vapor reacted with oxygen vacancies in perovskites to form protons. It also could react with pyrophosphates to form hydrogen phosphates in $Ba_3Ce(PO_4)_3$. Defect equilibrium can be written as

$$(P_2O_7)^{-}_{2PO_4} + H_2O(g) \rightarrow 2(HPO_4)_{PO_4}. \qquad \text{K5} \qquad (4\text{-}5)$$

$$K_5 = K_3^2 K_4^{-1} K_1^{-1}$$

Water vapor also could first produce bound hydrogen by reaction (4-4). Produced bound hydrogen is then oxidized, forming protons and attaching to the O atoms of PO_4 group. The whole process includes defect equilibrium (4-3) and (4-4). Defect equilibrium is simplified as

$$2(PO_4)^{x}_{PO_4} + H_2O \rightarrow 2(HPO_4)^{\cdot}_{PO_4} + 2e' + \frac{1}{2}O_2. \qquad \text{K6} \qquad (4\text{-}6)$$

$$K_6 = K_3^2 K_4^{-1} = K_5 K_1^{-1}$$

The electroneutrality condition is written as

$$[(HPO_4)^{\cdot}_{PO_4}] + 2[(P_2O_7)^{-}_{2PO_4}] = n.$$

Therefore,

$$K_3 n^{-1} p_{H_2}^{\frac{1}{2}} + 2K_1 n^{-2} p_{O_2}^{-\frac{1}{2}} = n.$$

$$(2K_1 n^{-2})(p_{O_2}^{-\frac{1}{4}})^2 + (K_3 K_4^{-\frac{1}{2}} n^{-1} p_{H_2O}^{\frac{1}{2}})(p_{O_2}^{-\frac{1}{4}}) - n = 0$$

$$p_{o_2}^{-\frac{1}{4}} = n\frac{-K_3 K_4^{-\frac{1}{2}} p_{H_2O}^{\frac{1}{2}} + \sqrt{K_3^2 K_4^{-1} p_{H_2O} + 8K_1 n}}{4K_1}.$$

It is difficult to predict defect concentration dependency of oxygen partial pressure from the above formula without the information about equilibrium constants K_1- K_6.

Case 3 is simplified into two conditions: one is oxygen vacancy concentration dominance condition and the other is proton concentration dominance condition.

If oxygen vacancy concentration still dominates in high water partial pressure condition, electroneutrality condition is simplified as

$2[(P_2O_7)^{\cdot\cdot}_{2PO_4}] = n$.

$2K_1 p_{O_2}^{-\frac{1}{2}} = 2K_1 K_4 p_{H_2O}^{-1} p_{H_2} = n^3$

Proton concentration is negligible under this hypothesis. The electron concentration and oxygen vacancy concentration are proportional to $p_{O_2}^{-\frac{1}{6}}$ and $p_{H_2O}^{-\frac{1}{3}} p_{H_2}^{\frac{1}{3}}$.

If high water partial pressure suppresses the oxygen vacancy formation and proton concentration dominates, the electroneutrality condition is written as

$[(HPO_4)^{\cdot}_{PO_4}] = n$.

Therefore,

$K_3 K_4^{-\frac{1}{2}} p_{H_2O}^{\frac{1}{2}} p_{O_2}^{-\frac{1}{4}} = n^2$

The protons and electron concentration are proportional to $p_{O_2}^{-\frac{1}{8}} p_{H_2O}^{\frac{1}{4}}$.

Mostly likely, case 3 is the mixture of these two conditions.

Case 4: high water partial pressure with free hydrogen.

Under high water partial pressure condition with free hydrogen, both water vapor and free hydrogen provide proton sources. The corresponding defect equilibriums are written as

$$(PO_4)^{x}_{PO_4} + \frac{1}{2}H_2 \rightarrow (HPO_4)^{\cdot}_{PO_4} + e' \qquad \text{K3} \qquad (4\text{-}3)$$

$$2(PO_4)^{x}_{PO_4} + H_2O \rightarrow 2(HPO_4)^{\cdot}_{PO_4} + 2e' + \frac{1}{2}O_2. \qquad \text{K6} \qquad (4\text{-}6)$$

The electroneutrality condition can be written as

$[(HPO_4)^{\cdot}_{PO_4}] + 2[(P_2O_7)^{\cdot\cdot}_{2PO_4}] = n$.

The only difference between case 3 and case 4 is that free hydrogen is involved in the proton incorporation in case 4. If we know about the information of equilibrium constants K_1 - K_6 under these two cases, the free hydrogen's contribution could easily be demonstrated. Unfortunately, no such fundamental research was reported.

Wet hydrogen belongs to case 4. For wet hydrogen treated $Ba_3Ce(PO_4)_3$, Raman spectroscopy result in figure 4-11 shows a broad band at 1350 cm^{-1}, assigned to the bending mode of POH bond, which clearly demonstrates the proton incorporation. Figure 4-11 also shows that POH vibration intensity is strong in wet hydrogen treated sample while it is negligible in dry hydrogen treated one. This indicates that water vapor plays a much more important role than free hydrogen in proton incorporation. Therefore, without further information about free hydrogen contribution, all the derivations in case 3 can approximately apply in case 4. However, the proton concentration is expected to be higher than in case 3 due to the free hydrogen contribution. Therefore, proton concentration is considered to be dominant in case 4. The electroneutrality condition is written as

$$[(HPO_4)_{PO_4}] = n .$$

$$K_3 K_4^{-\frac{1}{2}} p_{H_2O}^{\frac{1}{2}} p_{O_2}^{-\frac{1}{4}} = K_3 p_{H_2}^{\frac{1}{2}} = n^2$$

The electron concentration and proton concentration are proportional to $p_{H_2}^{\frac{1}{4}}$. The defect concentration dependence is proportional to $p_{O_2}^{-\frac{1}{8}} p_{H_2O}^{\frac{1}{4}}$.

Low-Intermediate Oxygen Partial Pressure Region

Oxygen vacancy also exists in the phosphate lattice at the low-intermediate oxygen partial pressure region and plays a similar role as that in the low oxygen partial pressure region. The following defect equilibrium also exists:

$$2(PO_4)^x_{PO_4} \rightarrow (P_2O_7)^{\cdot\cdot}_{2PO_4} + 2e^{'} + \frac{1}{2}O_2 . \qquad \text{K1} \qquad (4\text{-}1)$$

However, oxygen vacancy concentration is smaller at this low-intermediate oxygen partial pressure region. Hole concentration can still be omitted. The total defect concentration is lower than that in the low oxygen partial pressure region.

With a small trace of free hydrogen, the oxygen partial pressure will decrease to $p_{O_2} < 10^{-15}\, atm$. Therefore, case 2 (low water partial pressure condition with free hydrogen) did not exist in the low-intermediate region. Only cases 1, 3 and 4 were discussed in this region. Case 1 is the low water partial pressure condition without free hydrogen, case 3 is the high water partial pressure condition without free hydrogen, and case 4 is the high water partial pressure condition with free hydrogen.

Case 1: low water partial pressure without free hydrogen.

Under low water partial pressure condition without free hydrogen, there is no proton source for $Ba_3Ce(PO_4)_3$. Oxygen vacancies are the only positive defects to charge balance electrons. Therefore, the electroneutrality condition is simplified as

$$2[(P_2O_7)^{\cdot\cdot}_{2PO_4}] = n .$$

Therefore,

$$K_1 = [n/2]n^2 p_{O_2}^{\frac{1}{2}} .$$

The electron concentration and oxygen vacancy concentration are proportional to $p_{O_2}^{-\frac{1}{6}}$. There is no water partial pressure dependence due to low water partial pressure condition. Without a proton source, there is also no hydrogen partial pressure dependence.

Case 3: high water partial pressure without free hydrogen.

Without free hydrogen, water vapor is the only proton source. Water vapor could react with oxygen vacancies to form protons. It also could first produce bound hydrogen. Produced bound hydrogen is then oxidized, forming protons and attaching to the O atoms of PO_4 group. The corresponding defect equilibriums can be written as

$$(P_2O_7)_{2PO_4}^{\cdot\cdot} + H_2O(g) \rightarrow 2(HPO_4)_{PO_4}^{\cdot} . \qquad \text{K5} \qquad (4\text{-}5)$$

$$2(PO_4)_{PO_4}^{x} + H_2O \rightarrow 2(HPO_4)_{PO_4}^{\cdot} + 2e' + \frac{1}{2}O_2 . \qquad \text{K6} \qquad (4\text{-}6)$$

The electroneutrality condition is written as

$$[(HPO_4)_{PO_4}^{\cdot}] + 2[(P_2O_7)_{2PO_4}^{\cdot\cdot}] = n .$$

There still exist two possibilities: one is proton concentration dominance and the other is oxygen vacancy concentration dominance.

If oxygen vacancy concentration dominates in high water partial pressure condition, then electroneutrality condition is simplified as

$$2[(P_2O_7)_{2PO_4}^{\cdot\cdot}] = n .$$

$$2K_1 p_{O_2}^{-\frac{1}{2}} = 2K_1K_4 p_{H_2O}^{-1} p_{H_2} = n^3$$

Proton concentration is negligible under this hypothesis. The electron concentration and oxygen vacancy concentration are proportional to $p_{O_2}^{-\frac{1}{6}}$ and $p_{H_2O}^{-\frac{1}{3}} p_{H_2}^{\frac{1}{3}}$.

If proton concentration dominates, the electroneutrality condition is written as

$[(HPO_4)^{\cdot}_{PO_4}] = n$.

$$K_3 K_4^{-\frac{1}{2}} p_{H_2O}^{\frac{1}{2}} p_{O_2}^{-\frac{1}{4}} = K_3 p_{H_2}^{\frac{1}{2}} = n^2$$

The proton and electron concentration are proportional to $p_{O_2}^{-\frac{1}{8}} p_{H_2O}^{\frac{1}{4}}$.

Without free hydrogen, the defect concentration dependence of hydrogen partial pressure was not further derived in this case.

Case 4: high water partial pressure with free hydrogen.

Under high water partial pressure condition with free hydrogen, both water vapor and free hydrogen provide proton sources. Their corresponding defect equilibriums are written as

$$(PO_4)^{x}_{PO_4} + \frac{1}{2} H_2 \rightarrow (HPO_4)^{\cdot}_{PO_4} + e' \qquad \text{K3} \qquad (4\text{-}3)$$

$$2(PO_4)^{x}_{PO_4} + H_2O \rightarrow 2(HPO_4)^{\cdot}_{PO_4} + 2e' + \frac{1}{2} O_2 . \qquad \text{K6} \qquad (4\text{-}6)$$

The electroneutrality condition can be written as

$[(HPO_4)^{\cdot}_{PO_4}] + 2[(P_2O_7)^{\cdot}_{2PO_4}] = n$.

The only difference between case 3 and case 4 is that free hydrogen is involved in the proton incorporation in case 4. However, the free hydrogen concentration is not high at the low-intermediate oxygen partial pressure region. Its contribution can be omitted compared with water vapor contribution. All the derivations in case 3 can approximately apply in case 4.

If oxygen vacancy concentration dominates, the electron concentration and oxygen vacancy concentration are proportional to $p_{o_2}^{-\frac{1}{6}}$ and $p_{H_2}^{\frac{1}{3}} p_{H_2O}^{-\frac{1}{3}}$.

If proton concentration dominates, the proton and electron concentration are proportional to $p_{H_2}^{\frac{1}{4}}$ and $p_{O_2}^{-\frac{1}{8}} p_{H_2O}^{\frac{1}{4}}$.

Intermediate Oxygen Partial Pressure Region

There is no free hydrogen in the intermediate oxygen partial pressure region and water vapor is the only possible proton source. Two cases were discussed in this region. One is the low water partial pressure condition and the other is high water partial pressure condition.

Case1: low water partial pressure

Dry nitrogen gas belongs to case 1. Raman spectroscopy result in figure 4-9 suggests that oxygen vacancy exists in the dry nitrogen treated $Ba_3Ce(PO_4)_3$. However, oxygen vacancy concentration is lower in dry nitrogen than in dry hydrogen.

The corresponding defect equilibrium in the dry atmosphere is written as

$$2(PO_4)_{PO4}^{\times} \rightarrow (P_2O_7)_{2PO_4}^{\cdot\cdot} + \frac{1}{2}O_2 + 2e' \qquad \text{K1} \qquad (4\text{-}1)$$

The electroneutrality condition is written as

$$2[(P_2O_7)_{2PO_4}^{\cdot\cdot}] + p = n .$$

Despite the fact that the electron and hole concentrations are not high due to the phosphate structure and the intermediate oxygen partial pressure; however, they could not be omitted. The electron concentration restricts the oxygen vacancy and hole concentration. Therefore, the total defect concentration in this region is expected to be low. There is no apparent oxygen partial pressure dependency under this condition.

Case 2: high water partial pressure.

Wet nitrogen belongs to case 2. Water vapor is the only proton source in wet nitrogen. Raman spectroscopy in figure 4-10 provides some information about the proton incorporation under this condition. The stretching mode of absorbed water molecule at 3333cm^{-1} did not appear in the wet nitrogen treated $Ba_3Ce(PO_4)_3$, suggesting that no water molecules were inserted in the lattice. The stretching modes at 2881, 2848cm^{-1} and bending modes at 1439, 1295, 1131cm^{-1} of POH in figure 4-10 indicated that protons are inserted in the lattice. This indicates that water vapor produces bound hydrogen and the produced bound hydrogen is then oxidized, forming protons. The protons are attached to O atoms of PO_4 group and incorporated into the lattice.

The corresponding defect equilibrium in wet atmosphere is written as

$$2(PO_4)^x_{PO_4} + H_2O \rightarrow 2(HPO_4)^{\cdot}_{PO_4} + 2e' + \frac{1}{2}O_2 . \qquad \text{K6} \qquad (4\text{-}6)$$

The electroneutrality condition is written as

$$[(HPO_4)^{\cdot}_{PO_4}] + 2[(P_2O_7)^{\cdot\cdot}_{2PO_4}] + p = n .$$

Based on defect equilibrium (4-6), proton concentration and electron concentration increase in the presence of water vapor. However, electron concentration is not high and almost equals hole concentration in the intermediate oxygen partial pressure region, which restricts the proton concentration based on the electroneutrality condition. Therefore, the total defect concentration will not change much in the presence of water vapor in the intermediate region. Their dependence of oxygen partial or water partial pressure will not be apparent in this region.

High Oxygen Partial Pressure Region

We do not know of any appropriate negative ionic species. Therefore, electrons are the only negative defects to charge balance holes, oxygen vacancies and possible protons. Oxygen vacancy concentration could be omitted in this region. In the presence of water vapor, equal amounts of protons and electrons were incorporated into the lattice based on reaction (4-6). However, electron concentration is usually lower than hole concentration under high oxygen partial pressure region. Extra negative defects are needed to charge balance holes.

The following defect equilibriums can exist in the high oxygen partial pressure region:

$$2(PO_4)^x_{PO_4} \rightarrow (P_2O_7)^{\cdot\cdot}_{2PO_4} + 2e' + \frac{1}{2}O_2 . \qquad \text{K1} \qquad (4\text{-}1)$$

$$2(PO_4)^x_{PO_4} + H_2O \rightarrow 2(HPO_4)^{\cdot}_{PO_4} + 2e' + \frac{1}{2}O_2 . \qquad \text{K6} \qquad (4\text{-}6)$$

The electroneutrality condition under dry atmosphere is written as

$$2[(P_2O_7)^{\cdot\cdot}_{2PO_4}] + p = n .$$

The electroneutrality condition under wet atmosphere is written as

$$[(HPO_4)^{\cdot}_{PO_4}] + 2[(P_2O_7)^{\cdot\cdot}_{2PO_4}] + p = n .$$

However, as stated above, electrons should not be a primary species at high oxygen partial pressure. Therefore, the defect structure model in this region faces a challenge and more studies are needed. The defect concentration dependencies of oxygen partial pressure are not further derived due to the challenge we pointed out.

4.3.5 Chemical and Thermal Stability

Figure 4-13 is the high temperature XRD of $Ba_3Ce(PO_4)_3$ in the helium atmosphere. The peak at 2θ=48° came from the result of the silver paste used as an adhesive. All the peak positions moved to lower angles with increasing temperature, suggesting the corresponding lattice expansion during heating. No second phase was detected, suggesting that the stability of $Ba_3Ce(PO_4)_3$ is good in helium up to 600 ºC.

The XRD in Figure 4-14 shows little difference between $Ba_3Ce(PO_4)_3$ samples after separate treatments in argon, air, and hydrogen atmosphere at 600 ºC for 10 h. This can be regarded as an indication of stability of $Ba_3Ce(PO_4)_3$ in air, argon, and hydrogen.

4.3.6 Thermal Expansion

The thermal expansion behavior of $Ba_3Ce(PO_4)_3$ in air and hydrogen is shown in Figure 4-15. The thermal expansion coefficients of $Ba_3Ce(PO_4)_3$ in the hydrogen and air atmospheres were 18×10^{-6} /°C and 15×10^{-6} /°C, respectively.

4.4 Conclusion

Single-phase $Ba_3Ce(PO_4)_3$ was synthesized successfully by a coprecipitation method. $Ba_3Ce(PO_4)_3$ is stable in dry air, argon and hydrogen atmospheres. Its thermal expansion coefficients in dry hydrogen and air atmosphere are 18×10^{-6} /°C and 15×10^{-6} /°C, respectively. Raman and NMR characterization results indicate that hydrogen phosphate exists in the $Ba_3Ce(PO_4)_3$ under wet atmospheres and dry hydrogen. A defect structure was proposed based on characterization results. The relationships between concentration of defects and oxygen partial pressure or water partial pressure are

predicted. The conductivities of $Ba_3Ce(PO_4)_3$ will be measured in the next chapter to assure the proposed defect structure model.

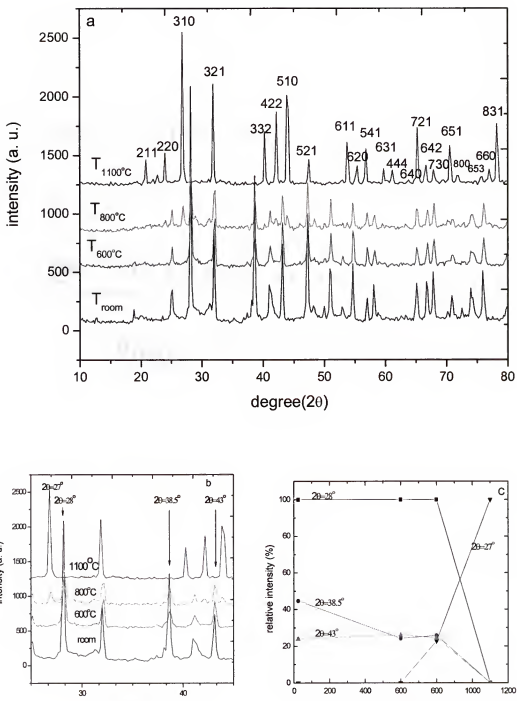

Figure 4-1. XRD patterns of calcined precipitate with different calcination temperatures. (a) XRD pattern between 2θ=10-80°, (b) magnified XRD pattern between 2θ=25-45° and (c) XRD peak intensity versus calcination temperature.

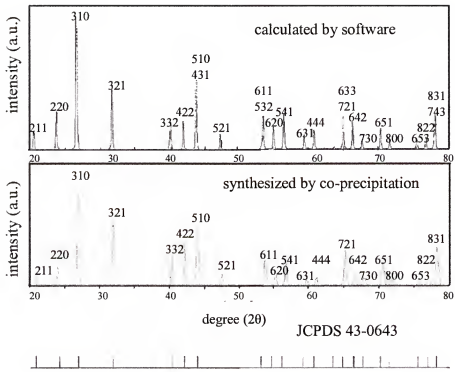

Figure 4-2. Compare XRD results from JCPDS, experiment and calculation by CaRIne Crystallography V3.1 software.

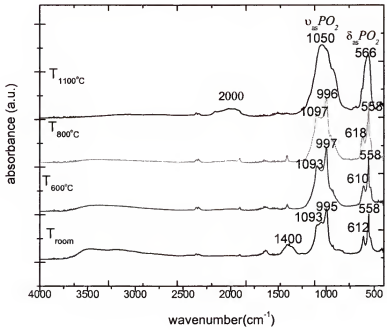

Figure 4-3. IR of precipitates after calcining at different temperatures for 4 h.

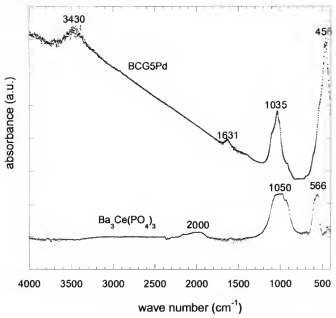

Figure 4-4. IR spectra of $Ba_3Ce(PO_4)_3$ and composite BCG5Pd.

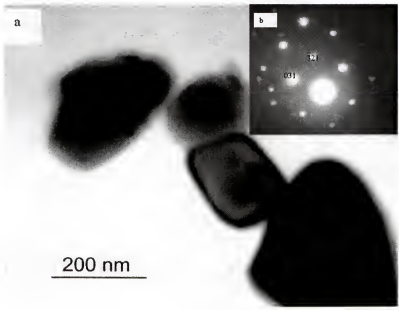

Figure 4-5. Bright field image and selected area diffraction pattern of $Ba_3Ce(PO_4)_3$ particle. (a) Bright field image and (b) selected area diffraction pattern.

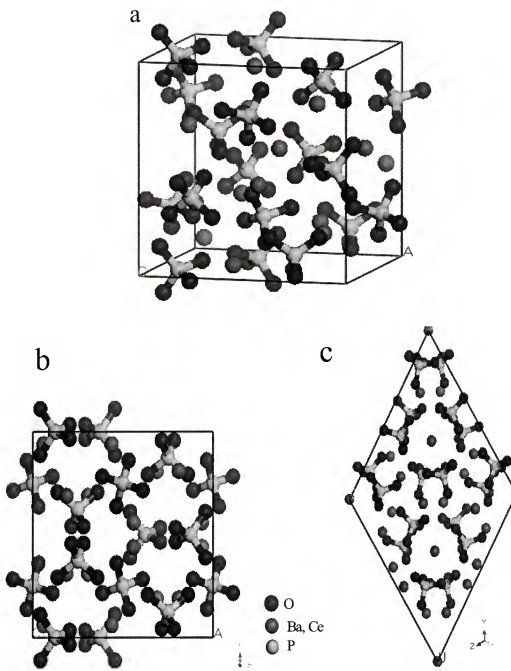

Figure 4-6. Crystal structure of $Ba_3Ce(PO_4)_3$ using "MS modeling" software. (a) 3-D view, (b) [001] directional view, and (c) [111] directional view of the crystal structure.

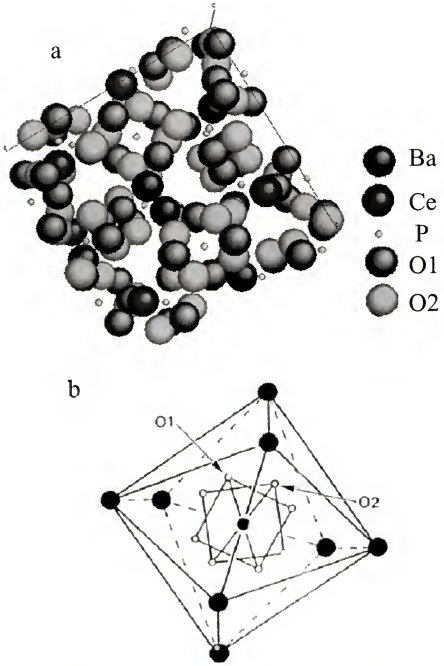

Figure 4-7. Crystal structure of $Ba_3Ce(PO_4)_3$ using "CaRIne Crystallography V3.1" software. (a) 3-D view and (b) [001] directional view of $Ba_3La(PO_4)_3$ (from ref [76]).

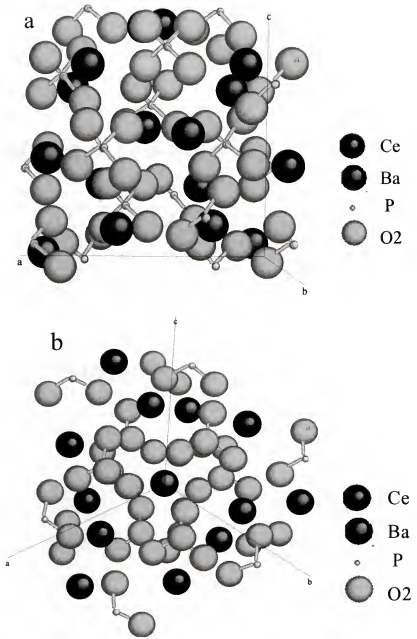

Figure 4-8. Directional view of $Ba_3Ce(PO_4)_3$. (a) [010] and (b) [111].

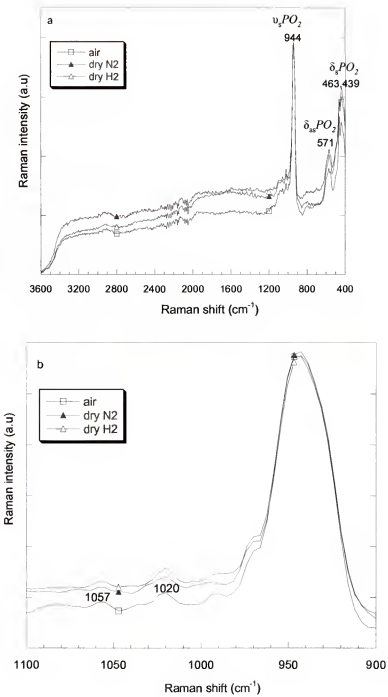

Figure 4-9. Raman spectra of $Ba_3Ce(PO_4)_3$ after dry air, N_2 and H_2 treatment. (a) at 400-3600 cm^{-1} and (b) at 900-1100 cm^{-1} region.

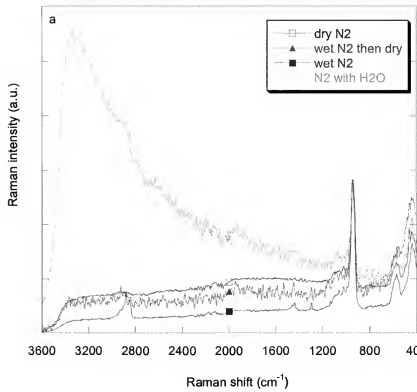
a
dry N2
wet N2 then dry
wet N2
N2 with H2O
Raman intensity (a.u.)
3600 3200 2800 2400 2000 1600 1200 800 400
Raman shift (cm-1)

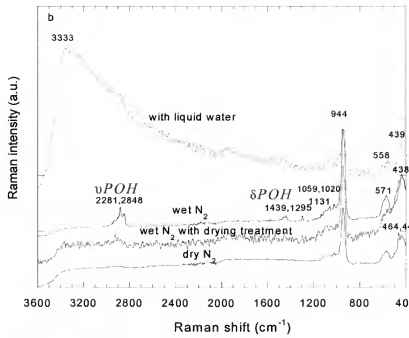
b
3333
with liquid water
944
439
558
438
υPOH
2281,2848
δPOH
1059,1020
1131
1439,1295
571
wet N2
wet N2 with drying treatment
464,441
dry N2
Raman intensity (a.u.)
3600 3200 2800 2400 2000 1600 1200 800 400
Raman shift (cm-1)

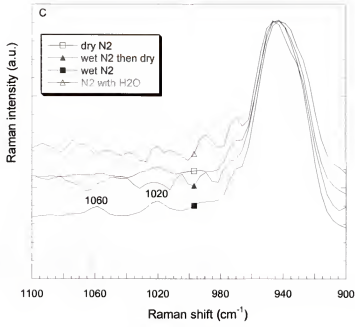

Figure 4-10. Raman spectra of $Ba_3Ce(PO_4)_3$ after wet and dry nitrogen treatment. (a, b) at 400-3600 cm^{-1} and (c) at 900-1100 cm^{-1} region. The band intensities in (a) were adjusted to show the band position in (b).

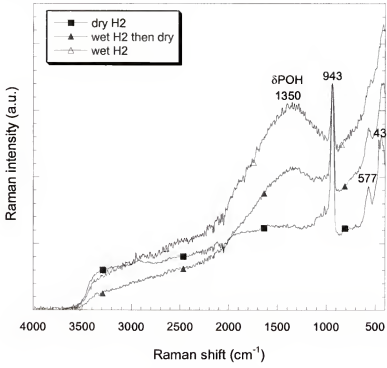

Figure 4-11. Raman spectra of $Ba_3Ce(PO_4)_3$ after wet hydrogen treatment.

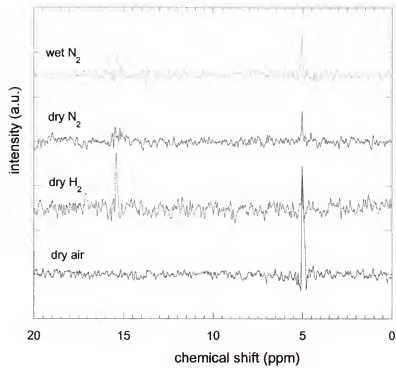

Figure 4-12. High- resolution ^{1}H NMR spectra of $Ba_3Ce(PO_4)_3$ after different gas treatment at 550ºC for 24 h.

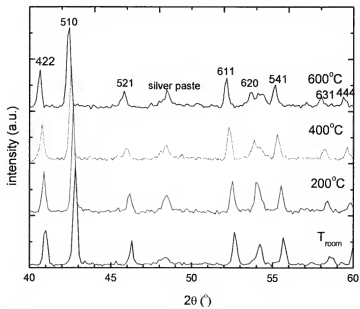

Figure 4-13. High-temperature XRD pattern of $Ba_3Ce(PO_4)_3$.

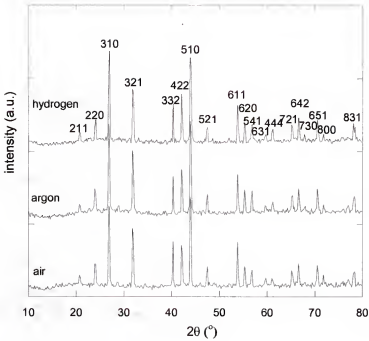

Figure 4-14. XRD of $Ba_3Ce(PO_4)_3$ after different atmosphere treatments at 600 ºC for 10 h.

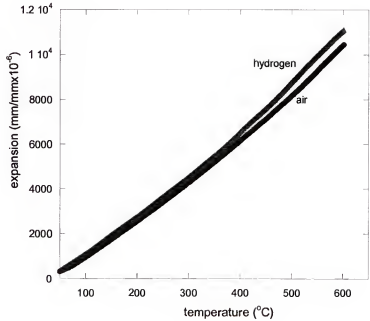

Figure 4-15. Thermal expansion behavior of $Ba_3Ce(PO_4)_3$ in hydrogen and air atmosphere.

Table 4-1. Measured spacing d compared with those obtained from TEM result and literature value*.

Coprecipitation method a=10.4466 Å			Literature a=10.5112 Å		Coprecipitation method a=10.4466 Å			Literature a=10.5112 Å
(hkl)	$d_{experiment.}$	$d_{TEM.}$	$d_{literature}$		(hkl)	$d_{experiment.}$	$d_{TEM.}$	$d_{literature}$
211	4.2458	4.2648	4.2922		631	1.5449	1.5403	1.5496
220	3.6897	3.6934	3.7145		444	1.5128	1.5078	1.5174
310	3.2960	3.3035	3.3244		721	1.4275	1.4216	1.4305
321	2.7916	2.7919	2.8093		642	1.4017	1.3960	1.4046
332	2.2271	2.2272	2.2415		730	1.3768	1.3717	1.3804
422	2.1361	2.1324	2.1459		651	1.3322	1.3267	1.3349
510	2.0529	2.0487	2.0615		800	1.3120	1.3058	1.3138
521	1.9128	1.9073			653	1.2542	1.2486	1.2562
611	1.7016	1.6947	1.7052		660	1.2379	1.2311	1.2388
620	1.6561	1.6518	1.6624		830	1.2209	1.2144	1.2219

*In coprecipitation method, coprecipitates were sintering at 1100 ºC for 4 h;
In literature JCPDS 43-0643, mixture were sintered at 1000 °C for one day and 1350 °C for 10 days

Table 4-2. Wavenumbers (cm^{-1}) of the absorption bands in infrared spectra of $Ba_3Ce(PO_4)_3$

	$\upsilon_1(cm^{-1})$	$\upsilon_2(cm^{-1})$	$\upsilon_3(cm^{-1})$	$\upsilon_4(cm^{-1})$
T_{room}	3465	1635	1093, 995	612, 558
$T_{600ºC}$	3391	1653	1093, 997	610, 558
$T_{800ºC}$	3391	------	1097, 996	618, 558
$T_{1100ºC}$	------	------	1050	566

υ_1: stretching vibration of water
υ_2: bending vibration of water
υ_3: asymmetric stretching vibration, $\nu_{as}PO_2$
υ_4: asymmetric bending vibration, $\delta_{as}PO_2$

Table 4-3. Raman shift of $Ba_3Ce(PO_4)_3$ at dry atmosphere compared with Sr doped $LaPO_4$

Functional Group	Raman shift (cm^{-1}) Sr-doped $LaPO_4$ [42]		Raman shift (cm^{-1}) $Ba_3Ce(PO_4)_3$
PO_4^{3-}	1073, 1065, 1055 and 1025	asymmetric stretching	1057, 1020
	991 and 967	symmetric stretching	944
	619, 589,571,559 and 537	O-P-O F2-bending	571
	466,416 and 395	O-P-O E-bending	463 and 439
$P_2O_7^{4-}$	1036,764, 728		1057 and 1020 [41]

Table 4-4. Raman shift of $Ba_3Ce(PO_4)_3$ at wet atmosphere compared with Sr doped $LaPO_4$

	Raman (cm^{-1})	Raman (cm^{-1}) $Ba_3Ce(PO_4)_3$		
	Sr-doped $LaPO_4$ [42]	wet N_2	wet H_2	assignment
PO_4^{3-}	1073			asymmetric stretching
	1065			
	1055	1059		
	1025	1020		
	991			symmetric stretching
	967	944	944	
	619			asymmetric bending
	589			
	571	571	577	
	559			
	537			
	466			symmetric bending
	416	438	438	
	395			
HPO_4^{2-}				stretching of water
		2881		stretching of POH
		2848		
		1439	1350	bending of POH
		1295		
	1135	1131		POH in plane bending
	672			POH out-of-plane bending

Table 4-5. Chemical shift of ^1H NMR of $Ba_3Ce(PO_4)_3$ after different atmosphere treatments compared with Sr doped $LaPO_4$

Sr-doped $LaPO_4$ [42]	$Ba_3Ce(PO_4)_3$			
	dry air	dry H_2	dry N_2	wet N_2
Water molecules	5 ppm	5 ppm	5 ppm	5 ppm
5.4 and 1.2 ppm	largest intensity			
Proton		15 ppm	15 ppm	15 ppm
12.4 ppm		largest intensity	(noise)	

Table 4-6. Defect concentration dependence of p_{H_2}, p_{O_2} and p_{H_2O}.

p_{O_2}	p_{H_2O}, p_{H_2}	n	$[(P_2O_7)'_{2PO_4}]$	$[(HPO_4)'_{PO_4}]$
		p_{H_2}, p_{O_2}, p_{H_2O}	p_{H_2}, p_{O_2}, p_{H_2O}	p_{H_2}, p_{O_2}, p_{H_2O}
Low	Low p_{H_2O} No free H_2	$p_{O_2}^{-\frac{1}{6}}$	$p_{O_2}^{-\frac{1}{6}}$	no
	Low p_{H_2O} With p_{H_2}	$p_{H_2}^{\frac{1}{3}} p_{H_2O}^{-\frac{1}{3}}$, $p_{O_2}^{-\frac{1}{6}}$ $p_{H_2}^{\frac{1}{4}}$, $p_{O_2}^{-\frac{1}{8}} p_{H_2O}^{\frac{1}{4}}$	$p_{H_2}^{\frac{1}{3}} p_{H_2O}^{-\frac{1}{3}}$, $p_{O_2}^{-\frac{1}{6}}$ negligible	negligible $p_{H_2}^{\frac{1}{4}}$, $p_{O_2}^{-\frac{1}{8}} p_{H_2O}^{\frac{1}{4}}$
	High p_{H_2O} No free H_2	$p_{O_2}^{-\frac{1}{8}} p_{H_2O}^{\frac{1}{4}}$ $p_{H_2}^{\frac{1}{3}} p_{H_2O}^{-\frac{1}{3}}$, $p_{O_2}^{-\frac{1}{6}}$	negligible $p_{H_2}^{\frac{1}{3}} p_{H_2O}^{-\frac{1}{3}}$, $p_{O_2}^{-\frac{1}{6}}$	$p_{O_2}^{-\frac{1}{8}} p_{H_2O}^{\frac{1}{4}}$ negligible
	High p_{H_2O} With p_{H_2}	$p_{H_2}^{\frac{1}{4}}$, $p_{O_2}^{-\frac{1}{8}} p_{H_2O}^{\frac{1}{4}}$	negligible	$p_{H_2}^{\frac{1}{4}}$, $p_{O_2}^{-\frac{1}{8}} p_{H_2O}^{\frac{1}{4}}$
Low-intermediate	Low p_{H_2O} No free H_2	$p_{O_2}^{-\frac{1}{6}}$	$p_{O_2}^{-\frac{1}{6}}$	no
	High p_{H_2O} No free H_2	$p_{O_2}^{-\frac{1}{8}} p_{H_2O}^{\frac{1}{4}}$ $p_{H_2}^{\frac{1}{3}} p_{H_2O}^{-\frac{1}{3}}$, $p_{O_2}^{-\frac{1}{6}}$	negligible $p_{H_2}^{\frac{1}{3}} p_{H_2O}^{-\frac{1}{3}}$, $p_{O_2}^{-\frac{1}{6}}$	$p_{O_2}^{-\frac{1}{8}} p_{H_2O}^{\frac{1}{4}}$ negligible
	High p_{H_2O} With p_{H_2}	$p_{H_2}^{\frac{1}{4}}$, $p_{O_2}^{-\frac{1}{8}} p_{H_2O}^{\frac{1}{4}}$ $p_{H_2}^{\frac{1}{3}} p_{H_2O}^{-\frac{1}{3}}$, $p_{O_2}^{-\frac{1}{6}}$	negligible $p_{H_2}^{\frac{1}{3}} p_{H_2O}^{-\frac{1}{3}}$, $p_{O_2}^{-\frac{1}{6}}$	$p_{H_2}^{\frac{1}{4}}$, $p_{O_2}^{-\frac{1}{8}} p_{H_2O}^{\frac{1}{4}}$ negligible
Intermediate	Low p_{H_2O}	n, p, $[(P_2O_7)'_{2PO_4}]$ are low, no apparent dependence		no
	High p_{H_2O}	n, p, $[(P_2O_7)'_{2PO_4}]$, $[(HPO_4)'_{PO_4}]$ are low, no apparent dependence		
High	Electroneutrality condition faces a challenge, no further discussion			

CHAPTER 5
CONDUCTIVITY MEASUREMENT OF $Ba_3Ce(PO_4)_3$

5.1 Introduction

The defect structure of $Ba_3Ce(PO_4)_3$ was proposed in chapter 4 based on characterization results. The relationship between charge carrier concentration, oxygen partial pressure and water partial pressure was derived. The measured conductivities of $Ba_3Ce(PO_4)_3$ are presented in this chapter to test the proposed defect structure model.

5.2 Experiment

$Ba_3Ce(PO_4)_3$ powder was pressed into pellets, cold isostatic pressed at 200 MPa and sintered at 1100, 1200, 1300 °C for 8 h. SEM was used to characterize the microstructure of the sintered pellets. Platinum paint was applied on each side of polished $Ba_3Ce(PO_4)_3$ pellets and platinum wire was fastened to the electrode. They were sintered at 1050°C for half an hour.

Conductivities were measured by two-point method with a Solartron 1260 frequency response analyzer. For conductivity measurements in wet and dry oxygen, air, nitrogen and 4vol% hydrogen atmospheres in the 300-600 °C region, gas flow rates were controlled at 50 sccm.

For conductivity measurements as a function of oxygen partial pressure, the oxygen partial pressure range 10^{-26}~10^{-19} atm was achieved by mixing argon with hydrogen. The oxygen partial pressure range 10^{-20}~10^{-17} atm was achieved by purifing argon gas through titanium charger at 800°C to remove oxygen. The oxygen partial pressure range 10^{-14}~10^{-}

^{11} atm was obtained by bubbling purified argon gas through water at room temperature. The oxygen partial pressure range 10^{-25}~10^{-7} atm was also obtained by bubbling mixture of hydrogen and argon through water at room temperature. The oxygen partial pressure range 10^{-7}~10^{-1} atm was achieved by using an oxygen pump (SGM5EL) with argon gas. The oxygen partial pressure range 0.21~1 atm was obtained by mixing argon and oxygen.

An oxygen sensor (SGM5EL) with operating temperature 750 °C monitored the oxygen partial pressure. The actual oxygen partial pressure at the testing temperature was calculated using thermodynamic equations.

5.3 Results and Discussion

5.3.1 Sintering and Density Issue

Figure 5-1 shows the relationship between the sample's density and sintering temperature with a dwell time of 8 h. Figure 5-2 shows XRD results with different sintering temperatures and dwell times. Figure 5-3 shows the SEM cross-section view of the sintered pellets with magnification 3500. As expected, the relative density increased with sintering temperature, from 78% at 1100 °C, to 89% at 1200 °C, to 95% at 1300 °C. However, the pellet sintered at 1300 °C, changed its color to green and a glassy phase was observed. The XRD result (shown in figure 5-2) shows that impurity phase $Ba_2P_2O_7$ was produced at high temperature. For pellets sintered at 1100 and 1200°C for 8h, there was no second phase detected. This is similar to Sr doped $LaPO_4$. Sr doped $LaPO_4$ sintered at 1350 °C has a second phase, $Sr_2P_2O_7$, and the resulting conductivity of the material is lower than that sintered at 1200 °C [42]. Therefore, we chose 1200 °C as the sintering temperature. We sintered pellets at 1200 °C for 8 h, 16 h and 24 h, respectively. The relative density was 91% with a sintering temperature of 1200 °C for 24 h. However, XRD in figure 5-2 shows the existence of impurity phase $Ba_2P_2O_7$, which would lower

conductivity. A dwell time of 8 h was chosen to assure no second phase was produced during the sintering. The porosity decreased extensively with increasing sintering temperature based on a SEM cross-section image. There were no interconnected pores in the cross section with a relative density 89%.

Samples used for conductivity measurements were batch sintered at 1200 °C for 8 h. Figure 5-3 shows the cross-section image of sintered $Ba_3Ce(PO_4)_3$ with magnification 3500. Figure 5-4 shows the SEM surface image of a porous Pt electrode on a $Ba_3Ce(PO_4)_3$ sample with magnification 1500.

5.3.2 Conductivity

5.3.2.1 Conductivity in different atmospheres

Atmosphere and Water Vapor Effects on the Impedance Plots

Figure 5-5 (a-d) illustrates the atmosphere and water vapor effects on the impedance plot of $Ba_3Ce(PO_4)_3$ at 600ºC. The impedance discontinuity at frequency around 1×10^6 Hz is an artifact. Figure 5-5 (e-f) enlarges the impedance plot of $Ba_3Ce(PO_4)_3$ in wet and dry 4vol% hydrogen in figure 5-5 (d) to show the electrolyte and electrode semicircle. The semicircle with high frequency belongs to the electrolyte and the semicircle with low frequency belongs to the electrode. The capacitances of the high frequency and low frequency semicircles are on the order of pF and nF, respectively.

Under pure oxygen, the impedance of $Ba_3Ce(PO_4)_3$ changed little by the presence of water vapor. Under pure air or nitrogen, the impedance decreased slightly in the presence of water vapor, suggesting the existence of proton conduction. Under 4vol% hydrogen, the impedance decreased significantly in the presence of water vapor.

Impedances of $Ba_3Ce(PO_4)_3$ also decreased significantly under 4vol% dry hydrogen compared with those under dry nitrogen or oxygen.

The proposed defect structures in chapter 4 are used to explain these atmosphere and water vapor effects on the impedance plot of $Ba_3Ce(PO_4)_3$.

Oxygen Atmosphere (High Oxygen Partial Pressure Region):

The defect equilibria under oxygen atmosphere are

$$2(PO_4)^x_{PO_4} \rightarrow (P_2O_7)^{\cdot}_{2PO_4} + 2e^{'} + \frac{1}{2}O_2 . \qquad \text{K1} \qquad (4\text{-}1)$$

$$2(PO_4)^x_{PO_4} + H_2O \rightarrow 2(HPO_4)^{\cdot}_{PO_4} + 2e^{'} + \frac{1}{2}O_2 . \qquad \text{K6} \qquad (4\text{-}6)$$

The electroneutrality condition can be written as

$$[(HPO_4)^{\cdot}_{PO_4}] + 2[(P_2O_7)^{\cdot}_{2PO_4}] + p = n .$$

Electrons are the only negative defects to charge balance holes, oxygen vacancies and possible protons. The oxygen vacancy concentration could be omitted in this region. However, electron concentration is usually not higher than hole concentration under high oxygen partial pressure region. Therefore, the proton concentration will not increase much in the presence of water vapor based on the electroneutrality restriction and as indicated by the impedance data of $Ba_3Ce(PO_4)_3$ (fig. 5-5a).

Nitrogen Atmosphere (Intermediate Oxygen Partial Pressure Region):

Dry nitrogen belongs to the intermediate oxygen partial pressure region. The Raman spectroscopy result in figure 4-9 suggests that oxygen vacancies exist in the dry nitrogen treated sample. The corresponding defect equilibrium in the dry atmosphere can be written as

$$2(PO_4)^x_{PO4} \rightarrow (P_2O_7)^{\cdot}_{2PO_4} + \frac{1}{2}O_2 + 2e^{'} \qquad \text{K1} \qquad (4\text{-}1)$$

The electroneutrality condition can be written as

$$2[(P_2O_7)^{\cdot}_{2PO_4}] + p = n .$$

Wet nitrogen also belongs to the intermediate oxygen partial pressure region. Raman spectroscopy result in figure 4-9 confirmed the proton incorporation by the stretching modes at 2881, 2848cm^{-1} and bending modes at 1439, 1295, 1131cm^{-1} of POH bond. The corresponding defect equilibrium in wet atmosphere can be written as

$$2(PO_4)^{x}_{PO_4} + H_2O \rightarrow 2(HPO_4)^{\cdot}_{PO_4} + 2e' + \frac{1}{2}O_2 . \qquad \text{K6} \qquad (4\text{-}6)$$

The electroneutrality condition can be written as

$$[(HPO_4)^{\cdot}_{PO_4}] + 2[(P_2O_7)^{\cdot}_{2PO_4}] + p = n .$$

Protons are incorporated into the lattice and make a contribution to the total conductivity in the presence of water vapor. However, the electron concentration almost equals the hole concentration in the intermediate oxygen partial pressure region, which restricts the proton concentration based on the electroneutrality condition. Therefore, the impedance will increase but will not increase much in the presence of water vapor in the nitrogen atmosphere, which is demonstrated by figure 5-5 (c).

Hydrogen Atmosphere (Low Oxygen Partial Pressure Region):

For dry hydrogen treated $Ba_3Ce(PO_4)_3$, chemical shift at 15 ppm in the ^{1}H NMR spectroscopy result in figure 4-12 clearly demonstrates proton insertion into the lattice. The corresponding defect equilibrium can be written as

$$(PO_4)^{x}_{PO_4} + \frac{1}{2}H_2 \rightarrow (HPO_4)^{\cdot}_{PO_4} + e' \qquad \text{K3} \qquad (4\text{-}3)$$

For wet hydrogen treated $Ba_3Ce(PO_4)_3$, the broad band at 1350 cm^{-1} in Raman spectroscopy result in figure 4-11 is assigned to the bending mode of POH bonds,

suggesting the proton incorporation. The corresponding defect equilibrium can be written as

$$(PO_4)^x_{PO_4} + \frac{1}{2}H_2 \rightarrow (HPO_4)^{\cdot}_{PO_4} + e^{'} \qquad \text{K3} \qquad (4\text{-}3)$$

$$2(PO_4)^x_{PO_4} + H_2O \rightarrow 2(HPO_4)^{\cdot}_{PO_4} + 2e^{'} + \frac{1}{2}O_2 . \qquad \text{K6} \qquad (4\text{-}6)$$

The electroneutrality condition in wet or dry hydrogen can be written as

$$[(HPO_4)^{\cdot}_{PO_4}] + 2[(P_2O_7)^{\cdot}_{2PO_4}] = n .$$

With the presence of hydrogen gas, proton and electron concentration increase due to the reaction (4-3). The mobility of proton or electron is much larger than that of oxygen vacancy. Therefore, the impedance of $Ba_3Ce(PO_4)_3$ decrease significantly under dry hydrogen atmosphere compared with dry oxygen or dry nitrogen.

Free hydrogen is the only proton source in dry hydrogen while both water vapor and free hydrogen provide protons in wet hydrogen. In the Raman results of figure 4-11, the POH bending band intensity is very strong in wet hydrogen treated $Ba_3Ce(PO_4)_3$ while it is almost undetectable in dry hydrogen treated sample. The intensity difference indicated that water vapor plays a much more important role and proton concentration is much higher in wet hydrogen. Therefore, the conductivity contribution from protons is expected to be larger in wet hydrogen than in dry hydrogen, which is demonstrated by figure 5-5 (d).

Atmosphere and Water Vapor Effects on the Arrhenius Plots

The bulk electrical resistance (R) values were obtained from the low frequency intercept of the first semicircle on the real axis of the impedance plot. The conductivity (σ) can be expressed as

$$\sigma = \frac{L}{A^* R} = \frac{L}{\frac{1}{4}\pi d^2 R} \tag{5-1}$$

where A is the cross sectional area.

The electrical transport behavior can be represented by the equation:

$$\sigma T = \sigma_0 \exp(-\frac{E_a}{kT}) \tag{5-2}$$

where σ_0 is the pre-exponential term, E_a is the activation energy, k is Boltzmann constant and T is absolute temperature. The plot of $\log(\sigma T)$ versus 1/T yields information about the pre-exponential term and the activation energy.

Figure 5-6 shows a Arrhenius plot of $\log(\sigma T)$ versus 1000/T for $Ba_3Ce(PO_4)_3$ in dry and wet oxygen, air, nitrogen, and 4vol% hydrogen at 300-600 °C. Table 5-1 lists the electrical conductivity data of $Ba_3Ce(PO_4)_3$ in different atmospheres. The conductivity of $Ba_3Ce(PO_4)_3$ at 600°C was 8.93×10^{-6} S/cm in wet air and 5.8×10^{-6} S/cm in dry air. This conductivity behavior indicates that proton conduction exists. The activation energy in dry and wet air was 0.821 and 0.810 eV, respectively, which is similar to the activation energy reported for Ca or Sr doped $LaPO_4$ at moderate temperature [27]. The conductivity of $Ba_3Ce(PO_4)_3$ at 600 °C was 8.91×10^{-6} S/cm in wet oxygen and 8.78×10^{-6} S/cm in dry oxygen. The total conductivity does not change much in the wet oxygen atmosphere. The activation energy in the dry and wet oxygen was 0.781 and 0.776 eV, respectively. The conductivities of $Ba_3Ce(PO_4)_3$ at 600 °C in the dry and wet nitrogen were 7.05×10^{-6} and 7.67×10^{-6} S/cm, respectively. The activation energies were 0.80 and 0.829 eV in the dry and wet nitrogen, respectively. The conductivities of $Ba_3Ce(PO_4)_3$ at 600 °C in dry and wet 4vol% hydrogen were 4.04×10^{-5} and 1.46×10^{-4} S/cm,

respectively. The activation energies were 0.932 and 0.815 eV in the dry and wet hydrogen, respectively. This is the first time that proton conductivities were studied in the low oxygen partial pressure region, especially in the hydrogen atmosphere.

Figure 5-7 compares the conductivity of $Ba_3Ce(PO_4)_3$ with other phosphates in the wet air and oxygen atmospheres. The conductivity of $Ba_3Ce(PO_4)_3$ was 8.91×10^{-6} S/cm at 600 °C in wet oxygen. The conductivities of un-doped $LaPO_4$ and YPO_4 were 8×10^{-7} S/cm and 1.26×10^{-6} S/cm at 600 °C in wet oxygen, respectively. The conductivity of 5 mol% Sr doped $LaPO_4$ was 1.5×10^{-5} S/cm at 600 °C in wet oxygen. Therefore, the conductivity of $Ba_3Ce(PO_4)_3$ is higher than un-doped $LaPO_4$ and YPO_4 but lower than 5 mol% Sr doped $LaPO_4$.

For Sr doped $LaPO_4$, both electrons and dopant can charge balance oxygen vacancies, holes and possible protons. The electroneutrality condition can be written as

$$[(HPO_4)_{PO_4}]+2[(P_2O_7)^{\cdot\cdot}_{2PO_4}]+p=[Sr'_{La}]+n.$$

For un-doped phosphates, the electrons are the only negative defects to charge balance oxygen vacancies, holes and possible proton. The electroneutrality condition can be written as

$$[(HPO_4)_{PO_4}]+2[(P_2O_7)^{\cdot\cdot}_{2PO_4}]+p=n.$$

The proton concentration increases in doped or un-doped phosphates in the presence of free hydrogen or water vapor; however, the positive defect concentration needs to equal the sum of the electron concentration and the dopant concentration in the doped phosphate while it is equal to the electron concentration alone in the un-doped

phosphate. The result is a total conductivity, which is much higher in doped phosphates than un-doped ones due to dopant effects.

In the future, $Ba_3Ce(PO_4)_3$ will be doped at Ce site with divalent elements and its conductivity behavior will be studied. Higher conductivity is expected in the doped $Ba_3Ce(PO_4)_3$.

5.3.2.2 Conductivity as a function of oxygen partial pressure

The defect structure model in chapter 4 derived the relationship between the charge carrier concentration of $Ba_3Ce(PO_4)_3$ and oxygen partial pressure. To test the proposed defect structure, the conductivity of $Ba_3Ce(PO_4)_3$ was measured as a function of oxygen partial pressure.

It should be pointed out that the conductivity is not only related to charge carrier concentration but also related to carrier mobility; thus, the conductivity dependence of oxygen partial pressure can only approximately reflect the charge carrier concentration dependence of oxygen partial pressure.

Figure 5-8 shows the conductivity of $Ba_3Ce(PO_4)_3$ as a function of oxygen partial pressure at 600 ℃ and 550 ℃. The figure clearly demonstrates the total conductivity dependence in the whole oxygen partial pressure region. Oxygen partial pressure range is divided into four regions: high (1~0.21atm, IV), intermediate ($0.21\sim10^{-7}$atm, III), low-intermediate ($10^{-7}\sim10^{-15}$atm, II) and low ($10^{-15}\sim10^{-25}$atm, I). The conductivity dependences of oxygen partial pressure in these regions of figure 5-8 are shown in figure 5-9 to 5-15. They were compared with defect concentration dependences of oxygen partial pressure, which was derived from the defect structure model. The results are shown in table 5-2.

Low Oxygen Partial Pressure Region (P_{O2}= 10^{-15}~10^{-25} atm)

Four cases were discussed in the proposed defect structure model. Case 1 is the low water partial pressure condition without free hydrogen, case 2 is the low water partial pressure condition with free hydrogen, case 3 is the high water partial pressure condition without free hydrogen, and case 4 is the high water partial pressure condition with free hydrogen.

Case 3, however, could not be studied experimentally in this work due to equipment limitation. The proposed defect structure model is only tested in cases 1, 2 and 4.

Case 1: low water partial pressure condition without free hydrogen

When an oxygen partial pressure is obtained by purifying dry argon gas, it corresponds to the low water vapor partial pressure condition without the existence of free hydrogen. The experimentally obtained oxygen partial pressure range is 10^{-20}~10^{-17} atm.

According to the proposed defect structure model, oxygen vacancies are the only significant positive defects to charge balance electrons. The oxygen vacancy formation can be expresses as the following defect equilibrium:

$$2(PO_4)^{x}_{PO_4} \rightarrow (P_2O_7)^{\cdot\cdot}_{2PO_4} + 2e' + \frac{1}{2}O_2 . \qquad \text{K1} \qquad (4\text{-}1)$$

The electroneutrality condition is simplified as

$$2[(P_2O_7)^{\cdot\cdot}_{2PO_4}] = n .$$

$$K_1 = [n/2]n^2 p_{O_2}^{\frac{1}{2}}$$

Electron concentration and oxygen vacancy concentration are derived to be proportional to $p_{O_2}^{-\frac{1}{6}}$. The experimentally obtained total conductivity is proportional to $p_{O_2}^{-\frac{1}{7}}$ at 600ºC, $p_{O_2}^{-\frac{1}{6}}$ at 550ºC and $p_{O_2}^{-\frac{1}{5}}$ at 500ºC, which is shown in figure 5-9. Therefore, the conductivity dependency of oxygen partial pressure supports the proposed defect structure under low water partial pressure condition without free hydrogen.

Case 2: low water partial pressure condition with free hydrogen

When an oxygen partial pressure is obtained by mixing dry hydrogen and dry argon, it corresponds to the low water vapor partial pressure condition with free hydrogen. The experimentally obtained oxygen partial pressure range is 10^{-26}~10^{-19} atm.

Defect equilibrium under this condition can be written as

$$(PO_4)_{PO_4}^x + \frac{1}{2}H_2 \rightarrow (HPO_4)_{PO_4}^{\cdot} + e' \qquad \text{K3} \qquad (4\text{-}3)$$

There exists small amount of water vapor due to the existence of hydrogen and oxygen formed in formula (4-1):

$$H_2 + \frac{1}{2}O_2 \rightarrow H_2O \qquad \text{K4} \qquad (4\text{-}4)$$

$$K_4 = p_{H_2O} p_{H_2}^{-1} p_{O_2}^{-\frac{1}{2}}.$$

Oxygen vacancies and inserted protons are the positive species in the lattice. The electroneutrality condition is written as

$$[(HPO_4)_{PO_4}^{\cdot}] + 2[(P_2O_7)_{PO_4}^{\cdot}] = n.$$

If oxygen vacancies dominate, then,

$$2[(P_2O_7)_{PO_4}^{\cdot}] = n$$

$$2K_1 p_{O_2}^{-\frac{1}{2}} = n^3.$$

Electron and oxygen concentration are derived to be proportional to $p_{O_2}^{-\frac{1}{6}}$.

If proton concentration dominates, then,

$$[(HPO_4)_{PO_4}] = n$$

$$K_3 K_4^{-\frac{1}{2}} p_{H_2O}^{\frac{1}{2}} p_{O_2}^{-\frac{1}{4}} = n^2$$

Electron and proton concentration are derived to be proportional to $p_{O_2}^{-\frac{1}{8}} p_{H_2O}^{\frac{1}{4}}$. Water partial pressure is low and can be considered as constant in case 2; therefore, the electron and proton concentration are most likely to be proportional to $p_{O_2}^{-\frac{1}{8}}$.

As we mentioned, case 2 was obtained experimentally by mixture of dry argon and dry hydrogen. Lower oxygen partial pressure is obtained by increasing hydrogen concentration in the gas mixture, which provides more proton sources at the same time. Therefore, more protons are incorporated into the lattice and proton concentration gradually becomes dominant when oxygen partial pressure becomes lower in case 2. According to the proposed defect structure, electron and proton concentration are proportional to $p_{O_2}^{-\frac{1}{8}}$ when proton concentration dominates, which is smaller than $p_{O_2}^{-\frac{1}{6}}$ when oxygen vacancy concentration dominates.

The experimentally obtained conductivity is initially proportional to $p_{O_2}^{-\frac{1}{6}}$ and conductivity dependence decreases when oxygen partial pressure becomes lower, which

is shown in figure 5-10 and may indicate the transition from oxygen vacancy dominance to proton dominance.

Therefore, the conductivity behavior of $Ba_3Ce(PO_4)_3$ is considered as a support to the proposed defect structure under low water partial pressure condition with free hydrogen.

Case 4: high water partial pressure condition with free hydrogen

When oxygen partial pressure range 10^{-15}~10^{-25} atm is obtained by flowing a mixture of hydrogen and argon through water, it corresponds to the high water partial pressure condition with free hydrogen.

The corresponding defect equilibriums can be written as

$$(PO_4)^x_{PO_4} + \frac{1}{2}H_2 \rightarrow (HPO_4)^{\cdot}_{PO_4} + e^{'} \qquad \text{K3} \qquad (4\text{-}3)$$

$$2(PO_4)^x_{PO_4} + H_2O \rightarrow 2(HPO_4)_{PO_4} + 2e^{'} + \frac{1}{2}O_2 . \qquad \text{K6} \qquad (4\text{-}6)$$

The electroneutrality condition can be written as

$$[(HPO_4)^{\cdot}_{PO_4}] + 2[(P_2O_7)^{\cdot\cdot}_{2PO_4}] = n .$$

With free hydrogen and water vapor contribution, proton concentration is expected to be dominant. The electroneutrality condition is simplified as

$$[(HPO_4)^{\cdot}_{PO_4}] = n .$$

$$K_3 K_4^{-\frac{1}{2}} p_{H_2O}^{\frac{1}{2}} p_{O_2}^{-\frac{1}{4}} = K_3 p_{H_2}^{\frac{1}{2}} = n^2$$

Proton and electron concentration are derived to be proportional to $p_{O_2}^{-\frac{1}{8}} p_{H_2O}^{\frac{1}{4}}$. They are proportional to $p_{O_2}^{-\frac{1}{8}}$ if water vapor is kept constant. The obtained conductivity

dependence of oxygen partial pressure is $p_{O_2}^{0.004}$ (shown in figure 5-11), which is almost negligible when oxygen partial pressure decreased below 10^{-15} atm.

Oxygen partial pressure change is very small in the low oxygen partial pressure region and water partial pressure may play a more important role. The water partial pressure was held constant in the experiment; therefore, $p_{O_2}^{-\frac{1}{8}} p_{H_2O}^{\frac{1}{4}}$ did not change much. It is difficult to tell whether or not the conductivity behavior in case 4 supports the defect structure model in the corresponding region.

Low-Intermediate Oxygen Partial Pressure Region (P_{O2}= 10^{-7}~10^{-15} atm)

In the proposed defect structure model, cases 1, 3 and 4 were discussed in the low-intermediate oxygen partial pressure region. Due to the equipment limitation, only cases 3 and 4 were tested in this work. Case 3 is the high water partial pressure condition without free hydrogen and case 4 is the high partial pressure condition with free hydrogen.

Case 3: high water partial pressure condition without free hydrogen

When an oxygen partial pressure is obtained by flowing purified argon through water, it corresponds to the high water vapor partial pressure condition without free hydrogen. The experimentally obtained oxygen partial pressure range is 10^{-14}~10^{-11} atm.

Defect equilibrium is written as

$$2(PO_4)_{PO_4}^{x} + H_2O \rightarrow 2(HPO_4)_{PO_4}^{\cdot} + 2e' + \frac{1}{2}O_2 . \qquad \text{K6} \qquad (4\text{-}6)$$

The electroneutrality condition is written as

$$[(HPO_4)_{PO_4}^{\cdot}] + 2[(P_2O_7)_{2PO_4}^{\cdot}] = n .$$

If oxygen vacancy concentration dominates, electroneutrality condition is simplified as

$$2[(P_2O_7)_{2PO_4}^{\cdot}] = n.$$

$$2K_1 p_{O_2}^{-\frac{1}{2}} = 2K_1 K_4 p_{H_2O}^{-1} p_{H_2} = n^3$$

Electron concentration and oxygen vacancy concentration are derived to be proportional to $p_{o_2}^{-\frac{1}{6}}$.

If proton concentration dominates, the electroneutrality condition is written as

$$[(HPO_4)_{PO_4}^{\cdot}] = n.$$

$$K_3 K_4^{-\frac{1}{2}} p_{H_2O}^{\frac{1}{2}} p_{O_2}^{-\frac{1}{4}} = n^2$$

Proton and electron concentration are derived to be proportional to $p_{o_2}^{-\frac{1}{8}} p_{H_2O}^{\frac{1}{4}}$.

Only three conductivity data points were obtained due to the equipment limitations. The conductivity dependency of oxygen partial pressure was obtained by extending the data trend to oxygen partial pressure $p_{o_2} = 10^{-7}$ atm. The conductivity data trend shows a $p_{O_2}^{-\frac{1}{7}}$ dependence at 600ºC and a $p_{O_2}^{-\frac{1}{6}}$ dependence at 550 and 500ºC, which is shown in figure 5-12. We could not tell whether or not the conductivity dependency of oxygen partial pressure supports the proposed defect structure under this condition due to the limited data.

Case 4: high water partial pressure condition with free hydrogen

When an oxygen partial pressure range at 10^{-15}~10^{-7} atm is obtained by flowing a mixture of hydrogen and argon through water, it corresponds to the high water vapor

partial pressure condition with free hydrogen. The corresponding defect equilibriums are written as

$$(PO_4)^x_{PO_4} + \frac{1}{2}H_2 \rightarrow (HPO_4)^{\cdot}_{PO_4} + e' \qquad \text{K3} \qquad (4\text{-}3)$$

$$2(PO_4)^x_{PO_4} + H_2O \rightarrow 2(HPO_4)^{\cdot}_{PO_4} + 2e' + \frac{1}{2}O_2 . \qquad \text{K6} \qquad (4\text{-}6)$$

The electroneutrality condition can be written as:

$$[(HPO_4)^{\cdot}_{PO_4}] + 2[(P_2O_7)^{\cdot\cdot}_{2PO_4}] = n .$$

A small trace of free hydrogen in the gas mixture decreases oxygen partial pressure a lot. Therefore, the free hydrogen concentration is not high at the low-intermediate oxygen partial pressure region and its contribution to the proton incorporation can be omitted compared with water vapor contribution. All the derivations in case 3 also approximately apply in case 4.

If oxygen vacancy concentration dominates, electron concentration and oxygen vacancy concentration will be proportional to $p_{o_2}^{-\frac{1}{6}}$. If proton concentration dominates, the proton and electron concentration will be proportional to $p_{o_2}^{-\frac{1}{8}} p_{H_2O}^{\frac{1}{4}}$.

The experimentally obtained conductivity is proportional to $p_{o_2}^{-\frac{1}{6}}$, which is shown in figure 5-13 and may suggest that oxygen vacancy dominates in this region. This also suggests that the conductivity dependence of oxygen partial pressure in case 4 supports the proposed defect structure model in the low-intermediate oxygen partial pressure region.

Intermediate Oxygen Partial Pressure Region ($P_{O2} = 0.21 \sim 10^{-7}$ atm)

Intermediate oxygen partial pressure range ($10^{-7} \sim 10^{-1}$ atm) was obtained by using an oxygen pump (SGM5EL) with dry or wet argon gas.

The defect equilibriums can be written as

$$2(PO_4)_{PO4}^{x} \rightarrow (P_2O_7)_{2PO_4}^{\cdot\cdot} + \frac{1}{2}O_2 + 2e^{'} \qquad \text{K1} \qquad (4\text{-}1)$$

$$2(PO_4)_{PO_4}^{x} + H_2O \rightarrow 2(HPO_4)_{PO_4} + 2e^{'} + \frac{1}{2}O_2 . \qquad \text{K6} \qquad (4\text{-}6)$$

The corresponding electroneutrality condition under dry atmosphere is written as

$$2[(P_2O_7)_{2PO_4}^{\cdot\cdot}] + p = n .$$

The corresponding electroneutrality condition under wet atmosphere is written as

$$[(HPO_4)_{PO_4}^{\cdot}] + 2[(P_2O_7)_{2PO_4}^{\cdot\cdot}] + p = n .$$

Despite the fact that the electron, hole and oxygen vacancy concentrations usually are not high due to the phosphate structure and the intermediate oxygen partial pressure; they could not be omitted. Electron concentration almost equals hole concentration, restricting proton concentration based on the electroneutrality condition. The oxygen vacancy concentration is also low in this region. In the intermediate oxygen partial pressure region, the total defect concentration is expected to be low. No apparent oxygen partial pressure or water partial pressure dependency is expected under this condition.

The experimentally obtained conductivity in this region is low and independent of oxygen partial pressure, which is shown in figure 5-14. The conductivity dependence is just as the defect structure model predicted. The conductivity behavior supports the proposed model in the intermediate oxygen partial pressure region.

High Oxygen Partial Pressure Region (P_{O_2} = 0.21~1 atm)

High oxygen partial pressure range (0.21~1atm) was obtained by using a mixture of argon and oxygen gas.

The following defect equilibriums exist in the high oxygen partial pressure region:

$$2(PO_4)^x_{PO_4} \rightarrow (P_2O_7)^{\cdot\cdot}_{2PO_4} + 2e' + \frac{1}{2}O_2 . \qquad \text{K1} \qquad (4\text{-}1)$$

$$2(PO_4)^x_{PO_4} + H_2O \rightarrow 2(HPO_4)^{\cdot}_{PO_4} + 2e' + \frac{1}{2}O_2 . \qquad \text{K6} \qquad (4\text{-}6)$$

The electroneutrality condition under dry atmosphere can be written as

$$2[(P_2O_7)^{\cdot\cdot}_{2PO_4}] + p = n .$$

The electroneutrality condition under wet atmosphere can be written as

$$[(HPO_4)^{\cdot}_{PO_4}] + 2[(P_2O_7)^{\cdot\cdot}_{2PO_4}] + p = n .$$

As we pointed out in chapter 4, the above electroneutrality conditions face a challenge: Electrons are the only negative defects to charge balance holes, oxygen vacancies and possible protons; however, electron concentration is usually lower than hole concentration in the high oxygen partial pressure region. Extra negative defects are needed to charge balance holes. The defect concentration dependencies of oxygen partial pressure were not derived.

Figure 5-15 shows the conductivity of $Ba_3Ce(PO_4)_3$ as a function of oxygen partial pressure in the oxygen partial pressure region 0.21~1 atm. The conductivity increases slightly with increasing oxygen partial pressure, suggesting p-type electronic conduction. The conductivity of $Ba_3Ce(PO_4)_3$ is slightly higher in a wet atmosphere than in a dry atmosphere, indicating the existence of proton conduction. In the presence of water vapor, equal amounts of protons and electrons were incorporated into the lattice.

The electron concentration restricts the proton concentration. The result is that the total concentration increases slightly.

Based on the conductivity data of $Ba_3Ce(PO_4)_3$, it is still unclear which extra negative defect is charge balancing the holes.

5.3.2.3 Conductivity as a function of water vapor partial pressure

Conductivity dependence of water vapor partial pressure was not studied in the low-intermediate oxygen partial pressure region due to equipment limitation. It was also not studied in the high oxygen partial pressure region due to the challenge we mentioned before.

Conductivity dependence of water vapor partial pressure was only studied in the low and intermediate oxygen partial pressure regions. The results are listed in table (5-3) and compared with defect concentration dependence.

Low Oxygen Partial Pressure Region

Wet 40vol% hydrogen belongs to case 4 in the low oxygen partial pressure region. Proton concentration dominates in wet 40vol% hydrogen. Proton concentration and electron concentration are derived to be proportional to $p_{O_2}^{-\frac{1}{8}} p_{H_2O}^{\frac{1}{4}}$ based on the proposed defect structure model. When water partial pressure is changed in 40vol% hydrogen, oxygen partial pressure changes slightly. If oxygen partial pressure change is omitted, the proton concentration and electron concentration is proportional to $p_{H_2O}^{\frac{1}{4}}$.

Figure 5-16 shows conductivity of $Ba_3Ce(PO_4)_3$ as a function of water partial pressure in 40vol% hydrogen in the temperature range of 500-600 °C. The conductivity of $Ba_3Ce(PO_4)_3$ is proportional to $p_{H_2O}^{\frac{1}{5}}$ at 550°C and $p_{H_2O}^{\frac{1}{5.8}}$ at 600°C. The

experimentally obtained conductivity dependence of water partial pressure is smaller than the defect concentration dependence in the proposed model.

It was pointed out at the beginning of chapter 5.3.2.2 that the conductivity is not only related to charge carrier concentration but also related to carrier mobility. Thus, take into account of mobility effect, this conductivity dependence of water vapor partial pressure still approximately reflects the defect concentration dependence of water vapor partial pressure in the low oxygen partial pressure region.

Intermediate Oxygen Partial Pressure Region:

A nitrogen atmosphere lies within the intermediate oxygen partial pressure region. Since electrons are present in minor concentration, the proton concentration is expected to be low and will not increase much in the presence of water vapor due to the electroneutrality restriction. The water vapor effect on defect concentration will not be apparent.

Figure 5-17 shows the conductivity of $Ba_3Ce(PO_4)_3$ as function of water partial pressure in the temperature range of 500-600 °C for a nitrogen atmosphere. The experimentally obtained conductivity is approximately proportional to $p_{H_2O}^{0.04}$ at 500 °C, which is negligible compared with that in wet hydrogen. The conductivity behavior of $Ba_3Ce(PO_4)_3$ as a function of water partial pressure supports the proposed defect structure in the intermediate oxygen partial pressure region.

5.3.2.4 Conductivity as a function of hydrogen partial pressure

Conductivity dependence of hydrogen partial pressure was studied only in the low oxygen partial pressure regions. The result is listed in table (5-4) and compared with defect concentration dependency.

Figure 5-18 shows the conductivity of $Ba_3Ce(PO_4)_3$ as a function of hydrogen partial pressure at 550~600 °C with p_{H_2O}=0.0312 atm. Wet hydrogen belongs to case 4 in the low oxygen partial pressure region. Proton concentration dominates in wet hydrogen. Proton concentration and electron concentration are derived to be proportional to $p_{H_2}^{\frac{1}{4}}$. The experimentally obtained conductivity is proportional to $p_{H_2}^{\frac{1}{12}}$ at 600°C, much smaller than the derived $p_{H_2}^{\frac{1}{4}}$ from the model.

One possible explanation for this discrepancy is the proton saturation in the lattice. No more protons can be incorporated into the lattice after the solubility limit is reached. The other possibility is that electron-proton associations are formed at the high proton concentration, without making a contribution to conduction. The association reaction can be written as

$$(HPO_4)_{PO_4} + e^{'} \rightarrow ((HPO_4)_{PO_4} e^{'})^{\times}.$$

Therefore, the conductivity dependence of hydrogen partial pressure is lower than the model predicted one.

5.3.2.5 Conductivity under CO/CO_2 mixture gas

During conductivity dependency studies, many gas mixtures were tried to obtain the required oxygen partial pressure. We find that the same oxygen partial pressure region 10^{-14}~10^{-19}atm can be obtained either by a CO/CO_2 gas mixture or by a purified argon gas. Figure 5-19 demonstrates the conductivity results of $Ba_3Ce(PO_4)_3$ in the above two gases in the same oxygen partial pressure region. Conductivity in CO/CO_2 mixture gas is lower when oxygen partial pressure is less than 10^{-15}atm. It suggests that

either CO/CO_2 does not come to equilibrium or the CO/CO_2 gas mixture lowers the conductivity of $Ba_3Ce(PO_4)_3$ when the oxygen partial pressure is less than 10^{-15}atm.

5.4 Conclusion

The relative density of $Ba_3Ce(PO_4)_3$ increased with sintering temperature, from 78% at 1100 °C, to 89% at 1200 °C, to 95% at 1300 °C. However, impurity phase $Ba_2P_2O_7$ was produced with a sintering temperature of 1300 °C for 8 h or with a sintering temperature of 1200 °C for 24 h.

The conductivity of $Ba_3Ce(PO_4)_3$ is 8.91×10^{-6} S/cm at 600 °C in wet oxygen, which is higher than undoped $LaPO_4$ and YPO_4 but lower than 5 mol% Sr doped $LaPO_4$. The conductivities of $Ba_3Ce(PO_4)_3$ at 600 °C in dry and wet 4vol% hydrogen are 4.04×10^{-5} and 1.46×10^{-4} S/cm, respectively. This is the first time that proton conductivities were studied in the low oxygen partial pressure region, especially in a hydrogen atmosphere. However, the total conductivity of $Ba_3Ce(PO_4)_3$ is not as good as that of perovskite in the measured temperature region, which is usually 10^{-2}-10^{-3} S/cm at 600 °C.

The $Ba_3Ce(PO_4)_3$ conductivity dependence of oxygen partial pressure and water partial pressure data supported the proposed defect structure.

In the future, $Ba_3Ce(PO_4)_3$ will be doped at Ce site with divalent elements and its conductivity behavior will be studied. Higher conductivity will be expected in the doped $Ba_3Ce(PO_4)_3$.

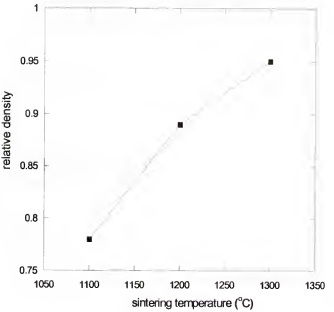

Figure 5-1. Relative density with different sintering temperatures for 8h.

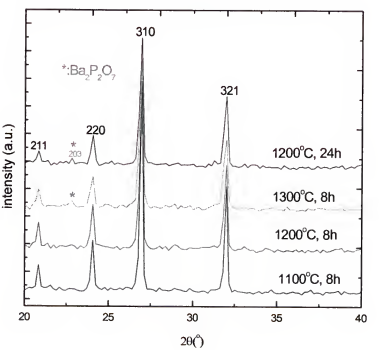

Figure 5-2. XRD of $Ba_3Ce(PO_4)_3$ with different sintering temperatures and dwell times.

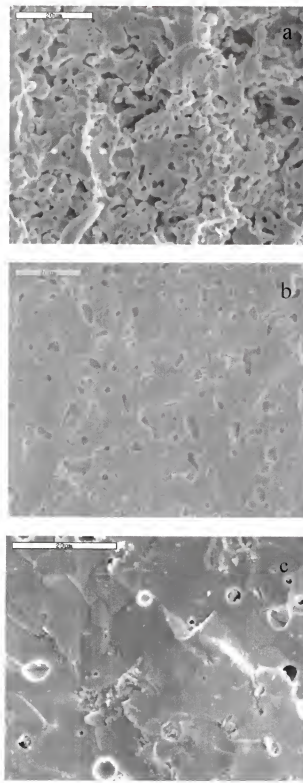

Figure 5-3. SEM images of fracture cross sections of $Ba_3Ce(PO_4)_3$ pellets with a dwell time of 8 h and different sintering temperatures. (a) 1100 °C, (b) 1200 °C and (c) 1300 °C.

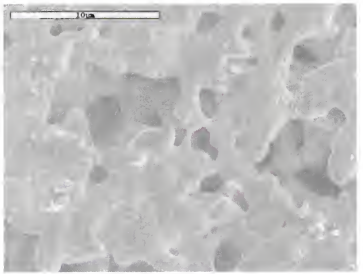

Figure 5-4. Porous Pt electrode on the surface of a $Ba_3Ce(PO_4)_3$ pellet.

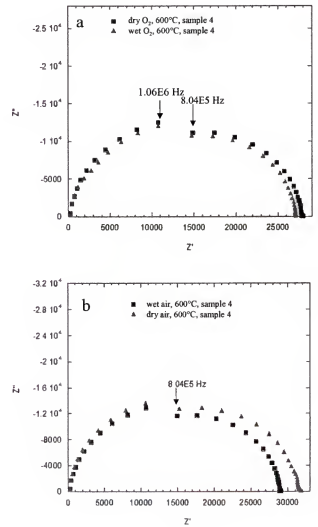

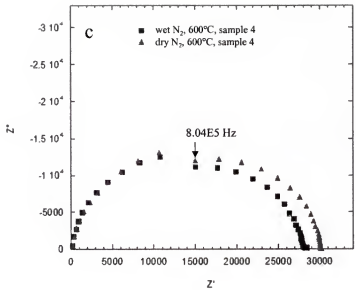
c
wet N2, 600°C, sample 4
dry N2, 600°C, sample 4
8.04E5 Hz
-Z''
Z'
-3 10^4
-2.5 10^4
-2 10^4
-1.5 10^4
-1 10^4
-5000
0
0
5000
10000
15000
20000
25000
30000

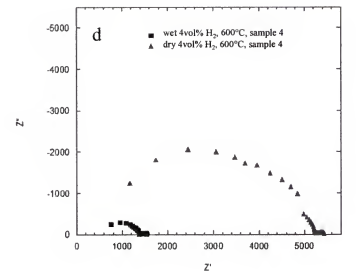
d
wet 4vol% H2, 600°C, sample 4
dry 4vol% H2, 600°C, sample 4
-Z''
Z'
-5000
-4000
-3000
-2000
-1000
0
0
1000
2000
3000
4000
5000

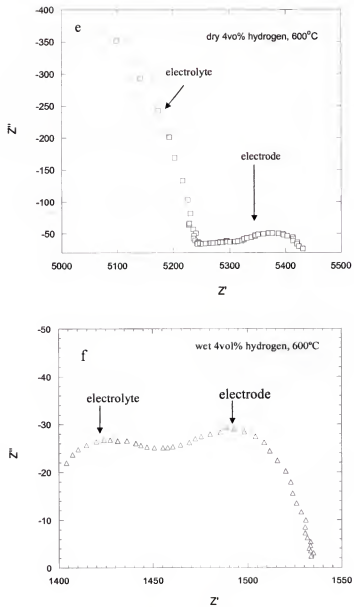

Figure 5-5. Impedance plot of $Ba_3Ce(PO_4)_3$ in different atmospheres. (a-d) is the impedance plot of $Ba_3Ce(PO_4)_3$ in oxygen, air, nitrogen and 4vol% hydrogen, respectively. (e-f) is the enlarged impedance plot of (d).

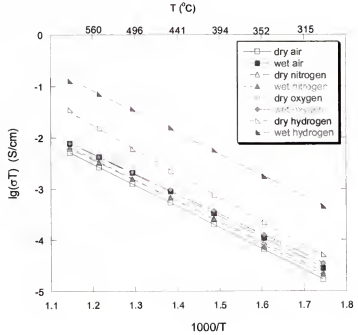

Figure 5-6. Arrhenius Plot of $Ba_3Ce(PO_4)_3$ under different atmospheres.

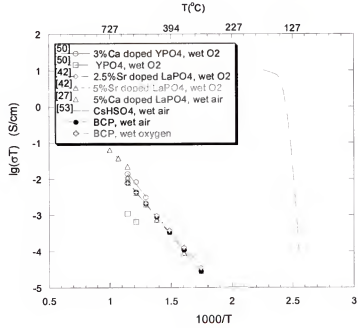

Figure 5-7. Conductivity comparison of $Ba_3Ce(PO_4)_3$ with reported data from literature.

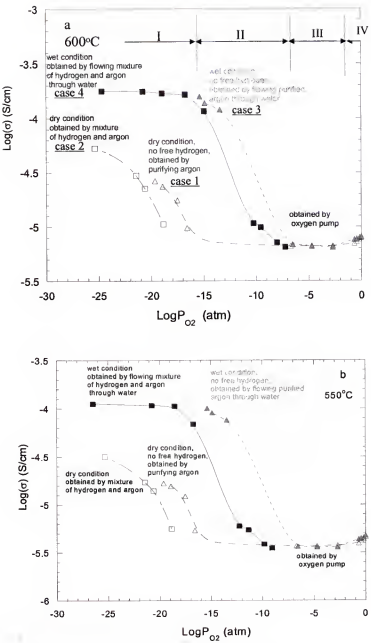

Figure 5-8. Conductivity of $Ba_3Ce(PO_4)_3$ as a function of oxygen partial pressure in the whole oxygen partial pressure region: (a) at 600°C and (b) at 550°C.

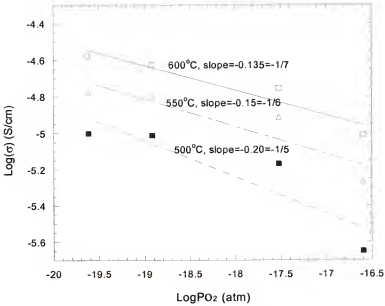

Figure 5-9. Conductivity of $Ba_3Ce(PO_4)_3$ as a function of oxygen partial pressure in the case 1 of low oxygen partial pressure region.

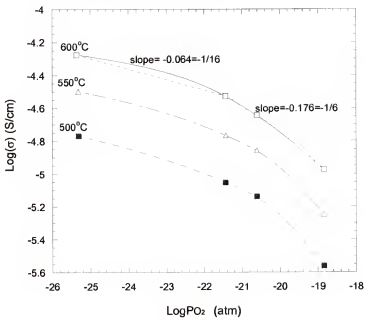

Figure 5-10. Conductivity of $Ba_3Ce(PO_4)_3$ as a function of oxygen partial pressure in the case 2 of low oxygen partial pressure region.

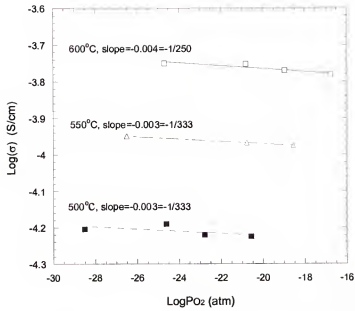

Figure 5-11. Conductivity of $Ba_3Ce(PO_4)_3$ as a function of oxygen partial pressure in the case 4 of low oxygen partial pressure region.

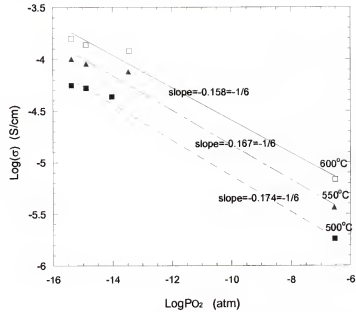

Figure 5-12. Conductivity of $Ba_3Ce(PO_4)_3$ as a function of oxygen partial pressure in the case 3 of low-intermediate oxygen partial pressure region.

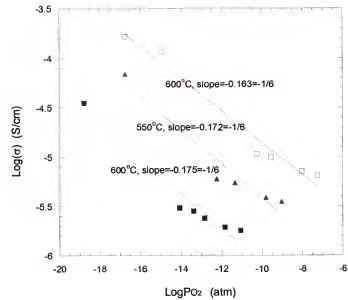

Figure 5-13. Conductivity of $Ba_3Ce(PO_4)_3$ as a function of oxygen partial pressure in the case 4 of low-intermediate oxygen partial pressure region.

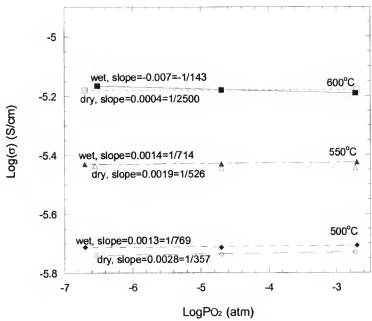

Figure 5-14. Conductivity of $Ba_3Ce(PO_4)_3$ as a function of oxygen partial pressure in the intermediate oxygen partial pressure region.

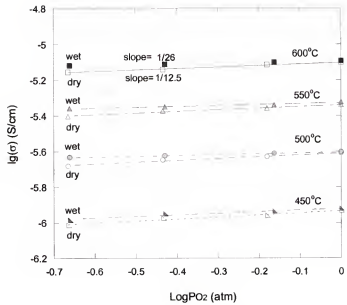

Figure 5-15. Conductivity of $Ba_3Ce(PO_4)_3$ as a function of oxygen partial pressure in the high oxygen partial pressure region.

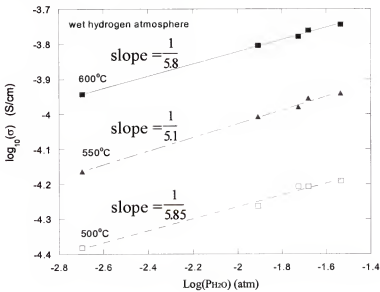

Figure 5-16. Conductivity of $Ba_3Ce(PO_4)_3$ as a function of water partial pressure in hydrogen.

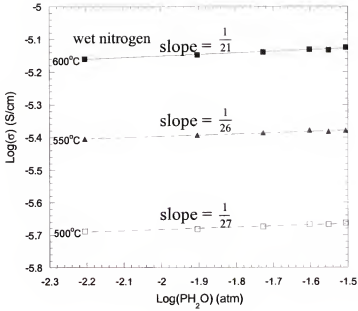

Figure 5-17. Conductivity of $Ba_3Ce(PO_4)_3$ as a function of water partial pressure in nitrogen.

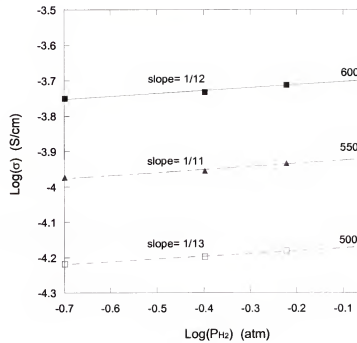

Figure 5-18. Conductivity of $Ba_3Ce(PO_4)_3$ as function of hydrogen concentration with p_{H_2O}=0.0312atm.

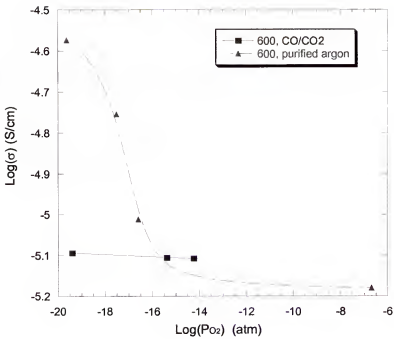

Figure 5-19. Conductivity of $Ba_3Ce(PO_4)_3$ under the CO/CO_2 gas mixture compared with that under purified argon gas.

Table 5-1. Electrical conductivity data of $Ba_3Ce(PO_4)_3$ under different atmospheres.

	σ_0	E_a (eV)	$\sigma_{600°C}$	$\sigma_{550°C}$
dry air	2.8747E2	0.821	5.8E-6	3.24E-6
wet air	3.9546E2	0.810	8.93E-6	5.17E-6
dry nitrogen	2.6224E2	0.800	7.05E-6	3.99E-6
wet nitrogen	4.1068E2	0.829	7.67E-6	4.08E-6
dry oxygen	2.6020E2	0.781	8.78E-6	5.08E-6
wet oxygen	2.4434E2	0.776	8.91E-6	5.13E-6
dry 4vol% H_2	7.7983E3	0.932	4.04E-5	1.83E-5
wet 4vol% H_2	7.191E3	0.815	1.46E-4	8.69E-5

Table 5-2. Conductivity dependence of oxygen partial pressure.

Oxygen partial pressure region		Defect concentration dependence	Conductivity dependence
Low p_{O_2} region	Low p_{H_2O} No free H_2	$p_{O_2}^{-\frac{1}{6}}$	$p_{O_2}^{-\frac{1}{6}}$ at 550°C
	Low p_{H_2O} With free H_2	$p_{O_2}^{-\frac{1}{6}}$ if vacancy dominates $p_{O_2}^{-\frac{1}{8}} p_{H_2O}^{\frac{1}{4}}$ if proton dominates	Initially $p_{O_2}^{-\frac{1}{6}}$, then decreases with decreasing p_{O_2}
	High p_{H_2O} No free H_2	$p_{O_2}^{-\frac{1}{6}}$ if vacancy dominates $p_{O_2}^{-\frac{1}{8}} p_{H_2O}^{\frac{1}{4}}$ if proton dominates	Not studied due to equipment limitation
	High p_{H_2O} With free H_2	$p_{O_2}^{-\frac{1}{8}} p_{H_2O}^{\frac{1}{4}}$	negligible
Low-intermediate p_{O_2} region	Low p_{H_2O} No free H_2	$p_{O_2}^{-\frac{1}{6}}$	Not studied due to equipment limitation
	High p_{H_2O} No free H_2	$p_{O_2}^{-\frac{1}{6}}$ if vacancy dominates $p_{O_2}^{-\frac{1}{8}} p_{H_2O}^{\frac{1}{4}}$ if proton dominates	$p_{O_2}^{-\frac{1}{6}}$ at 500 and 550°C, however, not enough data
	High p_{H_2O} With free H_2	$p_{O_2}^{-\frac{1}{6}}$ if vacancy dominates $p_{O_2}^{-\frac{1}{8}} p_{H_2O}^{\frac{1}{4}}$ if proton dominates	$p_{O_2}^{-\frac{1}{6}}$
Intermediate p_{O_2} region		Independent	Independent
High p_{O_2} region		dependence was not derived	

Table 5-3. Conductivity dependency of water partial pressure.

p_{O_2} region		Defect concentration dependence	Conductivity dependence
Low p_{O_2} region	Low p_{H_2O} No free H_2	Not derived due to low water partial pressure	
	Low p_{H_2O} With free H_2		
	High p_{H_2O} No free H_2	$p_{H_2}^{\frac{1}{3}} p_{H_2O}^{\frac{1}{3}}$ if oxygen vacancies dominate; $p_{O_2}^{-\frac{1}{8}} p_{H_2O}^{\frac{1}{4}}$ if protons dominate	Not studied due to experimental condition
	High p_{H_2O} With free H_2	$p_{O_2}^{-\frac{1}{8}} p_{H_2O}^{\frac{1}{4}}$	$p_{H_2O}^{\frac{1}{5.85}}$ (600ºC), $p_{H_2O}^{\frac{1}{5.1}}$ (550ºC)
Low-intermediate p_{O_2} region	Low p_{H_2O} No free H_2	Not derived due to low water partial pressure	
	High p_{H_2O} No free H_2	$p_{O_2}^{-\frac{1}{8}} p_{H_2O}^{\frac{1}{4}} - p_{H_2}^{\frac{1}{3}} p_{H_2O}^{\frac{1}{3}}$	Not studied due to experimental condition
	High p_{H_2O} With free H_2	$p_{O_2}^{-\frac{1}{8}} p_{H_2O}^{\frac{1}{4}} - p_{H_2}^{\frac{1}{3}} p_{H_2O}^{\frac{1}{3}}$	
Intermediate p_{O_2} region		Independent	Independent
High p_{O_2} region		Electroneutrality condition faces a challenge, dependence was not derived	

Table 5-4. Conductivity dependence of hydrogen partial pressure.

Low p_{O_2} region	Defect concentration dependence	Conductivity dependence
Low p_{H_2O}, Without free H_2	Not derived due to no free hydrogen	
Low p_{H_2O}, With free H_2	$p_{H_2}^{\frac{1}{3}} p_{H_2O}^{\frac{1}{3}}$ if oxygen vacancy dominates; $p_{H_2}^{\frac{1}{4}}$ if proton dominates	Not studied
High p_{H_2O}, Without free H_2	Not derived due to no free hydrogen	
High p_{H_2O}, With free H_2	$p_{H_2}^{\frac{1}{4}}$	$p_{H_2}^{\frac{1}{12}}$

CHAPTER 6
TRANSFERENCE NUMBER MEASUREMENT

6.1 Introduction

Chapter 5 presented the measured conductivity of $Ba_3Ce(PO_4)_3$, which includes the contribution from protons, electrons and oxygen vacancies. Information about proton transference number is needed to assess the proton conductivity and to determine if $Ba_3Ce(PO_4)_3$ is a mixed conductor or pure proton conductor. If it is a mixed conductor, hydrogen flux will be measured directly in single phase $Ba_3Ce(PO_4)_3$. If it is a pure proton conductor, it will be mixed with Pd or CeO_2 to form a composite and hydrogen flux through the composite will be measured.

The transference number of $Ba_3Ce(PO_4)_3$ in hydrogen atmosphere was studied by employing the following cells:

II, 100% H_2, Pt/ $Ba_3Ce(PO_4)_3$/Pt, 4% H_2, I (c1)

II, 50% H_2+balance He, Pt/ $Ba_3Ce(PO_4)_3$/Pt, 4% H_2, I (c2)

II, 25% H_2+balance He, Pt/ $Ba_3Ce(PO_4)_3$/Pt, 4% H_2, I (c3)

II, 12.5% H_2+balance He, Pt/ $Ba_3Ce(PO_4)_3$/Pt, 4% H_2, I (c4)

where I and II correspond to the two sides of the cell.

The transference number of $Ba_3Ce(PO_4)_3$ in wet hydrogen atmosphere was studied by flowing hydrogen gases on both sides of the above cells bubbled through water at room temperature.

In a hydrogen partial pressure gradient, the theoretical electromotive force can be expressed as

$$E_{theoretical} = -\frac{RT}{2F} \ln \frac{p_{H_2}^{II}}{p_{H_2}^{I}}. \quad (6\text{-}1)$$

If $Ba_3Ce(PO_4)_3$ is a mixed conductor, the experimental value of the electromotive force will be smaller than the theoretical one.

The experimental electromotive force in a hydrogen partial pressure gradient can be expressed as

$$E_{experimental} = t_{ion} E_{theoretical}. \quad (6\text{-}2)$$

The experimental electromotive force in a hydrogen and water partial pressure gradient can be expressed as

$$E_{experimental} = \frac{RT}{4F}[-t_{ion} \ln \frac{p_{H_2}^{II}}{p_{H_2}^{I}} + t_{V_O^{\cdot\cdot}} \ln \frac{p_{H_2O}^{II}}{p_{H_2O}^{I}}] \text{ [13]} \quad (6\text{-}3)$$

due to the possibility of both proton and oxygen ion conductivity.

To measure the transference number between 300 and 600 °C, a gas tight seal must be formed between the sample and the supporting alumina tube. Rubber O-ring seals can only be used below 400 °C due to their heat resistance limits. Metal ring seals are used at high temperature but their thermal stress during heating or cooling causes sample cracking [80]. Glass-based seals have better spreading properties and thermal compatibility with the ceramic membranes and supporting tube. The sealing material must meet the following requirements [81-82]: (1) it should have good wettability with the membrane and the supporting tube, (2) it should fit and stay in the gap between the membrane and tube at the testing temperature range, (3) it should have no reaction with

the membrane and tube, (4) the thermal expansion coefficient of the seal should be compatible with the membrane. Because of the intermediate temperature range and large thermal expansion coefficient (15×10^{-6}/°C) of $Ba_3Ce(PO_4)_3$, conventional sealants do not work well. The thermal expansion coefficient of SZP-1 glass is in the range 10-12×10^{-6}/°C [83]. In this chapter, it was used to seal $Ba_3Ce(PO_4)_3$ membrane and Al_2O_3 tube.

The transference numbers obtained from the above four cells should be identical at the same temperature if sealant is perfect. If sealant is not good, the true hydrogen concentration on the outlet of gas I (4vol% H_2) will be detected by the mass spectrometer.

6.2 Experiment

The experimental setup for $Ba_3Ce(PO_4)_3$ transference number measurement is illustrated in Figure 6-1. Platinum wire was attached to the sample and carefully connected with electrode leads inside the setup. SZP-1 glass powder was pasted around the sample and tube. The whole setup was heated to 450 °C at 3 °C/min and held for half an hour to seal, followed by a slow heating to the testing temperature. Gas flow rate was controlled at 50 sccm. The open circuit voltage was measured with a Keithley 2000 multimeter. The true hydrogen concentration on the outlet of gas I was monitored by the Q100MS Dycor Quadlink mass spectrometer.

6.3 Results and Discussion

The total ionic transference number of $SrCe_{0.95}Y_{0.05}O_{3-\delta}$ in dry hydrogen concentration cells was considered the proton transference number by Guan [13]. This assumes no oxygen ionic transport and is the approach we are using.

In the proposed defect structure model of $Ba_3Ce(PO_4)_3$, a dry hydrogen atmosphere is considered the low water partial pressure condition with free hydrogen. The defect concentration is derived to be proportional to $p_{O_2}^{-\frac{1}{6}}$ if oxygen vacancy dominates and it is derived to be proportional to $p_{O_2}^{-\frac{1}{8}}$ if proton concentration dominates. The conductivity of $Ba_3Ce(PO_4)_3$ is initially proportional to $p_{O_2}^{-\frac{1}{6}}$ and the conductivity dependence decreases at lower oxygen partial pressure, demonstrating that the proton concentration becomes dominant when oxygen partial pressure decreases. The oxygen partial pressure in the above dry hydrogen concentration cells is around 10^{-24}~10^{-25} atm; therefore, proton concentration dominates in these cells consistent with the assumption $t_{ion} = t_{OH_O}$.

In the proposed defect structure model of $Ba_3Ce(PO_4)_3$, a wet hydrogen atmosphere is considered the high water partial pressure condition with free hydrogen. Both free hydrogen and water vapor make contributions to proton incorporation; therefore, proton concentration dominates. Conductivity of $Ba_3Ce(PO_4)_3$ remains unchanged when oxygen partial pressure is below 10^{-15} atm, which confirms that the proton concentration dominates in wet hydrogen atmosphere.

When proton concentration dominates, the ionic transference number could be considered proton transference number because the mobility of protons is much higher than that of oxygen vacancies. It can be expressed as

$$t_{ion} \approx t_{OH_O} = \frac{\sigma_{OH_O}}{\sigma_{OH_O} + \sigma_{elec}} = \frac{c_{OH_O} e\mu_{OH_O}}{c_{OH_O} e\mu_{OH_O} + c_{e'} e\mu_{e'}}. \quad (6\text{-}4)$$

where c_{OH_O} is the concentration of protons, $c_{e'}$ is the concentration of electrons, μ_{OH_O} is the mobility of protons and $\mu_{e'}$ is the mobility of electrons. The ionic transference number is not only related to the concentration of charge carriers but also related to their mobilities.

Figure 6-2 shows the open circuit voltage of $Ba_3Ce(PO_4)_3$ as a function of hydrogen partial pressure ratio in the dry and wet hydrogen concentration cells at 600 and 550 °C. The proton transference number is 0.53 in cell 4 under dry hydrogen and 0.52 under wet hydrogen at 600 °C. Figure 6-2, however, also shows that the proton transference number increased with decreasing hydrogen partial pressure ratio, indicating the SZP-1 glass sealant is not perfect. In order to eliminate the leakage effect, the true hydrogen concentration on the outlet of gas I was monitored by mass spectrometer.

Figure 6-3 is the calibration curve of the mass spectrometer. In the calibration, hydrogen gases with different concentrations were fed into the mass spectrometer to achieve the corresponding hydrogen partial pressures. Hydrogen partial pressure as a function of concentration was plotted. The true hydrogen concentration in gas I outlet during the experiment can be obtained from its partial pressure in figure 6-3.

The true hydrogen concentrations in the gas I outlet for the four cells are listed in table 6-1. The values are higher than the applied concentrations and increase with increasing hydrogen partial pressure on the side II, indicating either hydrogen permeation or the existence of a leakage. Argon gas is detected on side II by the mass spectrometer when it is fed on the side I, indicating the existence of a leakage. The true theoretical electromotive forces were obtained by using formula (6-1) and the true hydrogen

concentration ratio. The measured voltages in the hydrogen cells are also listed in table 6-1.

Figure 6-4 shows the open circuit voltage of $Ba_3Ce(PO_4)_3$ in dry hydrogen concentration cells at 600°C after concentration correction. With mass spectrometer correction, the proton transference number showed no apparent dependence on the hydrogen partial pressure ratio. For cell 1, the proton transference number is 0.77 in dry hydrogen at 600°C. The proton transference number studies in wet hydrogen concentration cells are more complex due to the hydrogen and water partial pressure effect. No further calibration or analysis was done in wet hydrogen concentration cells.

Hydrogen concentration cell 1 was also used to investigate the relationship between proton transference numbers and temperature. The true hydrogen concentration on the gas I outlet in cell 1 remains 15.4% at 500-600°C. The corresponding theoretical and experimental electromotive forces are listed in table 6-2. Figure 6-5 shows the proton transference number of $Ba_3Ce(PO_4)_3$ in the dry hydrogen atmosphere as a function of temperature. The proton transference number remains 0.79 from 500 °C to 550 °C.

The proton transference number should have no relationship with hydrogen partial pressure ratio. Cells 1-4 correspond to the same oxygen partial pressure region. Therefore, proton transference number is the same in these cells. No further analysis of proton transference as a function of temperature was done on the cells 2-4.

The conclusion drawn from this data is that $Ba_3Ce(PO_4)_3$ is a mixed conductor with dominant proton conduction. The proton conductivity is approximately 3.23×10^{-5} S/cm at 600 °C in dry hydrogen atmosphere.

6.4 Conclusion

$Ba_3Ce(PO_4)_3$ is a mixed conductor with dominant proton conduction. The proton transference number and electronic transference number are around 0.8 and 0.2, respectively, at 600 °C in the dry hydrogen concentration cells. Therefore, the proton conductivity of $Ba_3Ce(PO_4)_3$ is around 3.23×10^{-5} S/cm at 600 °C in dry hydrogen atmosphere and electron conductivity is 8.1×10^{-6} S/cm.

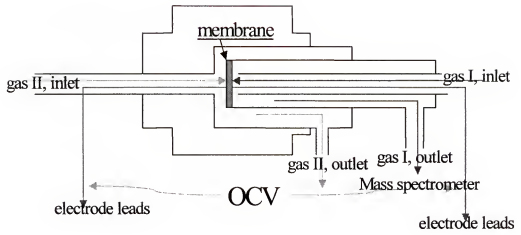

Figure 6-1. Schematic illustration of the experimental setup for transference number measurement.

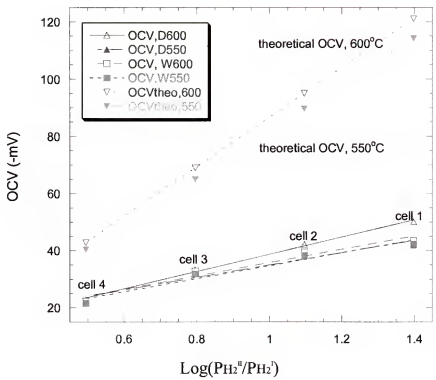

Figure 6-2. Open circuit voltage of $Ba_3Ce(PO_4)_3$ as a function of Log($P_{H_2}^{II}/P_{H_2}^{I}$) in the wet and dry concentration cells at 600 and 550°C.

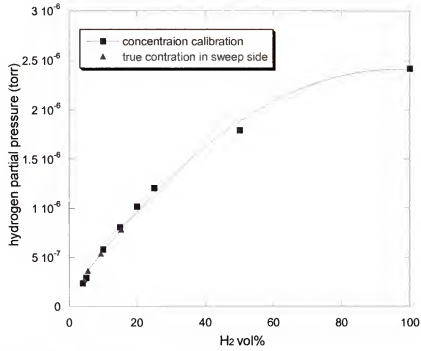

Figure 6-3. Hydrogen concentration calibration of the mass spectrometer.

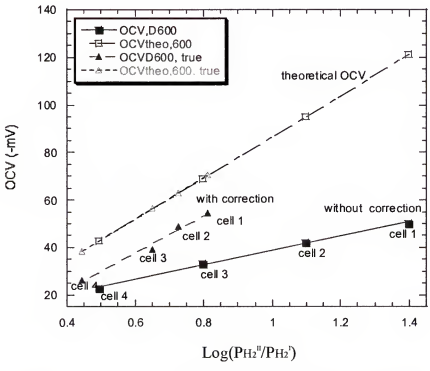

Figure 6-4. Open circuit voltage of $Ba_3Ce(PO_4)_3$ as a function of Log(P_{H2}^{II}/P_{H2}^{I}) with or without MS correction in dry concentration cells at 600ºC.

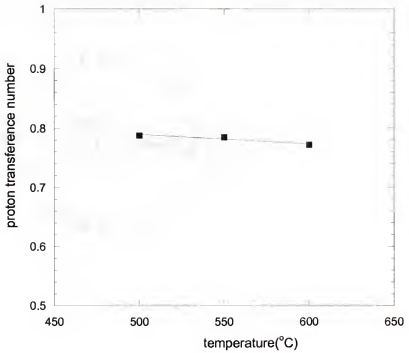

Figure 6-5. Proton transference number as a function of temperature in the dry hydrogen atmosphere.

Table 6-1. Corrected hydrogen concentration in cell 1-cell4.

cell	applied hydrogen concentration of gas I	true hydrogen concentration of gas I	600°C	
			dry H_2 cell $E_{measurement}$ (mV)	true $E_{theoretical}$ (mV)
1	4vol%	15.4vol%	-54.30	-70.36
2	4vol%	9.4vol%	-48.62	-62.86
3	4vol%	5.6vol%	-39.28	-56.27
4	4vol%	4.5vol%	-26.67	-38.43

Table 6-2. Proton transference number of $Ba_3Ce(PO_4)_3$ at different temperatures in cell 1.

	$E_{measurement}$ (mV)	$E_{theoretical}$ (mV)	transference number
500°C	-49.10	-62.31	0.79
550°C	-52.08	-66.34	0.79
600°C	-54.30	-70.36	0.77

CHAPTER 7
HYDROGEN PERMEATION MEASUREMENT

7.1 Introduction

Hydrogen permeation can be defined as a process by which pure hydrogen is selectively passed through a separation membrane from a gas mixture. The driving force usually is a pressure or potential gradient. The hydrogen permeation process is a kinetic process. The characteristic length $L_C = D^* / k_s$, where k_s is the surface exchange coefficient and D* is the self diffusion coefficient, determines the transition from bulk diffusion limited to surface exchange rate limited transport [84]. When the thickness L is larger than L_c, the hydrogen flux is governed by the bulk diffusion. A 2 μm film still was considered as bulk diffusion controlled in Yb doped strontium cerate [85]. The thickness of all the membranes in our test was larger than 1 mm, so they should be bulk diffusion controlled.

The ionic transference number of $Ba_3Ce(PO_4)_3$ in hydrogen concentration cells indicates that it is a mixed conductor with dominant proton conduction. Therefore, its hydrogen permeation flux could be measured directly on single phase $Ba_3Ce(PO_4)_3$.

Generally, the hydrogen permeation flux J_{OH_O} across an oxide membrane can be calculated using the Wagner equation, which assumes the bulk diffusion to be the rate-limiting step [35].

$$J_{OH_O} = -\frac{1}{L}\left[\frac{RT}{4F^2}\int_{P_{O_2}}^{P'_{O_2}} \sigma_{total} t_{OH_O} t_{V_O} d\ln P_{O_2} + \frac{RT}{2F^2}\int_{P_{H_2}}^{P'_{H_2}} \sigma_{total} t_{OH_O}(t_{V_O} + t_{e'}) d\ln P_{H_2}\right] \quad (1\text{-}17)$$

According to literature [13], the hydrogen permeation rate of 0.11 cm thick $SrCe_{0.95}Y_{0.05}O_{3-\delta}$ membrane is only 0.006 cm^3 (STP) cm^{-2} min^{-1} at 600°C while its conductivity is around 10^{-3}~10^{-2} S/cm and proton transference number is around 0.86 in a dry hydrogen concentration cell (4% H_2/ 0.488% H_2).

The total conductivities of $Ba_3Ce(PO_4)_3$ are 4.04×10^{-5} and 1.46×10^{-4} S/cm at 600°C in dry and wet 4vol% hydrogen, respectively. The proton transference number was around 0.8 and the electronic transference number was around 0.2 at 600ºC in dry hydrogen concentration cells. Therefore, a low hydrogen flux of $Ba_3Ce(PO_4)_3$ is expected due to its low total conductivity. Hydrogen permeation is only studied in dry hydrogen atmosphere in this work.

As mentioned before, two-phase composites can provide continuous channels for both proton and electronic conductivity and enhance hydrogen transport. Hydrogen permeation was tried on the composites $Ba_3Ce(PO_4)_3$-CeO_2 and $Ba_3Ce(PO_4)_3$-Pd, in which CeO_2 or Pd was used to increase the electronic conductivity in the composites.

7.2 Experiment

For $Ba_3Ce(PO_4)_3$ membrane samples, the sintering procedures were the same as that for conductivity measurement. For composite $Ba_3Ce(PO_4)_3$-CeO_2 or $Ba_3Ce(PO_4)_3$-Pd, powders were mixed and ball milled for 24 h and then sintered at 1450 °C for 10 h. Their relative densities are higher than 90%.

The hydrogen permeability measurement system is shown in Figure 7-1. The sealant is glass powder V-10031. The feed gas is a mixture of dry helium and dry hydrogen with a flow rate of 50 sccm. The sweep gas is helium and flow rate is 20 sccm.

A small amount of argon gas was flowed on the feed side to check for a gas leakage in the system. The gas partial pressure on the sweep side was measured by a mass spectrometer (Q100MS Dycor Quadlink).

7.3 Results and Discussion

7.3.1 Hydrogen Permeability of $Ba_3Ce(PO_4)_3$

Figure 7-2 shows the partial pressure of various gases at the sweep side while testing $Ba_3Ce(PO_4)_3$ at 600 °C. In the first 30mins, only helium and a small amount of argon were fed. Therefore, the partial pressures of other gases such as hydrogen, nitrogen, and oxygen could be considered as baseline. The sealing of the system appeared to be sufficient because the argon partial pressure was lower than 8×10^{-11} kPa and the partial pressure of nitrogen and oxygen was lower than 2.67×10^{-10} kPa. After collecting baseline for 30 mins, helium was shut down and pure hydrogen was fed. The hydrogen partial pressure at the sweep side did not increase. This indicates that $Ba_3Ce(PO_4)_3$ does not have good hydrogen permeability under these conditions.

7.3.2 Hydrogen Permeability of Composite $Ba_3Ce(PO_4)_3$ with CeO_2

$Ba_3Ce(PO_4)_3$ is a mixed conductor with proton conduction dominance. However, based on results above, its electronic conductivity and proton conductivity do not appear high enough for it to have good hydrogen permeability. As mentioned in chapter 3, CeO_2 and $Ba_3Ce(PO_4)_3$ were observed in composite BCG5Pd. That BCG5Pd sample demonstrated a higher hydrogen flux than solid state synthesized composite BCG35Pd when the operating temperature was lower than 550 °C. There is a possibility that CeO_2 may have some contribution to that hydrogen flux. Therefore, $Ba_3Ce(PO_4)_3$ was mixed

with CeO_2 to check whether or not electron hopping between Ce^{3+} in $Ba_3Ce(PO_4)_3$ and Ce^{4+} in CeO_2 facilitated the hydrogen permeation.

Figure 7-3 shows the XRD result of composite CeO_2-$Ba_3Ce(PO_4)_3$ before and after sintering. CeO_2 and $Ba_3Ce(PO_4)_3$ were indexed. No tertiary phase was detected by XRD. Figure 7-4 shows the cross section of composite. There is no interconnected pore structure. Figure 7-5 shows the partial pressure of gases at the sweep side while testing the composite CeO_2-$Ba_3Ce(PO_4)_3$ at 600 °C. Helium and a small amount of argon were fed in the first 30mins. No leakage was detected. Then helium was shut off and hydrogen was feed. The hydrogen partial pressure on the sweep side is 1.80×10^{-10} kPa, slightly larger compared with baseline 1.52×10^{-10} kPa in figure 7-2. The actual hydrogen partial pressure caused by permeation is 2.8×10^{-11} kPa. The hydrogen permeability of composite is almost zero when considering the mass spectrometer resolution. This indicated that the electronic conductivity provided by the hopping between Ce^{3+} and Ce^{4+} was not enough for hydrogen permeation.

7.3.3 Hydrogen Permeability of Composite 35vol%Pd-65vol% $Ba_3Ce(PO_4)_3$

$Ba_3Ce(PO_4)_3$ was also mixed with 35vol%Pd and sintered to form a composite. Figure 7-6 shows the XRD results of composite 35vol%Pd-65vol% $Ba_3Ce(PO_4)_3$ sintered in air and treated in argon atmosphere. No tertiary phase was detected by XRD. Figure 7-7 shows the surface image of composite Pd-$Ba_3Ce(PO_4)_3$. Pd isolated itself from $Ba_3Ce(PO_4)_3$ grain due to the difference bond type of metal and ceramic. Figure 7-8 shows the EDS results on a Pd grain and a $Ba_3Ce(PO_4)_3$ grain. They all contained Pd,

but the concentration of Pd in $Ba_3Ce(PO_4)_3$ grain is low. Figure 7-9 shows there are no interconnected pores in the cross-section of composite.

Figure 7-10 shows the partial pressure of gases on the sweep side while testing composite 35vol%Pd-65vol%$Ba_3Ce(PO_4)_3$. The argon concentration increased very quickly once it was fed, indicating the sealing was poor. The inherent properties of the sealant or microcracks in the sample may be the source of the leak. The sample was broken after the furnace was cooled down to room temperature, so the origin of the leakage is not clear. Composite 5vol%Pd-95vol%$Ba_3Ce(PO_4)_3$ was also tried and had a similar leakage problem. Therefore, while these composites may have a high hydrogen permeation, inability to obtain sealed crack free sample prevented further measurements.

7.4 Conclusion

Glass powder V-10031 was found to be a good sealant for $Ba_3Ce(PO_4)_3$ or composite CeO_2-$Ba_3Ce(PO_4)_3$. However, $Ba_3Ce(PO_4)_3$ did not exhibit any significant hydrogen permeability with a He sweep gas. The electronic conductivity provided by the electron hopping between Ce^{3+} and Ce^{4+} was not enough for hydrogen permeation of composite CeO_2-$Ba_3Ce(PO_4)_3$ under these same conditions.

However, the transference number results in chapter 6 indicate that $Ba_3Ce(PO_4)_3$ has an electronic transference number of 0.2 in the dry hydrogen concentration cells and therefore should exhibit hydrogen permeation. One major difference between the permeation and transference measurements was the composition of the sweep gas. When the hydrogen permeation is measured with a He sweep gas, the corresponding oxygen partial pressure region on sweep side belongs to the intermediate region; therefore, the

electronic conductivity is lower. If the hydrogen permeation is measured in the low oxygen partial pressure region with a hydrogen sweep gas, the electronic conductivity may be sufficient for hydrogen permeation. Further permeation work of $Ba_3Ce(PO_4)_3$ with a hydrogen sweep gas is necessary.

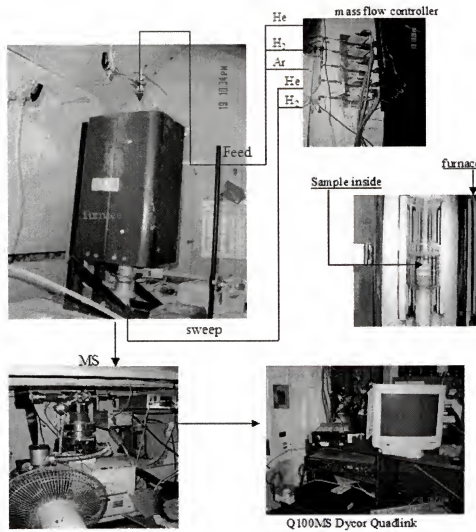

Figure 7-1. Hydrogen permeability measurement system.

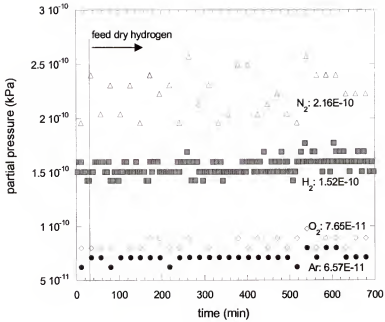

Figure 7-2. Gas partial pressure on sweep side while testing $Ba_3Ce(PO_4)_3$.

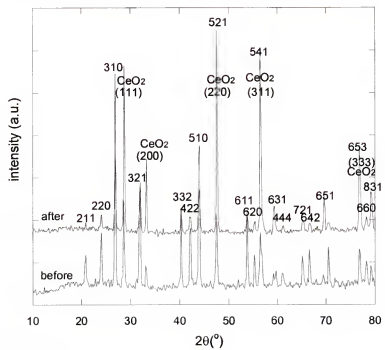

Figure 7-3. XRD patterns of composite CeO_2 - $Ba_3Ce(PO_4)_3$ before and after sintering.

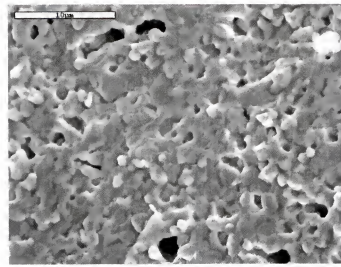

Figure 7-4. Cross-section image of composite CeO_2 - $Ba_3Ce(PO_4)_3$.

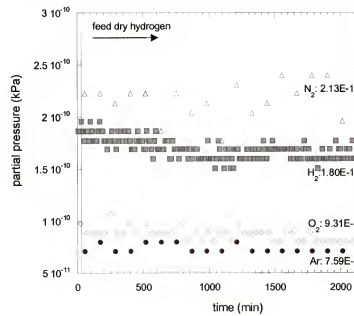

Figure 7-5. Gas partial pressure on sweeping side while testing composite CeO_2 - $Ba_3Ce(PO_4)_3$.

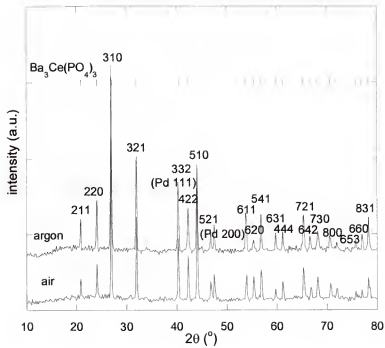

Figure 7-6. XRD pattern of composite 35 vol% Pd–65 vol% $Ba_3Ce(PO_4)_3$ after separate treatment in air and argon.

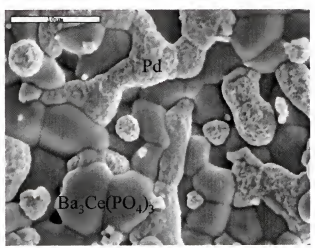

Figure 7-7. Surface image of composite 65 vol% $Ba_3Ce(PO_4)_3$ -35 vol% Pd.

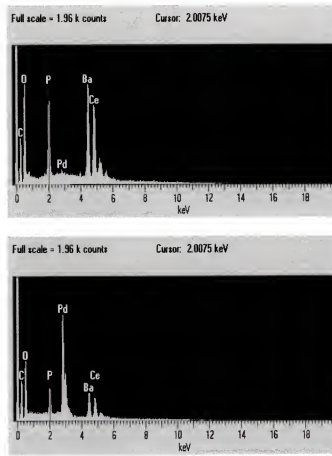

Figure 7-8. EDS results of $Ba_3Ce(PO_4)_3$ grain and Pd grain in the composite 65 vol% $Ba_3Ce(PO_4)_3$-35 vol% Pd.

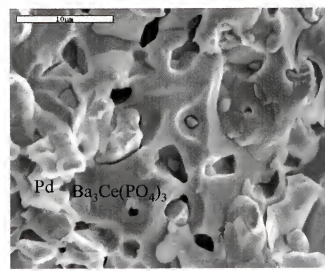

Figure 7-9. Cross-section image of composite 35 vol% Pd-65 vol% $Ba_3Ce(PO_4)_3$.

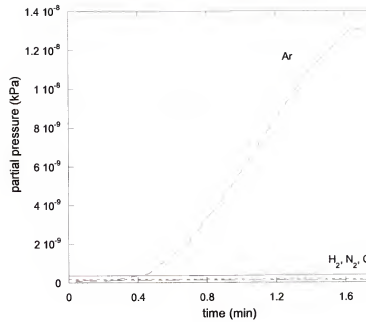

Figure 7-10. Gas partial pressure on sweeping side with composite 35 vol% Pd-65 vol% $Ba_3Ce(PO_4)_3$.

CHAPTER 8
CONCLUSION

In previous work in our lab, the hydrogen flux of composite BCG5Pd was higher than that of BCG35Pd when the temperature was lower than 550ºC. Additionally, this hydrogen flux did not achieve an equilibrium value for 20 hours at 650ºC until feed gas was shut off [36]. The second phase, Pd, did not exhibit such a trend under isothermal conditions, indicating the existence of a tertiary phase. Analysis results showed that the phosphorous impurity was introduced. In electroless deposition, exposure to acidic bath decomposed part of BCGO to form CeO_2 and the absorbed phosphorus impurity covered the BCGO particles. They reacted at higher temperature to form a BaO-rich compound $Ba_3Ce(PO_4)_3$ and leave a certain CeO_2 excess. $Ba_3Ce(PO_4)_3$ is most likely the desired tertiary phase in the composite BCG5Pd.

Single-phase $Ba_3Ce(PO_4)_3$ was synthesized successfully by a co-precipitation method at a lower temperature than that required for solid-state reaction. It was stable in dry air, helium, argon, and hydrogen. The conductivity of $Ba_3Ce(PO_4)_3$ is 8.91×10^{-6} S/cm at 600 °C in wet oxygen, which is higher than undoped $LaPO_4$ and YPO_4 but lower than 5 mol% Sr doped $LaPO_4$. The conductivities of $Ba_3Ce(PO_4)_3$ are 4.04×10^{-5} and 1.46×10^{-4} S/cm at 600 °C in dry and wet 4vol% hydrogen, respectively. The proton transference number was around 0.8 and the electronic transference number was around 0.2 at 600ºC in hydrogen concentration cells. Therefore, $Ba_3Ce(PO_4)_3$ was a mixed conductor with dominant proton conduction. However, neither its proton nor electron

conductivity was high enough for hydrogen separation with a He sweep gas. The electronic conductivity provided by the electron hopping between Ce^{3+} and Ce^{4+} was also too low to allow hydrogen separation in the composite CeO_2- $Ba_3Ce(PO_4)_3$ under these conditions. It is still possible to obtain a hydrogen flux with hydrogen on both sides.

The results of Raman spectroscopy and magic-angle spinning nuclear magnetic resonance showed the local structures of $Ba_3Ce(PO_4)_3$ at different atmospheres. Protons. Free hydrogen can be oxidized forming protons and incorporated into the lattice. In the presence of water vapor, bound hydrogen is produced and oxidized forming protons. The formed protons attach onto the O atoms of PO_4 group and are incorporated into the lattice.

The defect structure of $Ba_3Ce(PO_4)_3$ was proposed in the low, low-intermediate, intermediate and high oxygen partial pressure regions. The conductivity of $Ba_3Ce(PO_4)_3$ as a function of oxygen partial pressure and water partial pressure supported the proposed defect structure.

LIST OF REFERENCES

1. R. W. Moss, A. P. Roskilly and S. K. Nanda, *Applied Energy*, **80**, 169 (2005)

2. S. Tosti, *International Journal of Hydrogen Energy*, **28**, 1445 (2003)

3. R. Checchetto, N. Bazzanella, B. Patton and A. Miotello, *Surface and Coatings Technology*, **177-178**, 73 (2004)

4. D. Wang, T. B. Flanagan and K. L. Shanahan, *Journal of Alloys and Compounds*, **372**, 158 (2004)

5. A. K. Garg, L. C. De Jonghe, *Journal of Material Science*, **28**, 33427 (1993)

6. R. S. A. de Lange, J. H. A. Hekkink, K. Keizer and A. J. Burggraaf, *Microporous Materials*, **4**, 169 (1995)

7. D. Lee and S. T. Oyama, *Journal of Membrane Science*, **210**, 291 (2002)

8. M. Asaeda and S. Yamasaki, *Separation and Purification Technology*, **25**, 151 (2001)

9. C. Y. Tsai, S. Y. Tam, Y. Liu and C. J. Brinker, *Journal of Membrane Science*, **169**, 255 (2000)

10. H. Iwahara, T. Esaka, H. Uchida and N. Maeda, *Solid State Ionics*, ¾, 359 (1981)

11. K. D. Kreuer, *Solid State Ionics*, **97**, 1 (1997)

12. M. E. Kompan, Y. M. Bailov, B. A. –T. Melekh and B. Z. Volchek, *Solid State Ionics*, **162-163**, 1 (2003)

13. J. Guan, S. E. Dorris, U. Balachandra and M. Liu, *Solid State Ionics*, **110**, 303 (1997)

14. H. Iwahara, T. Yajima, T. Hibino and H. Ushida, *J. Electrochem. Soc.*, **140**, 1687 (1993)

15. N. Taniguchi, E. Yasumoto and T. Gamo, *J. Electrochem. Soc.*, **143**, 1886 (1996)

16. N. Bonanos, B. Ellis and M. N. Mahmood, *Solid State Ionics*, **44**, 305 (1991)

17. R. A. Davies, M. S. Islam and J. D. Gale, Solid State Ionics, **126**, 323 (1999)

18. T. Yajima, H. Yogo and H. Iwahara, *Solid State Ionics*, **51**, 101 (1992)

19. S. Shin, H. H. Huang and M. Ishigame, *Solid State Ionics*, **40/41**, 910 (1990)

20. S. M. Haile, D. L. West and J. Campbell, *J. Mater. Res.*, **V13,** 1576 (1998)

21. R. J. Phillips, N. Bonanos, F. W. Poulsen and E. O. Ahlgren, *Solid State Ionics*, **125**, 389 (1999)

22. H. Iwahara, *Solid State Ionics*, **77**, 289 (1995)

23. R. C. T. Slade and N. Singh, *Solid State Ionics*, **46**, 111 (1991)

24. J. M. Rhode and E. D. Wachsman, *Electrochem. Soc. Pro.*, **99-13**, 151 (2001)

25. G. Alberti and M. Casciola, *Solid State Ionics*, **145**, 3 (2001)

26. T. Norby, *Solid State Ionics*, **125**, 1 (1999)

27. T. Norby, *Solid State Ionics*, **77**, 240 (1995)

28. W. K. Lee and A. S. Nowick, *Solid State Ionics*, **18/19**, 989 (1986)

29. K. C. Liang, Y. Du, A. S. Nowick, *Solid State Ionics*, **69**, 910 (1990)

30. H. Matsumoto, S. Hamajima and H. Iwahara, *Solid State Ionics*, **145**, 25 (2001)

31. H. Iwahara, T. Esaka, H. Uchida and T. Yamauchi, K. Ogaki, *Solid State Ionics*, **18-19**, 1003 (1986)

32. J. Guan, S. E. Dorris, U. Balachandran and M. liu, *J. Electrochem. Soc.*, **145**, 1780 (1998)

33. F.A. Kröger and H.J. Vink, *Solid State Phys.*, **3**, 307 (1956)

34. K. D. Kreuer, *Chem. Mater.*, **8**, 610 (1996)

35. S. -J. Song, E. D. Wachsman, S. E. Dorris, U. Balachandran, *Solid State Ionics*, **149**, 1 (2002)

36. B. Krishnamurthy, M. S. Thesis, *Synthesis and Characterization of Two-Phase Mixed Ionic Electronic Conducting Membranes for Hydrogen Separation*, University of Florida, 2000

37. C. S. Chen, B. A. Boukamp, H. J. M. Bouwmeester, C .Z. Cao, H. Kruidhof, A. J. A. Winnubst and A. J. Burggraaf, *Solid state ionics*, **76**, 23 (1995)

38. H. Iwahara, *Bull. Ceram. Soc. Jpn.*, **27**, 112 (1992)

39. D. C. Harris and M. D. Bertolucci, *Symmetry and Spectroscopy*, p152, Dover Publication, Inc., N.Y., 1989

40. R. B. King, *Encyclopedia of Inorganic Chemistry*, V6, p3096, John Wiley and Sons, New York (1994)

41. G. Socrates, *Infrared and Raman Characteristic Group Frequencies: Tables and Charts*, p290, Wiley, New York, 2001

42. K. Amezawa, H. Maekawa, Y. Tomii and N. Yamamoto, *Solid State Ionics*, **145**, 233 (2001)

43. K. S. Knight, *Mineralogical Magazine*, **64(2)**, 291 (2000)

44. A. Meldrum, L. A. Boatner and R. C. Ewing, *Physical Review B*, **56 (21)**, 13805 (1997)

45. S. Gallini, M. Hansel, T. Norby, M. T. Colomer and J. R. Jurado, *Solid State Ionics*, **162-163**, 167 (2003)

46. K. Amezawa, S. Kjelstrup, T. Norby and Y. Ito, *J. Electrochemical Society*, **V145 No.10**, 3313 (1998)

47. K. Amezawa, Y. Tomii and N. Yamanoto, *Solid State Ionics*, **176**, 135 (2005)

48. K. Amezawa, Y. Tomii and N. Yamamoto, *Solid State Ionics*, **176**. 143 (2004)

49. N. Kitamura, K. Amezawa, Y. Tomii, N. Yamamoto and T. Hanada, *Solid State Ionics*, **175**, 563 (2004)

50. K. Amezawa, Y. Tomii and N. Yamamoto, *Solid State Ionics*, **162-163**. 175 (2003)

51. N. Kitamura, K. Amezawa, Y. Tomiim and N. Yamamoto, *Solid State Ionics*, **162-163**, 161 (2003)

52. A. I. Baranov, V. M. Duda, D. J. Jones, J. Roziere, V. V. Sinitsyn and R. C. T. Slade, *Solid State Ionics*, **145**, 241 (2001)

53. S. M. Haile, P. M. Calkins and D. Boysen, *Solid State Ionics*, **97**, 145 (1997)

54. S. M. Haile, D. A. Boysen, C. R. I. Chisholm and R. B. Merle, *Nature*, **410**, 910 (2001)

55. S. M. Haile and K. -D. Kreuer, *J. Mater. Acta Cryst.*, **B 51**, 680 (1995)

56. T. Ude, D. A. Boysen and S. M. Haile, *Solid State Ionics*, **176**, 127 (2005)

57. S. M. Haile and P. M. Calkins, *J. Solid State Chem.*, **140**, 251 (1998)

58. C. R. I. Chisholm and S. M. Haile, *Solid State Ionics*, **136-137**, 229 (2000)

59. J. Otomo, N. Minagawa, C. Wen, K. Eguchi and H. Takahashi, *Solid State Ionics*, **156**, 357 (2003)

60. A. T. Howe and M. G. Shilton, *J. Solid State Chem.*, **28**, 345 (1979)

61. M. Pham-Thi and Ph. Colomban, *Solid State Ionics*, **17**, 295 (1985)

62. M. Casciola and U. Costantino, *Solid State Ionics*, **20**, 69 (1986)

63. G. Alberti, M. Casciola, U. Costantino, A. Peraio and T. Rega, *J. Mater. Chem.*, **5**, 1809 (1995)

64. G. Alberti, M. Casciola, L. Massinelli and R. Palombari, *Ionics*, **2**, 179 (1996)

65. G. Alberti and M. Casciola, *Solid State Ionics*, **97**, 177 (1997)

66. J. S. Wainright, J. T. Wang, D. Weng, R. F. Savinell and M. Litt, *J. Electrochem. Soc.*, **142**, L121 (1995)

67. M. Mizuno and S. Hayashi, *Solid State Ionics*, **167**, 317 (2004)

68. S. Hayashi and M. Mizuno, *Solid State Ionics*, **171**, 289 (2004)

69. X. Ke and I. Tanaka, *Solid State Ionics*, **172**, 145 (2004)

70. R. S. Souleimanova, A. S. Mukasyan and A. Varma, *AIChE Journal*, **48**, 262 (2002)

71. D. Shima and S. M. Haile, *Solid State Ionics*, **97**, 443 (1997)

72. A. C. Caballero, J. F. Fernandez, C. Moure and P. Duran, *Materials Letters*, **35**, 72 (1998)

73. W. Szuszkiewica and T. Znamierowska, *J. Solid State Chem.*, **88**, 406 (1990)

74. N. A. Lange, *Lange's Handbook of Chemistry*, section 8.9, McGraw-Hill, New York, 2005

75. Pierre Stadelmann, *Electron Microscopy Image Simulation*, 1995, http://www.cimesgl.epfl.ch/ciol/ems.html (March 2003)

76. J. Barbier, *J. Solid State Chem.*, **101**, 249 (1992)

77. T. BenChaabane, L. Smiri and A. Bulou, *Solid State Sciences*, **6**, 197 (2004)

78. M. Harcharras, F. Capitelli, A. Ennaciri, K. Brouzi, A. G. G. Moliterni, G. Mattei and V. Bertolasi, *Journal of Solid State Chemistry*, **176**, 27 (2003)

79. T. Osaka, C. Numako and K. Koto, *Materials Research Bulletin*, **34**, 11 (1999)

80. S. Kim, K. H. Lee and H. L. Lee, *Solid State Ionics*, **144**, 109 (2001)

81. X. Qi, F .T. Akin and Y. S. Lin, *Journal of Membrane Science*, **193**, 185 (2001)

82. K. L. Ley, M. Krumpelt, R. Kumar, J. H. Meiser and I. Bloom, *Journal of Materials Research*, **11**, 1489 (1996)

83. R. Morena, *Journal of Non-Crystalline Solids*, **263&264**, 382 (2000)

84. P. J. Gellings and H. J. M. Bouwmeester, *The CRC Handbook of Solid State Electrochemistry*, p.504, CRC press,Inc., Boca Raton, USA., 200

85. S. Hamakawa, L. Lnwu and E. Iglisia, Solid State Ionics, **148**, 71 (2002)

BIOGRAPHICAL SKETCH

Guojing Zhang was born in 1974. She got her bachelor's degree in 1995 from the Department of Inorganic Material, East China University of Science and Technology (ECUST), Shanghai, P. R. China. She worked in Jiangsu Province Building Material School, currently Changzhou Institute of Engineering Technology, after graduation. Two years later, she went back to graduate school and earned her master's degree in 2000 from the Department of Chemistry in ECUST.

In the fall of 2000, she entered the Department of Materials Science and Engineering in University of Florida. She pursued her Ph.D. in the field of solid state ionics under the guidance of Prof. E. D. Wachsman.

I certify that I have read this study and that in my opinion it conforms to acceptable standards of scholarly presentation and is fully adequate, in scope and quality, as a dissertation for the degree of Doctor of Philosophy.

Eric D. Wachsman, Chairman
Professor of Materials Science and Engineering

I certify that I have read this study and that in my opinion it conforms to acceptable standards of scholarly presentation and is fully adequate, in scope and quality, as a dissertation for the degree of Doctor of Philosophy.

Timothy J. Anderson
Professor of Chemical Engineering

I certify that I have read this study and that in my opinion it conforms to acceptable standards of scholarly presentation and is fully adequate, in scope and quality, as a dissertation for the degree of Doctor of Philosophy.

Juan C. Nino
Assistant Professor of Materials Science and Engineering

I certify that I have read this study and that in my opinion it conforms to acceptable standards of scholarly presentation and is fully adequate, in scope and quality, as a dissertation for the degree of Doctor of Philosophy.

E. Dow Whitney
Professor of Materials Science and Engineering

I certify that I have read this study and that in my opinion it conforms to acceptable standards of scholarly presentation and is fully adequate, in scope and quality, as dissertation for the degree of Doctor of Philosophy.

Kevin Jones
Professor of Materials Science and Engineering

I certify that I have read this study and that in my opinion it conforms to acceptable standards of scholarly presentation and is fully adequate, in scope and quality, as a dissertation for the degree of Doctor of Philosophy.

Wolfgang Sigmund
Associate Professor of Materials Science and Engineering

This dissertation was submitted to the Graduate Faculty of the College of Engineering and to the Graduate School and was accepted as partial fulfillment of the requirements for the degree of Doctor of Philosophy.

December 2005

Pramod P. Khargonekar
Dean, College of Engineering

Kenneth J. Gerhardt
Interim Dean, Graduate School